scientific reports

OPEN

Cortical glia in SOD1(G93A) mice are subtly affected by ALS-like pathology

Tereza Filipi[1,2,7], Zuzana Matusova[3,4,7], Pavel Abaffy[3], Ondrej Vanatko[1,2], Jana Tureckova[1], Sarka Benesova[3,5], Monika Kubiskova[1], Denisa Kirdajova[1], Jakub Zahumensky[6], Lukas Valihrach[3]✉ & Miroslava Anderova[1]✉

The role of glia in amyotrophic lateral sclerosis (ALS) is undeniable. Their disease-related activity has been extensively studied in the spinal cord, but only partly in the brain. We present herein a comprehensive study of glia in the cortex of SOD1(G93A) mice—a widely used model of ALS. Using single-cell RNA sequencing (scRNA-seq) and immunohistochemistry, we inspected astrocytes, microglia, and oligodendrocytes, in four stages of the disease, respecting the factor of sex. We report minimal changes of glia throughout the disease progression and regardless of sex. Pseudobulk and single-cell analyses revealed subtle disease-related transcriptional alterations at the end-stage in microglia and oligodendrocytes, which were supported by immunohistochemistry. Therefore, our data support the hypothesis that the SOD1(G93A) mouse cortex does not recapitulate the disease in patients, and we recommend the use of a different model for future studies of the cortical ALS pathology.

The characteristic degeneration of motor neurons (MNs) in ALS initially causes progressive muscle atrophy leading to difficulties with movement, speaking and swallowing, and respiratory failure in the final stage. Generally, ALS is considered as a multifactorial disease with poorly understood pathological mechanisms, and with a median survival of three to five years. There is currently no cure or prevention available, only symptomatic treatment.

Although MNs are recognized as the primary cell type affected by the pathology, multiple studies have confirmed that also non-neuronal cells including glia undergo changes and participate in ALS progression[1,2]. Glial cells respond to neurodegeneration or injury by various mechanisms. Microglia and astrocytes acquire a so-called reactive state marked by changes of gene expression and morphology. By the activation of inflammatory and anti-inflammatory pathways, they protect the tissue from further damage. However, in the chronic stage of diseases they have a harmful effect and contribute to the progression of neurodegeneration. Traditionally, reactive astrocytes and microglia were divided into A1 and A2 or M1 and M2 subtypes, respectively. However, this terminology is currently considered outdated, as many various subpopulations of glia with specific gene signatures have recently been described in different disease models[3–5]. Disease-associated astrocytes (DAA), disease-associated microglia (DAM), activated response microglia (ARM), and interferon response microglia (IRM), are just a few examples of these. Oligodendrocytes, on the other hand, are more susceptible to pathological changes. In reaction to disease, they tend to degenerate, rather than transform into a reactive state. However, their passive role in the progression of disease has recently been questioned by studies describing their contribution to immunoprotection, interferon signaling and antigen processing and presentation[6,7].

The role of astrocytes, microglia and oligodendrocytes, and their respective pathology-related changes, have been reported in ALS patients multiple times[8–10]. The majority of available data come from the spinal cord, but a few studies also reported glial pathology in the cortex[11]. The known pathological changes were mostly identified

[1]Department of Cellular Neurophysiology, Institute of Experimental Medicine, Czech Academy of Sciences, Videnska 1083, 14220 Prague, Czech Republic. [2]Second Faculty of Medicine, Charles University, V Uvalu 84, 15006 Prague, Czech Republic. [3]Laboratory of Gene Expression, Institute of Biotechnology CAS, BIOCEV, Prumyslova 595, 25250 Vestec, Czech Republic. [4]Faculty of Science, Charles University, Albertov 6, 12800 Prague, Czech Republic. [5]Department of Informatics and Chemistry, Faculty of Chemical Technology, University of Chemistry and Technology, Technicka 5, 16628 Prague, Czech Republic. [6]Department of Functional Organization of Biomembranes, Institute of Experimental Medicine, Czech Academy of Sciences, Videnska 1083, 14220 Prague, Czech Republic. [7]These authors contributed equally: Tereza Filipi and Zuzana Benesova. ✉email: lukas.valihrach@ibt.cas.cz; Miroslava.Anderova@iem.cas.cz

in *post mortem* tissue, which does not allow for study of the disease mechanisms, increasing the need for a reliable animal model. Currently, the SOD1(G93A) mouse represents the most widely used model resembling familial ALS[12]. Phenotypically the model matches the disease course, and studies in the spinal cord and brainstem reported ALS-related cellular changes previously found in patients[2,8,13–16]. The cortex, however, seems to be a subject of controversy. The number of studies is limited, and the results suggest contradictory outcomes. While some show that cortical glial cells and MNs are affected by the ALS-like phenotype[17–20], others report no effect in the cortical area in the SOD1(G93A) model[21].

In this study, we aimed to provide a comprehensive insight into the SOD1 glial pathology in the cortex of the SOD1(G93A) mouse. Combining robust and high-throughput methods such as scRNA-seq and immunohistochemistry, we analyzed astrocytes, microglia, and oligodendrocytes, during the complete course of the disease, which was characterized by behavioral tests. The scRNA-seq was used to monitor transcriptional changes in individual glial cells in time, and to investigate the composition of distinct glial populations with a particular focus on disease-associated subpopulations. To complete the characterization of the cortical pathology, we evaluated the morphological and quantitative changes of glial cells using immunohistochemistry, measuring canonical protein markers.

Methods

Animals. For all experiments, we used transgenic mice expressing high levels of human SOD1(G93A) (JAX Strain: 004435 C57BL/6 J-Tg (SOD1*G93A)1Gur/J) and their non-carrier littermates[12]. This strain contains ~ 25 copies of the transgene, and its 50% survival ranges 157 ± 9.3 days (https://www.jax.org/strain/004435). All experimental protocols were approved by the Czech Republic Animal Care Commitee (approval number 40/2019). All methods using animals were carried out in accordance with the European Communities Council Directive (86/609/EEC). All animals used for experiments were sacrificed using pentobarbital followed by decapitation. Due to an advanced stage of the disease, mutant mice were euthanized using carbon dioxide shortly after reaching five months of age. All efforts were made to minimize both the suffering and the number of animals used. The study is reported in accordance with the ARRIVE guidelines.

Behavioral testing. We conducted the wire grid hang test and the rota-rod test (Mouse RotaRod NG 47650, Ugo Basile, Italy) to assess muscle strength, function, and coordination throughout the disease. Weight was also measured as an additional parameter of the symptom progression. Testing consisted of a single three-attempt session every week, beginning at P30, and lasted for 14 weeks. Before the experiment, all animals performed training. Data are presented as mean or mean ± standard error of the mean (SEM) for n animals. Repeated measures two-way ANOVA with Holm-Sidak's multiple comparison correction was used to analyze the differences between groups.

Wire grid hang test. The mouse was placed on a custom-made wire lid, approximately 60 cm above a wood chip covered bottom, and turned upside down. The latency to fall was measured. At the beginning of a testing period, we trained each mouse three consecutive times for at least 180 s. In the experimental session, the mouse had three attempts to hold on to the lid. We noted the best score out of the three with a maximum of 180 s.

Rota-rod test. The mouse was placed on a stationary rod facing against the direction of rotation. The rod started rotating at a constant speed of 15 rpm, and the latency to fall was measured. Each mouse was trained three consecutive times of at least 180 s at 5, 10 and 15 rpm speed. In the experimental session, the mouse had three attempts to remain on the rod. We noted the best score out of the three with a maximum of 180 s.

Immunohistochemistry. For immunohistochemical analyses, the animals were deeply anesthetized with PTB (100 mg/kg, i.p.), perfused transcardially with 20 ml of saline solution followed by 20 ml of cooled 4% paraformaldehyde (PFA) in 0.1 M phosphate buffer and decapitated. The brains and spinal cords were dissected out, postfixed overnight with PFA and treated with a sucrose gradient (ranging from 10 to 30%) for cryoprotection. Coronal 30-µm-thick slices were prepared using a cryostat (Leica CM1850, Leica Microsystems, Wetzlar, Germany).

For immunohistochemical staining, the slices were washed in a phosphate buffer saline followed by blocking of the nonspecific binding sites with 5% Chemiblocker (Millipore, Billerica, MA), and 0.2% Triton in phosphate buffer saline. The blocking solution was also used as the diluent for the antisera. The slices were incubated with the primary antibodies overnight, and the secondary antibodies were applied for 2 h at 4–8 °C.

The following primary antibodies were used: rabbit anti-aldehyde dehydrogenase 1 family, member L1 (ALDH1L1 1:500; Abcam, Cambridge, UK), rat anti-myelin basic protein (MBP, 1:500, Biorad, Hercules, CA, US), rabbit anti-choline acetyltransferase (ChAT, 1:200, Merck, Darmstadt, Germany), rabbit anti-ionized calcium-binding adapter molecule 1 (Iba-1, 1:500, Abcam, Cambridge, UK), rabbit cleaved caspase-3 (CC3, 1:50, CellSignaling, Massachusetts, USA) and adenomatous polyposis coli (APC, 1:200, Merck, Darmstadt, Germany). The secondary antibodies were goat anti-rabbit IgG or goat anti-mouse IgG conjugated with Alexa Fluor 488, and chicken anti-rat IgG conjugated with Alexa Fluor 488 (1:500, Invitrogen, Waltham, MA, US). Cell nuclei were visualized by DAPI staining (Merck, Darmstadt, Germany). A Zeiss LSM 880 Airyscan confocal microscope equipped with Ar/HeNe lasers and × 40 water or × 63 oil objectives were used for the immunohistochemical analysis.

Image analysis and quantification. All analysis were done using FIJI image processing software (ImageJ 2.9.0/1.53t)[22]. Confocal images (212 × 212 × 30 µm) were taken from brain coronal slices (1 mm and 2 mm from bregma), covering area of primary and secondary motor and primary somatosensory cortex (five to six zones per hemisphere).

To quantify the ALDH1L1 fluorescence intensity, we used six animals for each group and two slices from each animal. The thresholding method (Yen method) was used to filter out the background. We calculated the mean integrated density limited to the threshold for each animal.

To quantify changes in morphology of microglia, we conducted Sholl analysis on IBA1 positive cells using Sholl analysis plugin[23]. We used six animals for group and two brain slices from each animal. For each brain slice, a minimum of eight cells was analyzed. For the Sholl analysis, the consecutive z-stack images were converted to maximum intensity projection and the projection was thresholded for creating a binary mask. We counted the number of intersections starting from 5 µm from the center of soma, with radius step size of 5 µm.

To quantify the APC and CC3-positive cells, three animals from each group and one slice (1 mm from bregma) from each animal was used for the analysis. The number of APC or CC3-positive cells was determined from superimposed images and expressed as the percentage of marker expressing cells from the total number of DAPI + cells. The percentage of apoptotic cells was then expressed as a ratio of CC3 + to the previously counted APC + cells.

An Olympus FV10i confocal microscope equipped with × 60 oil objective was used for the analysis of MBP staining. We used six animals for each group and two slices for each animal and scanned 12 zones per each hemisphere. MBP expression density was determined using custom-written FIJI (ImageJ) macro (available at: https://github.com/jakubzahumensky/JT_paper). In brief, to keep the dimensionality of analyzed images equal, the macro extracted a substack of the 20 brightest frames from each z-stack. This was followed by creating a binary mask of the fibers in each frame and measurement of the frame fraction covered by the mask. Within each substack, the mean of this value was calculated, resulting in the volume fraction taken up by the fibers. The statistical analysis of the differences among groups was performed using unpaired t-test. All error bars in plots represent standard error of mean (SEM).

The preparation of single-cell suspension. The mice were deeply anaesthetized with pentobarbital (PTB) (100 mg/kg, i.p.), and perfused transcardially with a cold (4–8 °C) isolation buffer containing (in mM): NaCl 136.0, KCl 5.4, HEPES 10.0, glucose 5.5, osmolality 290 ± 3 mOsmol/kg. We isolated motor and primary somatosensory cortex and followed the Adult Brain dissociation protocol for mice and rats (Milteyni-Biotec, Germany) but omitted the red blood cell removal step. To prevent the activation of immediate early genes (IEGs), we used transcriptional inhibitor actinomycin D (Sigma–Aldrich, St. Louis, MO), 30 µM during enzymatic dissociation and 3 µM in the following steps[24]. After the debris removal, the cells were layered on top of 5 ml of ovomucoid inhibitor solution (Worthington, NJ) and harvested by centrifugation (300 × *g* for 6 min). Potential cell aggregates were removed by 70 µm cell strainers (Becton Dickinson, NJ). We labeled the final suspension with ACSA-2, Cd11b and O4 antibodies conjugated with allophycocyanin and phycoerythrin respectively (4 °C, 10 min; Miltenyi-Biotec, Germany) to allow for the enrichment of astrocytes[25], microglia and oligodendrocytes. The cells were enriched using flow cytometry (FACS; BD Influx), calibrated to sort ACSA-2 + , Cd11b + and O4 + cells. Hoechst 33258 (ThermoFisher Scientific, Waltham, MA) was used to check viability. The cells were collected into 200 µl of Advanced Dulbecco's Modified Eagle Medium, supplemented with 10% fetal bovine serum (ThermoFisher Scientific Waltham, MA). Four animals per condition were pooled for the preparation of cell suspension. After FACS, the cell suspension was spun down, concentrated, and used for library preparation.

scRNA-seq. Chromium Next GEM Single Cell 3' Reagent Kits v3.1 (10 × Genomics, Pleasanton, CA) was used to prepare the sequencing libraries, and the protocol was performed according to the manufacturer's instructions. Briefly, 10 × Chromium platform was used to encapsulate individual cells into droplets along with beads covered in cell-specific 10 × Barcodes, unique molecular identifiers (UMIs) and poly(dT) sequences. After reverse transcription, the cDNA libraries were amplified (13–14 cycles), fragmented and ligated to sequencing adaptors. SPRISelect magnetic beads were used for purification of the cDNA suspension and size selection of the fragments. Concentration and quality of the libraries was measured using Qubit dsDNA HS Assay Kit (Invitrogen) and Fragment Analyzer HS NGS Fragment Kit (#DNF-474, Agilent). The libraries were pooled and sequenced in paired-end mode using Illumina NovaSeq 6000 SP Reagent Kit, Read 1 containing a barcode and a UMI, and Read 2 covering the sequence of interest. Sequencing data comprised of approx. 100–200 million reads per sample (Supp. Tab. 4).

Data analysis. The sequencing data were aligned to the reference mouse genome GRCm38 and annotated (GENCODE version M8 annotation) by STARsolo (STAR version 2.7.3a)[26]. EmptyDrops function (DropletUtils R package)[27] with a threshold of 100 UMIs and FDR < = 0.001 was applied to preserve only cell-containing droplets. Cells were counted based on the barcodes specific for each droplet/cell. The final number of detected cells differed among samples and was in the range approx. from 2500 to 6800 cells (Supp. Tab. 4).

The data were further processed using Seurat R package (version 4.1.1)[28]. First, data from all samples were SCTransformed and integrated (excluding mitochondrial and ribosomal genes, prefixed by mt- or Rps/Rpl, respectively). Uniform Manifold Approximation and Projection (UMAP) was used to visualize 17 principal components (PC), which were subsequently clustered (FindNeighbors and FindClusters functions, UMAP resolution 0.5). Clusters were annotated based on the expression of known marker genes of the expected cell populations, and their correspondence to the markers found by the FindAllMarkers function (at least 80 % cells in the cluster expressing the markers). DoubletFinder[29] R package was used for the identification of droplets potentially containing more than one cell. Doublet formation rate was set to 3.9 % as estimated by 10 × Genomics, and the data were processed according to the authors' recommendations. Clusters expressing ambiguous markers and containing a higher number of doublets were filtered out of the data set.

Sex (male, female) was assigned to individual cells based on the expression of genes encoded by X (*Xist*) and Y chromosome, and those not matching our criteria (male: counts of *Xist* < 1, nFeature_Y > 0; female: counts of *Xist* > 0, nFeature_Y < 2, nCount_Y < 2; nFeature_Y being a number of Y-encoded genes and nCount_Y being a number of transcripts mapping to Y chromosome) were excluded from the dataset (Supp. Fig. 1a). These cells classified as 'Undefined' comprised almost 1/3 of the total number of cells and represented low quality cells (Supp. Fig. 1b).

A specific gene expression profile was also used to determine a phase of the cell cycle of each cell (CellCycleScoring Seurat function) to ensure that the cells in all phases are equally distributed among clusters. Individual cell types were filtered based on the number of genes detected (nFeature_RNA), number of counts (nCount_RNA) and amount of mitochondrial RNA (percent.mt). The cut-offs specific for each cell type of interest were the following: astrocytes—nFeature_RNA > 1000, 2000 < nCount_RNA < 10,000, percent.mt < 8; microglia—nFeature_RNA > 700, 1000 < nCount_RNA < 10,000, percent.mt < 5; oligodendrocytes—nFeature_RNA > 1300, 2500 < nCount_RNA < 50,000, percent.mt < 5 (Supp. Fig. 1d). Tissue dissociation may induce the expression of IEGs, the first rapid cellular response to stimuli[24,30]. A set of the IEGs (e. g. *Fos* and *Jun* transcription factors) was projected onto the UMAP using AddModuleScore function to investigate the level of induction of these genes by sample preparation (Supp. Fig. 1c). The SoupX R package (version 1.5.2)[31] was applied to remove the contaminating RNA background. The unfiltered and annotated data were supplied as the input. The contamination fraction was estimated by the automated method and was in the range from 1 to 2 % for individual samples. The count values were subsequently corrected for the contamination.

To view the overall differences between samples by pseudobulk principal component analysis (PCA), the normalized and scaled data set was used to create a pseudobulk data by summing up the gene counts of cells belonging to the same condition, age, and sex.

Differential expression analysis and Gene Set Enrichment Analysis. Differentially expressed genes (DEGs) in the single-cell data set were identified by t-test in Seurat's FindMarkers function. Normalized and scaled data in the RNA assay were used in this analysis. *P*-adjusted value (p_{adj}) threshold was set to 0.05, and genes with $\log_2$ fold change ($\log_2$FC) > 1 or < − 1 were considered differentially expressed. Males and females were compared at each time point for each cell type and condition. Control (CTRL) and SOD1 pairs were also tested at each time point and for each cell type (end-stage DEGs in Supp. Tab. 1). The Gene Set Enrichment Analysis (GSEA)[32] was performed using clusterProfiler R package (version 4.0.5)[33,34]. Reference gene set size was limited to 10–800 genes and the significance threshold was set to $p_{\mathrm{adj}} = 0.05$. Only results where more than one gene contributed to the enrichment (core enrichment) were considered relevant.

The analysis of cellular subtypes. Individual cell types of interest (astrocytes, microglia, oligodendrocytes) were analyzed separately. Mitochondrial and ribosomal genes were not included in the subsequent analyses. The filtered, normalized, scaled and SCTransformed data were then subjected to PCA. Within the scope of quality control, several genes were excluded, as they introduced additional undesirable variability in the clustering (*Sod1*, *Gm8566*, *Cmss1*, *Cdk8* and lncRNAs *Xist*, *Gm42418*, *Gm424181*, *Malat1*). 16 PC for microglia and astrocytes, and 17 PC for oligodendrocytes were visualized using UMAP, and clustered at a resolution of 0.2 (FindNeighbors and FindClusters functions). A cluster of male control cells at the 3 M time point was excluded from the astrocyte and oligodendrocyte subsets, as it expressed potentially stress related marker genes (e.g., *Cdkn1a, Fkbp5*), which might have been induced during sample preparation (Supp. Fig. 2).

Markers of the subclusters were identified using the default Wilcoxon test in the FindAllMarkers function (at least 10 % cells in a cluster expressing the given marker, $\log_2$FC > 0.25, Supp. Tab. 3). The identity of the subclusters was determined by comparison with available gene signatures of various previously described cellular subtypes using the AddModuleScore function and by manual annotation based on the calculated marker genes. Reference gene expression signatures were taken from Habib et al.[5] (Gfap-Low and Gfap-High astrocytes), Sala Frigerio et al.[4] (ARM, IRM) and Marques et al.[35] (MFOL1/2, MOL2, MOL5/6). The intermediate state of astrocytes was visualized using a gene set containing calculated markers of cluster 2 and markers of transition state published by Habib et al.[5]. The signature of homeostatic microglia resulted from the combination of homeostatic markers mentioned in Keren-Shaul et al.[3], Mathys et al.[36] and Butovsky and Weiner[37]. The top 30 genes were used for the projection in astrocytes, and 20 genes were used in the microglia and oligodendrocytes. Numbers of cells entering differential expression analysis (DEA) and subpopulation analysis are provided in Supp. Tab. 4.

Results

Behavioral tests confirmed ALS-like phenotype. Firstly, we investigated the expected disease-related phenotypic changes characteristic for the animal model used in this study. Our goal was to assess the main turning points of the disease and characterize its progression.

To study the phenotype, we used two types of behavioral testing—the wire grid hang test and the rotarod performance test. We tested comparable groups of animals harboring SOD1(G93A) mutation (SOD1), and control animals (CTRL) with even numbers of males and females within each group. At the beginning of the testing period (1 month), all the animals performed for the maximum time (180 s) in both tests (see "Methods" section). The differences between CTRL and SOD1 animals were first noticeable in the wire grid hang test, where primarily the muscle strength is tested (Fig. 1a). The differences became significant at two months of age, so we considered this point an onset. The performance then slowly declined until a sudden drop at three months,

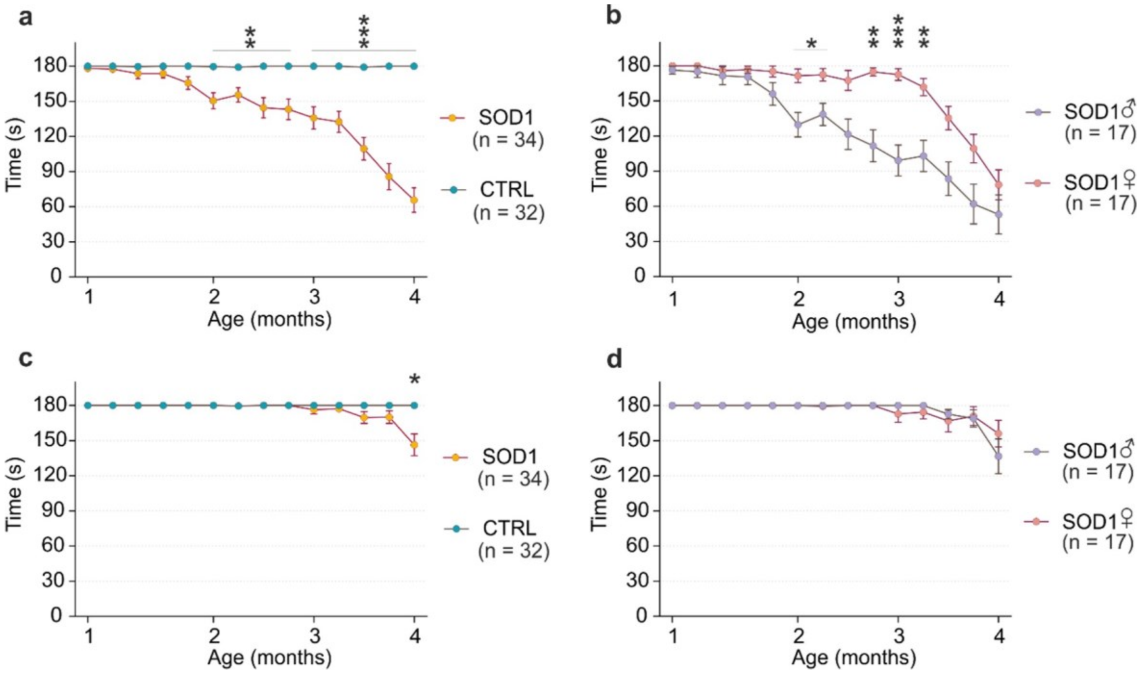

Figure 1. The cortical pathology evaluation by behavioral testing and immunohistochemistry. (**a**) The hanging wire test confirmed the motor skills decline in SOD1 animals during progression compared to the CTRLs. (**b**) Results from the hanging wire test comparing SOD1 animals divided based on sex revealed phenotypical differences in onset. (**c**), (**d**) The rotarod results comparing the CTRL and SOD1 animals did not reveal significant changes in progression. Statistical significance was determined using two-way ANOVA with Holm-Sidak's post-hoc test, error bars representing SEM. $^{*}p_{\text{adj}} \le 0.05$, $^{**}p_{\text{adj}} \le 0.01$, $^{***}p_{\text{adj}} \le 0.001$. n states the number of performing animals.

signaling the beginning of the symptomatic stage. This stage, accompanied by an even further performance decline, lasted approximately a month, after which the animals reached the end-stage marked by seriously impaired motor functions. The decrease in motor coordination of the animals measured by the rotarod (Fig. 1c) was only significant at the end-stage.

Investigating the SOD1 male versus female performance, the wire grid hang test revealed differences in the symptom onset and the progression in general (Fig. 1b). The onset in males appeared earlier, and overall they performed worse than the females, which is in agreement with human pathology[38]. However, despite the later onset, the female performance in the symptomatic stage declined faster than the male, resulting in similar results for both sexes at the end-stage. The rotarod measurements did not reveal any significant sex-related differences in motor coordination during the progression.

Thus, behavioral tests confirmed the characteristic features of the model, identified sex-related differences, and determined the four main time points of the disease, which we considered in the following experiments.

Identical cell populations were identified in the control and SOD1 mouse cortex using scRNA-seq.

The scRNA-seq experiment was designed as follows (Fig. 2a): CTRL and SOD1 mice were sacrificed at four time points, representing the main stages of the disease, with two males and two females used per condition at each time point. All cell suspensions were prepared from the motor and somatosensory cortical tissue and were enriched for three glial cell types—astrocytes, microglia, and oligodendrocytes—using FACS.

The scRNA-seq data followed an initial quality control, filtering, and clustering, and the resulting set of single cells was annotated using the expression of canonical marker genes of individual glial cell populations (Fig. 2b,d). As expected, the most numerous clusters in the data set were identified as astrocytes (*Aqp4*, *Aldh1l1*, *Gjb6*), microglia (*Cx3cr1*, *Aif1*), and oligodendrocytes (*Mobp*, *Apod*). Oligodendrocyte precursor cells (OPC) and committed oligodendrocyte precursor cells (COP) clustered separately from the mature oligodendrocytes that prevailed in the data set. The marker genes of these populations partially overlapped, indicating a gradual maturation of OPCs into oligodendrocytes (*Emid1*, *Pdgfra*, *Sox6*, *Vcan*, *Plp1*, *Cldn11* and others). In addition, perivascular macrophages, pericytes, and endothelial cells were present in the minority.

Each cell was assigned a sex identity based on the expression of X and Y chromosome-associated genes. Cells that did not fulfil the criteria for sex determination (see *Methods,* Supp. Fig. 1a, b) were excluded from further analyses. No cell cluster was overrepresented specifically in CTRL or SOD1, or in the male or female samples, confirming the robustness of cell preparation (Fig. 2c). Furthermore, the low proportion of mitochondrial reads and minimal activation of immediate early genes further validated the data quality (Supp. Fig. 1c, d). Overall, we successfully identified the targeted cell populations in the dataset and observed their equal proportions in both conditions and sexes.

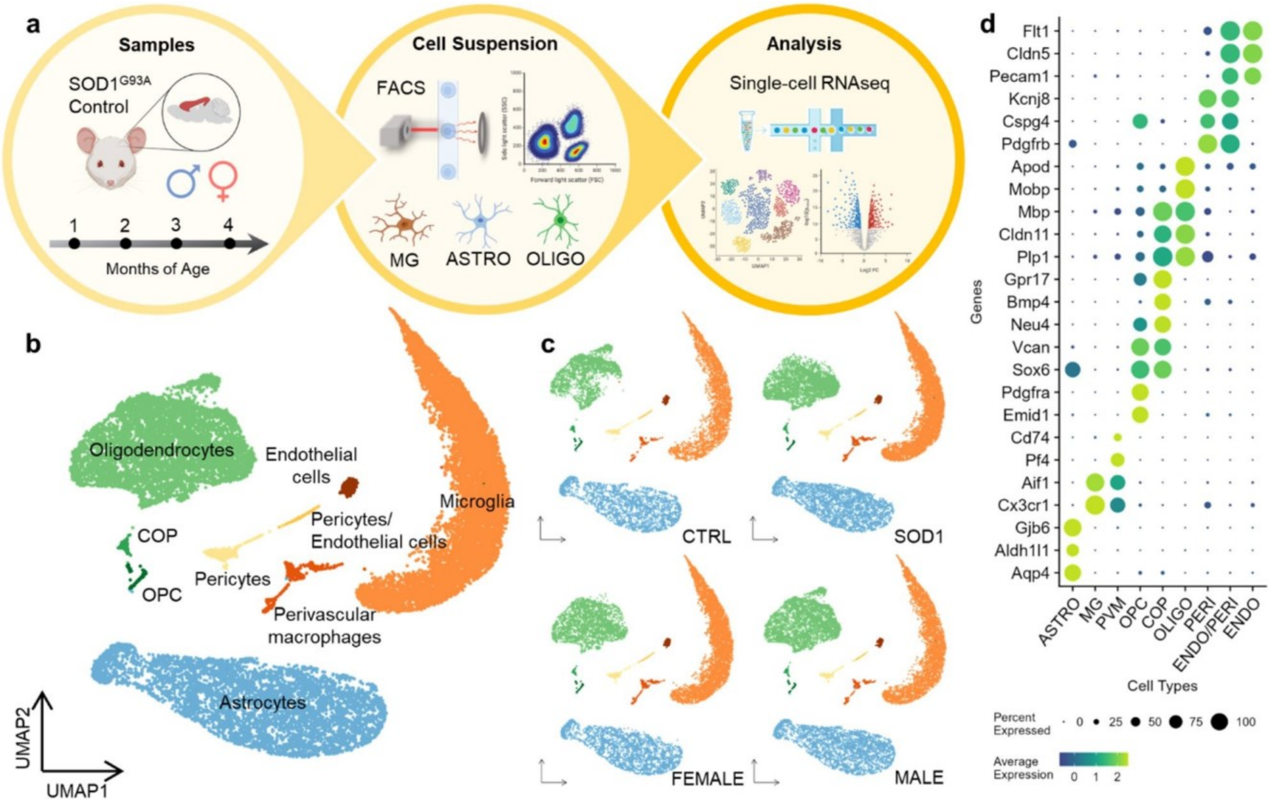

Figure 2. Single-cell RNA sequencing experiment overview. (**a**) A scheme summarizing the process of the sequencing experiment. (Created with BioRender.com) (**b**) A UMAP plot visualization of the identified cell clusters, containing cells from all samples. ASTRO n = 5536, MG n = 8429, OLIGO n = 6180, PVM n = 434, OPC n = 165, COP n = 98, PERI n = 395, ENDO n = 235, ENDO/PERI n = 108, total n = 21,580. (**c**) A visualization of cluster representation and the prevalence of targeted glia in both conditions and sexes. CTRL n = 7646, SOD1 n = 12,499, female n = 10,246, male n = 9899. (**d**) A list of canonical marker genes used for identification of cell clusters. ASTRO—astrocytes, MG—microglia, PVM—perivascular macrophages, OPC—oligodendrocyte precursor cells, COP—committed oligodendrocyte precursors, OLIGO—oligodendrocytes, PERI—pericytes, ENDO—endothelial cells.

The cortical glia of SOD1 mice showed minor changes in gene expression at the late stage of the ALS-like pathology. To provide a general view on the gene expression changes in SOD1 mice, each of the main cell types was subjected to PCA as a pseudobulk (Fig. 3a). The analysis revealed a minor alteration between the CTRL and SOD1 samples in both sexes during disease progression. The first apparent shift between the samples appeared at four months of age in microglia and oligodendrocytes, suggesting their reaction to ALS-like pathology. The SOD1 astrocytes, frequently reported to be activated in SOD1(G93A) and other models of ALS[14,18,19,39], remained unchanged and clustered with the CTRL samples. Notably, the clustering showed a displacement of three-month-old (3 M) male data points. This was most prominent in astrocytes, where it represented the highest source of variability (reflected by separation in PCA1). Exploring the source of the variability, we identified a minor cluster of cells within astrocytes and oligodendrocytes, which was only present in 3 M CTRL males (Supp. Fig. 2). The cluster was characterized by the expression of stress-related genes *Cdkn1a* and *Fkbp5*, which had the most extreme values of loadings in respective principal components (PCs) in the pseudobulk analysis, confirming the effect of the cluster on the displacement of 3 M CTRL male data points. As the presence of the cluster had a negligible effect on further analysis, we considered it as a technical artifact of sample processing and removed it from the dataset. This finding, however, showed the power of the single-cell analysis to characterize even minor changes in cell subpopulations, which might otherwise be hard to interpret in traditional bulk analysis.

Based on the sex-related differences in behavioral tests (Fig. 1a–d), we examined the potential ALS-associated gene expression variations between the sexes by DEA, and compared the male and female cells for CTRL and SOD1 separately. The analysis yielded only a few DEGs based on the set thresholds of $|\log_2FC| > 1$ and $p_{adj} < 0.05$. The X chromosome gene *Xist* was significantly upregulated in the females in all three cell types, regardless of genotype. The *Xist* gene plays a major role in the gene dosage compensation in females by silencing one of the X chromosomes, and is therefore expressed only in female cells[40]. Two genes encoded by chromosome Y (*Eif2s3y*, *Uty*) were upregulated in males, but the difference in their expression only exceeded the $\log_2FC$ threshold in astrocytes (Fig. 3b). Apart from these, no other dysregulated genes related to the pathology progression and sex were found in our data.

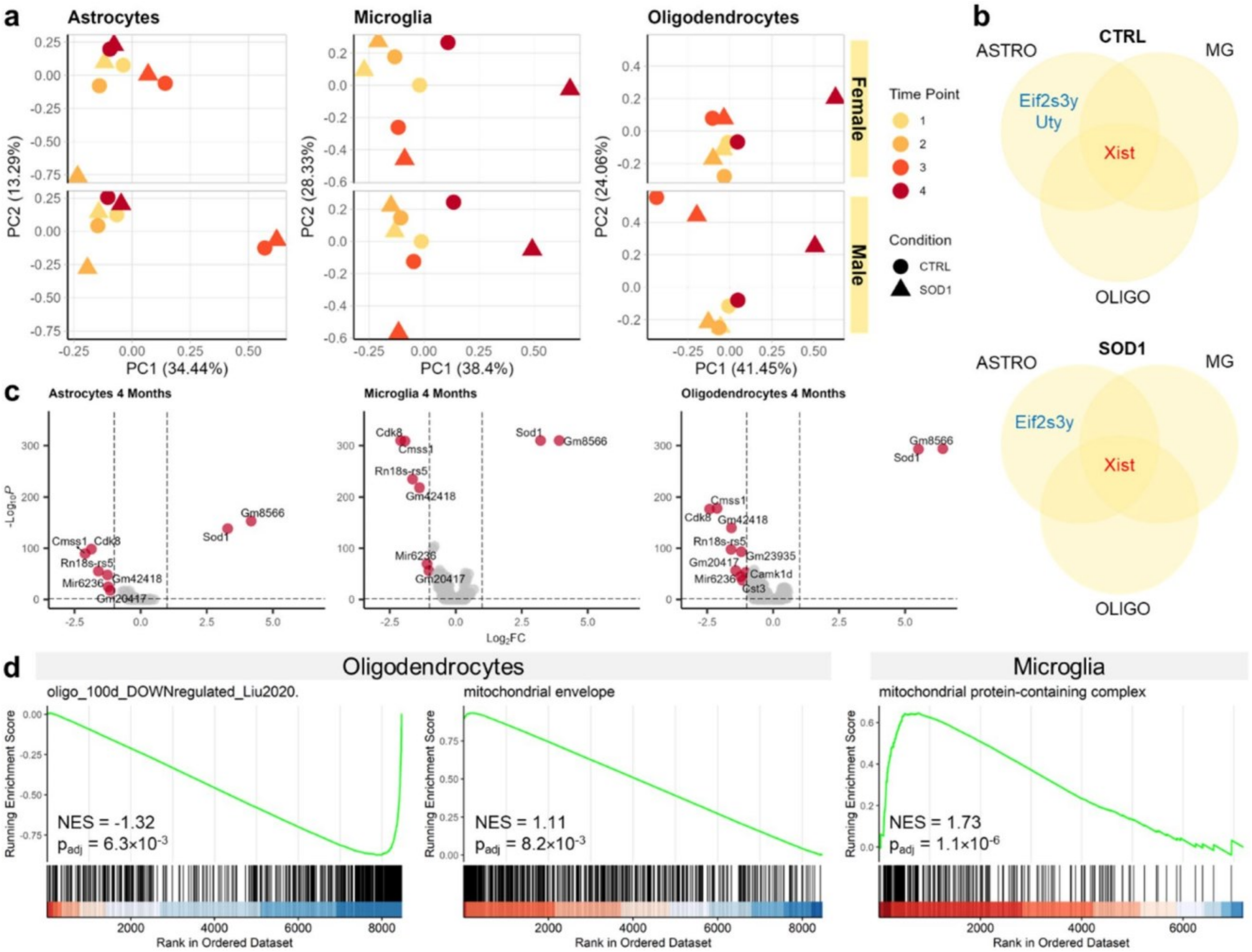

Figure 3. Pseudobulk and differential expression analysis reveals only minor changes in gene expression. (**a**) Pseudobulk PCA clustering comparison of male and female samples showing a shared reaction to the ongoing pathology in microglia and oligodendrocytes at 4 M. (**b**) A visualization of the few differentially expressed genes found dysregulated in males and females in all cell types at 4 M time point. *Xist* clearly distinguishes female cells, whereas *Eif2s3y* and *Uty* are both expressed by male chromosome Y. (**c**) Results of the DEA comparing CTRL and SOD1 4 M samples show a limited number of up- and downregulated genes at the final stage. (**d**) Enrichment curves visualising the results of the GSEA at 4 M. One reference gene set was enriched among genes downregulated in oligodendrocytes. Analysis of GO terms showed mitochondrial components to be enriched among genes upregulated in oligodendrocytes and microglia.

To investigate disease-related transcriptional changes, we performed the DEA on the comparisons of CTRL and SOD1 samples at each time point and for each cell type, considering males and females together. The *Sod1* gene was the only one significantly upregulated DEG in all the measured stages of the disease, including the end-stage as shown in Fig. 3c and Supp. Tab. 1 ($|\log_2 FC| > 1$, $p_{adj} < 0.05$), confirming the validity of the SOD1(G93A) model. Other dysregulated genes were mostly noncoding or ribosomal transcripts that evaded quality control. Additionally, the 4 M CTRL samples were marked by an increased expression of genes *Cdk8* and *Cmss1* across all cell types. These two genes were identified in the subsequent analysis as confounders negatively effecting sub-clustering results (Supp. Fig. 2a, b). Therefore, they were considered as biasing factors without connection to the ALS-like pathology. Together, these results show minimal variation in gene expression related to the pathology progression in the cortex of the SOD1(G93A) mouse, regardless of sex, with the indication of subtle changes in microglia and oligodendrocytes in the late phase of the disease.

The GSEA indicated an altered mitochondrial function in cortical microglia and oligodendrocytes of SOD1 mice.

To investigate the potential biological significance of the minimal changes in gene expression detected by DEA, we utilized the GSEA[32] focused on the most affected 4 M time point. As GSEA considers the expression of all genes, regardless of cut-offs in log2FC or p-value, it allows for the finding of any dysregulated processes even if the change of the individual genes is minor.

First, we employed a meta-analysis approach, and collected the gene signatures of glial cells affected by SOD1 mutation from 15 transcriptomic studies published in the last 20 years (Supp. Tab. 2). This set includes data mostly derived from the spinal cord of the SOD1(G93A) model. Using GSEA, we detected the enrichment of only a single gene set that was recently reported by Liu, et al.[15] as downregulated in brainstem oligodendrocytes in 100-day-old mice. In concordance, our results showed a negative enrichment in oligodendrocytes (NES = − 1.32, $p_{adj} = 6.3 \times 10^{-3}$; NES—normalized enrichment score; Fig. 3d), indicating small, but significant changes in the cortical 4 M SOD1 oligodendrocytes. No gene set was found enriched for microglia or astrocytes.

In addition to the meta-analysis, we also looked for Gene Ontology (GO) terms [41,42] enriched in our data. Two activated terms related to mitochondria turned out to be upregulated in our data set: *mitochondrial envelope* in oligodendrocytes (NES = 1.11, $p_{adj} = 8.2 \times 10^{-3}$) and *mitochondrial protein-containing complex* in microglia (NES = 1.73, $p_{adj} = 1.1 \times 10^{-6}$) (Fig. 3d). In support of our data, mitochondrial dysfunction has been extensively discussed as one of the factors contributing to ALS pathology, not only in relation to the mutant *Sod1* gene, but also to other ALS-linked genetic perturbations (reviewed in Jankovic et al.[43]).

Taken together, despite the low number of DEGs, we identified subtle changes in the mitochondria function in cortical oligodendrocytes and microglia. However, considering the number of enriched terms and their significance, the severity of the dysfunction is rather low.

The subpopulation analysis confirmed subtle changes in oligodendrocytes and microglia. As the pseudobulk analyses revealed only subtle variations in the gene expression of the SOD1(G93A) cortical glia, we speculated that the pathological changes could be represented by a small fraction of cells, hidden at the population level. Therefore, we conducted an in-depth sub-clustering analysis with the goal to identify subpopulations potentially playing a role in the disease progression.

Starting with astrocytes, we identified three clusters that were present in both the CTRL and SOD1 samples in a similar proportion (Fig. 4a). To annotate these clusters, we calculated their marker genes (Supp. Tab. 3) and visualized the gene signatures of astrocytic subtypes described by Habib et al.[5] in a mouse model of Alzheimer's disease (AD). The study identified two similar subpopulations of astrocytes expressing markers of reactivity – Gfap-High and DAAs. While Gfap-high were present in controls and in AD samples, DAAs were unique to the AD model, and the authors suggested their potential role in the disease progression. Marker genes of cluster 3 in our data partially overlapped with the markers of the Gfap-High cluster (e. g. genes *Mt1*, *Mt2*, *Id3*, *Cd9*, *Vim*), but we did not detect the DAAs specifically in SOD1 samples. Of note, *Gfap* and *Vim* expression levels were low, suggesting a limited pathological reaction of astrocytes in the cortex of the mutant SOD1(G93A) mice. This finding complies with the results of the pseudobulk analysis, showing no changes in astrocytes. Cluster 1 shared common genes with Gfap-low astrocytes (e. g. *Luzp2*, *Trpm3*), and the remaining cluster 2 expressed markers of both Gfap-High and Gfap-Low clusters, therefore representing an intermediate state cluster.

Microglia were grouped into four clusters as shown in the UMAP plot in Fig. 4b. Cluster 1 was characterized by the expression of homeostatic markers[3,36,37]. The gene signatures of microglia in clusters 2 and 3 resembled the expression profile of ARM, that were described in a model of AD, but also in a smaller proportion in a healthy brain[3,4]. These activated microglia characteristically downregulate homeostatic genes such as *Cx3cr1*, *P2ry12,* and *Sall1*, which is also noticeable in our data (Fig. 4b). Additionally, cluster 3 was marked by a higher expression of *Apoe*, which is a major regulator of microglial neurodegenerative phenotype[44]. Cluster 4 represented IRM[4], and was clearly distinguishable by the expression of *Ifit2*, *Ifit3,* and *Ifitm3*, the genes involved in the interferon response pathway. However, the proportion of IRM was very low in both conditions. Nevertheless, we detected a small increase in the subpopulation of activated microglia in SOD1 samples (cluster 2), suggesting a starting activation of microglia in response to pathological stimuli.

Oligodendrocytes formed four clusters (Fig. 4c). Cluster 1 shared a similar gene expression signature with myelin forming oligodendrocytes (MFOL) described by Marques, et al.[35], including the expression of *Mal*, *Plp1*, *Mog,* and *Opalin* genes. These cells were predominantly present at the one month (1 M) time point (Fig. 4d), which coincides with the extensive myelination in rodents during the early weeks after birth[45]. Cluster 2 represents mature oligodendrocytes (MOL2) expressing *Klk6*, but also mature oligodendrocyte marker *Apod* and genes typical for myelinating cells *Pmp22*, *S100b,* and *Apc*[7,35,46]. Floriddia et al.[7] reported the MOL2 population to be more abundant in the white matter of the spinal cord, but also to a lesser extent in the cortex[35]. The proportions in both conditions were similar for clusters 1 and 2. As for clusters 3 and 4, they showed an increased expression of several genes found in mature oligodendrocyte populations MOL5/6[7,35]. Interestingly, cluster 4 was present almost exclusively in the SOD1 samples (Fig. 4d), and it was characterized by a higher expression of *Apoe* and *Il33*. *Il33* is upregulated in oligodendrocytes and astrocytes in lesions and can be released by stressed or damaged cells. It has an anti-inflammatory effect and promotes the activation of microglia (reviewed in Sun et al.[47]). Upregulation of *Ill33* has been previously reported in disease-associated oligodendrocytes in a mouse model of AD[48,49]. *Apoe* was identified as a marker gene of immune oligodendroglia (ImOLG)[50], which were enriched in multiple sclerosis lesions, suggesting their role in chronic demyelination and continuous attempts to remyelinate[51]. Thus, we hypothesize that cluster 4 represents a damaged or reactive state of oligodendrocytes, responding to the pathological stimuli in the 4 M SOD1 cortex. It is tempting to speculate whether the small increase in numbers of activated microglia and possibly the shift to the intermediate state in astrocytes that we observed in the SOD1 (Fig. 4a,b, respectively) might be a response to the damaged/activated oligodendrocytes. This kind of interaction between disease-associated states of glial cells was recently described in AD[52], and also in ALS[2].

Overall, we were able to identify multiple subpopulations of astrocytes, microglia, and oligodendrocytes, and we recognized the gene expression patterns of specific, previously described, cellular subtypes. However, in contrast with our expectations, we did not detect any disease-associated subpopulations in the SOD1 samples, apart from the damaged/activated oligodendrocytes.

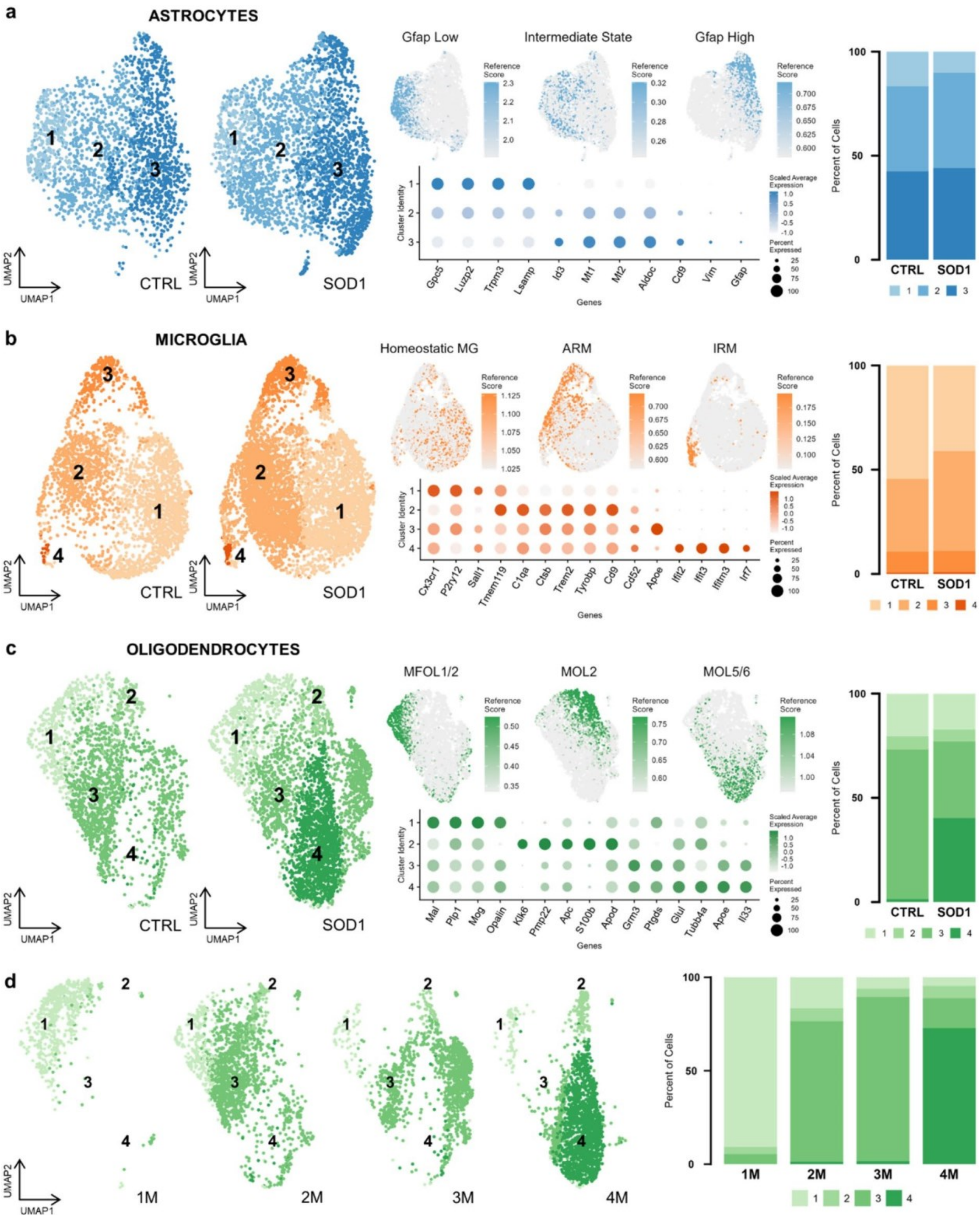

Figure 4. The subpopulation analysis revealed a unique subpopulation of oligodendrocytes in SOD1 samples. UMAP visualization of subpopulations of astrocytes (n = 5292) (**a**), microglia (n = 8414) (**b**), and oligodendrocytes (n = 5876) (**c**) split to CTRL and SOD1 condition (left), including cells from all four time points. Gene expression signatures of previously described subpopulations are shown projected onto UMAP (middle-top). A list of representative cluster markers used for their annotation (middle-bottom). Proportions of subpopulations in CTRL and SOD1 (right), including cells from all four time points. (**d**) UMAP visualization of CTRL and SOD1 oligodendrocytes split according to age (1 M: n = 682, 2 M: n = 1697, 3 M: n = 1430, 4 M: n = 2067). Bar plot shows proportions of subpopulations at each time point.

The immunohistochemical identification of changes in the cortical and spinal glia of SOD1 mice. The results of the scRNA-seq analysis suggested minor changes in the cortical glia of the SOD1(G93A) mouse model. To further explore and validate this conclusion, we conducted an immunohistochemical analysis of glia in the motor and primary somatosensory cortex (the identical region used for the sequencing) at the 4 M time point, when the phenotypic changes are the most pronounced. The imaged zones within areas of interest are represented in Fig. 5a. As the morphological changes are well described in the spinal cord, we also stained the lumbar region of the spinal cord at the end-stage (4 M), and used those pictures as a reference for advanced gliosis in our animals.

Astrocytes were stained using ALDH1L1 marker, which allowed the inspection of the whole cell morphology, including the processes. Astrogliosis, a morphological change marked by enlargement of the cellular body and shortened, thickened processes, is a characteristic response of astrocytes in pathological states, and it was well described in the ALS spinal cord[13,14]. In the cortex we conducted fluorescence analysis in order to find any morphological differences (Fig. 5b), but the analysis showed very similar fluorescence values of both SOD1 and CTRL astrocytes, suggesting there is no cell enlargement associated with activation. The similar morphology can be seen in Fig. 5c in comparison with astrocytes in the ventral horns of the spinal lumbar region, which showed an enlarged body with distinctively shortened processes. The results from fluorescence analysis align with little or no change detected in astrocytes at the level of gene expression.

Microglia, like astrocytes, change their morphology in response to pathological stimuli. They retract processes and adopt a specific amoebic shape, typical for their activated state. To visualize microglia, we used IBA1 antibody and stained both the cortex and lumbar spinal cord for comparison. The Sholl analysis we used to evaluate the changes in morphology (Fig. 5d) is frequently conducted to quantify the complexity of cell´s arborization. The analysis confirmed that the SOD1 cortical microglia morphology does not significantly differs from CTRL animals. We did not detect shorter processes or reduced branching, which would suggest activated phenotype. However, during the analysis we noticed some tips of the processes looking bulbous and enlarged (Fig. 5e). These structures, called *bulbous termini*, appear as the microglia's first reaction after injury[53], and may represent an initial phase of microglia activation observed in the transcriptomic data. The SOD1 microglia in the ventral horns of the spinal cord on the other hand display the typical amoebic shape with very short and thickened processes associated with activation.

The previous analysis identified a SOD1-specific oligodendrocyte cluster (cluster 4) suggesting a certain portion of cells as being apoptotic, we thus focused on the protein expression changes related to chronic demyelination, necrosis, or apoptosis. Accordingly, we stained for myelin basic protein (MBP)—a marker of myelination, adenomatous polyposis coli (APC)—a marker of adult oligodendrocytes, and cleaved caspase 3 (CC3)—an apoptotic marker. The quantification of MBP signal intensity as well as the number of APC + oligodendrocytes in the cortex of the SOD1 animals excluded the demyelination processes as there was no significant decrease of MBP or APC + cells compared to the CTRLs (Fig. 5f). Similarly, the co-staining of CC3 with APC did not reveal a different abundance of CC3 + oligodendrocytes in either the SOD1 or CTRLs, suggesting a similar rate of apoptosis (Fig. 5f). MBP staining and representative image of a cell positive for APC and CC3 can be found in Fig. 5g. Collectively, the data showed no significant demyelination or degeneration of oligodendrocytes, therefore it is likely that the SOD1-specific cluster 4 identified in scRNA-seq in 4 M animals does not represent dying or damaged cells.

Taken together, we did not detect any profound morphological changes in the cortical glia of the SOD1 mice. Oligodendrocytes did not show an increased cell death or loss of MBP protein, suggesting its maintained function in the cortex of the ALS mice.

Discussion

ALS is a devastating neurodegenerative disease with fast progression and no effective treatment strategies. Although it is primarily recognized as a motor-neuron disease, the other cell types, including glial cells, contribute to the disease progression and thus represent a potential target for future therapies. In the past, multiple experimental models have been developed to understand the mechanisms of the disease, as well as to facilitate the search for therapeutic targets. Among them, the SOD1(G93A) mouse model has the prime position as the best-characterized mouse strain used in current ALS research. Despite its long-term application, the effect of the pathological changes across different CNS regions is still not fully understood.

The pathological effect on cortex is of special interest due to its role in the planning, control, and execution of voluntary movements, which are severely affected by ALS. Pathological changes in the cortex of ALS patients have been reported since the first description of the disease in 1869, and the monitoring of cortical structural abnormalities became a standard ALS diagnostic procedure[54]. Along with cortical MN death, changes in glia have also been observed, including microgliosis[11,55–57], accompanied by the DAM-like gene expression signature[56], demyelination[8], and change of oligodendrocyte function from myelinating to neuro-supportive[57].

While the changes are well documented in humans, less is known about the effect of the ALS-like pathology on the cortex of the SOD1 models. In the SOD1(G93A) model, the cortical MN degeneration was observed early by Özdinler et al.[17] and others, together with the changes in glia[18–20]. Reactive astrocytes in the SOD1(G93A) cortex were shown to differ from their spinal counterparts, while still maintaining a toxic effect on neurons[18,19,58]. However, Gomes et al.[19] also reported no significant gene expression changes in microglia or oligodendrocytes. Moreover, others suggested the pathology in the SOD1 model as being restricted to only spinal and bulbar motor neurons, not affecting the motor cortex[21]. Thus, such opposing data raise questions as to what extent the cortex is affected in the SOD1 mouse model, and how well this model recapitulates the cortical pathology in humans.

To fill this knowledge gap, we applied single-cell RNA sequencing supported by immunohistochemistry to detect gene expression changes, the presence of disease-associated cell populations, and morphological or

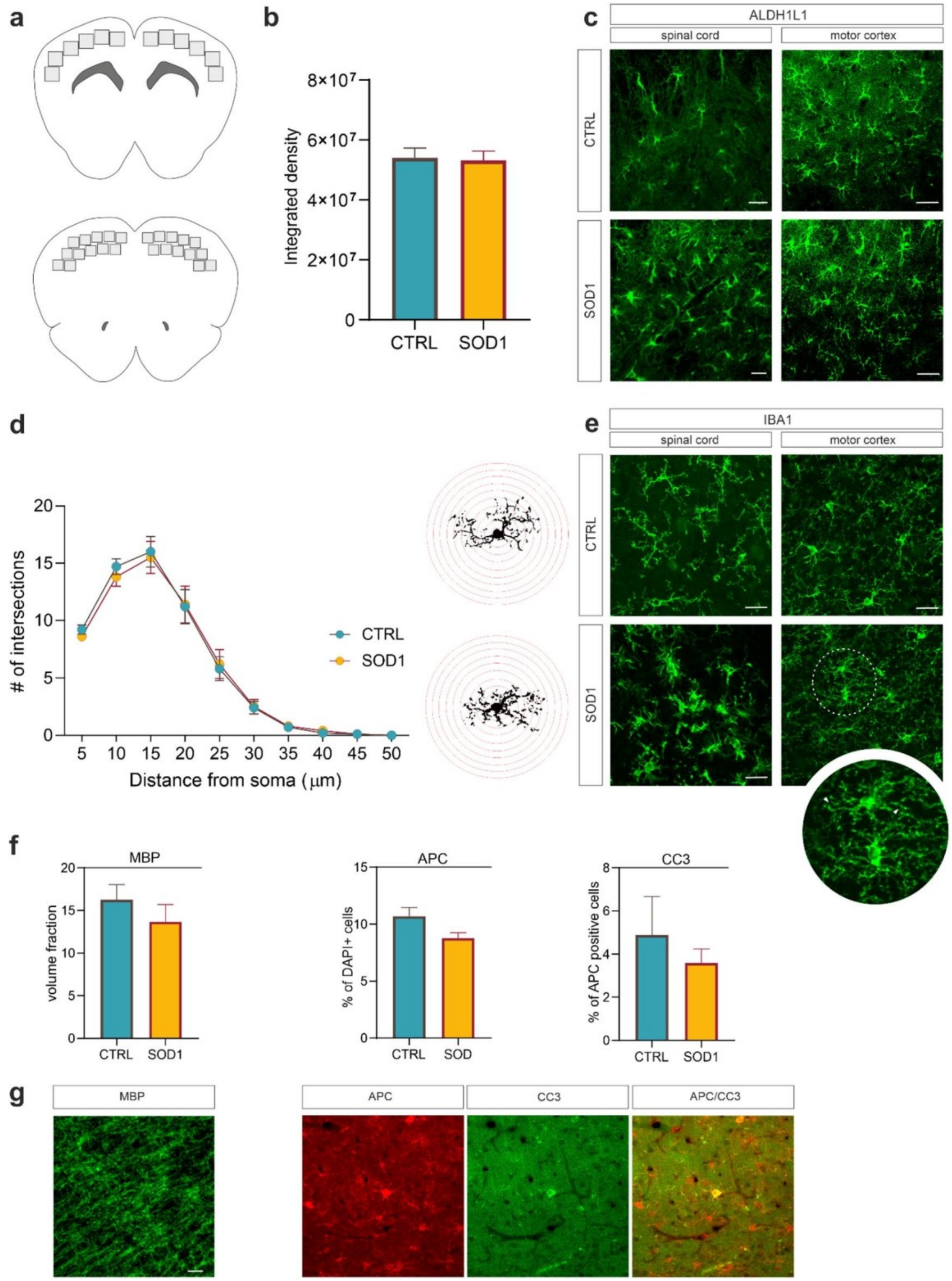

Figure 5. The immunohistochemistry (**a**) An upper cartoon depicts 12 areas scanned for the investigation of morphological changes and quantification of APC and CC3. Lower cartoon shows 24 areas scanned for the MBP analysis. (**b**) Fluorescence analysis did not reveal any significant differences in morphology between cortical astrocytes in SOD1 (n=6) and CTRL (n=6) animals. (**c**) Representative pictures of ALDH1L1 staining in cortex and spinal cord comparing astrocytes show morphological difference between SOD1 and CTRL in the spinal cord but no noticeable difference in the cortex. (**d**) The results of Sholl analysis indicated very similar microglia complexity in both CTRL (n=6) and SOD1 (n=6) samples. Scholl masks with red concentric radii depict single thresholded microglia as they were used for the analysis. (**e**) Representative images of cortical and spinal slices stained with IBA1 show evident amoebic morphology of spinal microglia but only subtle morphological changes represented by *bulbous termini* (see close up) in the cortex. (**f**) The quantification of MBP in the cortex revealed insignificant difference between SOD1 (n=6) and CTRLs (n=6). The number of APC+cells was consistent between SOD1 (n=3) and CTRLs (n=3) and the number of APC+cells co-stained with CC3 used as a marker of apoptosis in oligodendrocytes also remained similar, suggesting no apparent oligodendrocyte degenerations. (**g**) Representative images of MBP, APC, and CC3 staining Scale bars, 20 μm. The statistical significance was determined using unpaired t-test. Error bars represent SEM. n states the number of used animals.

other pathological modifications in cortical glia accompanying the ALS-like pathology in the SOD1(G93A) mouse model. The ALS-like phenotype was confirmed by behavioral testing, including sex-dependent differences in disease progression as reported by McCombe and Henderson[38]. The results of scRNA-seq focused on glia revealed minor changes in microglia and oligodendrocytes, and showed no significant ALS-related shift in astrocytes, which contradicts several studies reporting the reactive phenotype of astrocytes[18,19,58]. Although the only significantly dysregulated gene in the SOD1(G93A) model was *Sod1*, GSEA indicated the mitochondrial dysfunction in microglia and oligodendrocytes. Similar changes have recently been observed by Liu et al.[15] in the oligodendrocytes isolated from the brainstem of 100-day-old SOD1 mice, suggesting the possible dysregulation of energetic pathways.

As our data were generated within the motor and primary somatosensory cortex, representing an end-point region of corticospinal tract affected by ALS, they allow basic questions to be addressed regarding the site of origin and the direction of ALS progression. Currently, there are two hypotheses, both supported by lines of evidence (reviewed in van den Bos et al.[59]). The 'dying forward' hypothesis suggests ALS originates in the cortex and spreads towards the spinal MNs. On the other hand, the 'dying back' hypothesis proposes ALS begins within muscles or neuromuscular junctions. Considering the advanced ALS-like phenotype of the end-stage SOD1 mice and the more pronounced changes in the brainstem and the spinal cord observed elsewhere, the milder changes in the cortex indicated by our data are more in favor of the 'dying back' hypothesis in SOD1(G93A) mice. Interestingly, this contrasts with a report from Burg et al.[60], which indicates the cortex as the initiating point of ALS in SOD1(G86R) mice. The contradictory data might suggest a differential effect of specific point mutations on the character of the disease, requiring further investigation.

Many of the previous reports exploring the effect of the SOD1 mutation on motor cortex relied on measuring the limited number of genes and proteins[19,20,55], or analysis of the bulk population of cells[18,61]. This consequently decreased the sensitivity of the analysis and limited the interpretability of the data. In this study, we used high-throughput scRNA-seq, allowing for an in-depth analysis of small cell populations that cannot be distinguished by bulk approaches. Using scRNA-seq, recent seminal studies revealed various disease-associated populations of glia, playing a major role in the disease progression[3–6]. Interestingly, many of these populations are present in multiple diseases, suggesting common mechanisms employed by glial cells in response to pathological stimuli. For example, a DAM-like population was identified not only in Alzheimer's disease, but also in the spinal cord of the SOD1(G93A) mouse[3], and in a spinal cord injury model[62]. In our work, we searched for these populations without any success, which confirmed the minimal changes observed at bulk transcriptional level, as well as by immunohistochemistry. We mostly found similar cellular composition between the control and SOD1(G93A) animals, except for microglia and oligodendrocytes. In the case of microglia, we observed a little increase in the proportion of the activated microglia, suggesting a starting phase of their activation. The data were completed by immunohistochemistry revealing *bulbous termini* on microglial processes. More apparent changes were observed in oligodendrocytes, where sub-clustering analysis identified the existence of a unique population of oligodendrocytes, characterized by an increased expression of *Apoe* and *Il33*, and enriched specifically in 4 M SOD1 samples. Considering no profound loss of oligodendrocytes or a higher apoptotic rate in immunohistochemistry, we could speculate about the active role of this population of oligodendrocytes in disease progression. This is also in line with recent evidence suggesting the active role of oligodendrocytes in the progression of multiple sclerosis[6] and in aging white matter[63], which contrasts with their widely accepted passive role. Notably, we did not observe any expression patterns similar to previously reported disease-associated oligodendrocytes[6,48–50], except *Apoe* or *Il33* mentioned above. However, this might be related to the overall mild changes in gene expression observed throughout our data.

In conclusion, our study demonstrates that cortical glia are only subtly affected in the SOD1(G93A) model, even at the very end-stage of disease. Furthermore, owing to the power of scRNA-seq, we showed that oligodendrocytes potentially actively participate in the pathology, emphasizing the importance of addressing their role in further research. Finally, on reflection of our results, we suggest that the SOD1(G93A) mouse model does not fully recapitulate the human disease and we recommend using a different model system for studying the cortical ALS pathology.

Conclusions

Collectively, our results suggest the ALS-like pathological changes present in the sensorimotor cortex of SOD1(G93A) mice are minimal. There is an ongoing discussion in the field whether the model mimics the disease completely including the pathology occurring in the cortex and the published results are disputable. Our collective findings inspecting glial cells on multiple levels did not reveal any significant changes of SOD1 astrocytes and only subtle changes of microglia and oligodendrocytes at the final stage. The changes of microglia and oligodendrocytes suggest starting activation linked to the pathology, but the extent of change does not correspond to the pathology described in human tissue. The SOD1 specific oligodendrocytes identified at the final stage, however, contribute to the recently published evidence reporting their active role in neurodegeneration, largely rejecting long-lasting dogma presenting oligodendrocytes as solely passive in the CNS diseases. However, despite the signs of activation, the effect of ALS-like pathology on the glial cells in the cortex of SOD1(G93A) mice is minor and our data provide supporting evidence against the use of this model for studying cortical pathology of ALS.

Data availability

The scRNA-seq data generated during this current study are available in NCBI's Gene Expression Omnibus[64] and are accessible through GEO Series accession number GSE206330 (https://www.ncbi.nlm.nih.gov/geo/query/acc.cgi?acc=GSE206330).

Received: 25 October 2022; Accepted: 15 April 2023

References

1. Baufeld, C., O'Loughlin, E., Calcagno, N., Madore, C. & Butovsky, O. Differential contribution of microglia and monocytes in neurodegenerative diseases. *J. Neural Transm. (Vienna)* **125**, 809–826. https://doi.org/10.1007/s00702-017-1795-7 (2018).
2. Maniatis, S. *et al.* Spatiotemporal dynamics of molecular pathology in amyotrophic lateral sclerosis. *Science* **364**, 89–93. https://doi.org/10.1126/science.aav9776 (2019).
3. Keren-Shaul, H. *et al.* A Unique microglia type associated with restricting development of Alzheimer's disease. *Cell* **169**, 1276-1290 e1217. https://doi.org/10.1016/j.cell.2017.05.018 (2017).
4. Sala Frigerio, C. *et al.* The major risk factors for Alzheimer's disease: Age, sex, and genes modulate the microglia response to aβ plaques. *Cell Rep.* **27**, 1293-1306 e1296. https://doi.org/10.1016/j.celrep.2019.03.099 (2019).
5. Habib, N. *et al.* Disease-associated astrocytes in Alzheimer's disease and aging. *Nat. Neurosci.* **23**, 701–706. https://doi.org/10.1038/s41593-020-0624-8 (2020).
6. Falcao, A. M. *et al.* Disease-specific oligodendrocyte lineage cells arise in multiple sclerosis. *Nat. Med.* **24**, 1837–1844. https://doi.org/10.1038/s41591-018-0236-y (2018).
7. Floriddia, E. M. *et al.* Distinct oligodendrocyte populations have spatial preference and different responses to spinal cord injury. *Nat. Commun.* **11**, 5860. https://doi.org/10.1038/s41467-020-19453-x (2020).
8. Kang, S. H. *et al.* Degeneration and impaired regeneration of gray matter oligodendrocytes in amyotrophic lateral sclerosis. *Nat. Neurosci.* **16**, 571–579. https://doi.org/10.1038/nn.3357 (2013).
9. Philips, T. *et al.* Oligodendrocyte dysfunction in the pathogenesis of amyotrophic lateral sclerosis. *Brain* **136**, 471–482. https://doi.org/10.1093/brain/aws339 (2013).
10. Zürcher, N. R. *et al.* Increased in vivo glial activation in patients with amyotrophic lateral sclerosis: Assessed with [(11)C]-PBR28. *Neuroimage Clin.* **7**, 409–414. https://doi.org/10.1016/j.nicl.2015.01.009 (2015).
11. Nolan, M. *et al.* Quantitative patterns of motor cortex proteinopathy across ALS genotypes. *Acta Neuropathol. Commun.* **8**, 98. https://doi.org/10.1186/s40478-020-00961-2 (2020).
12. Gurney, M. E. *et al.* Motor neuron degeneration in mice that express a human Cu, Zn superoxide dismutase mutation. *Science* **264**, 1772–1775. https://doi.org/10.1126/science.8209258 (1994).
13. Miller, S. J., Zhang, P. W., Glatzer, J. & Rothstein, J. D. Astroglial transcriptome dysregulation in early disease of an ALS mutant SOD1 mouse model. *J. Neurogenet.* **31**, 37–48. https://doi.org/10.1080/01677063.2016.1260128 (2017).
14. Guttenplan, K. A. *et al.* Knockout of reactive astrocyte activating factors slows disease progression in an ALS mouse model. *Nat. Commun.* **11**, 3753. https://doi.org/10.1038/s41467-020-17514-9 (2020).
15. Liu, W. *et al.* Single-cell RNA-seq analysis of the brainstem of mutant SOD1 mice reveals perturbed cell types and pathways of amyotrophic lateral sclerosis. *Neurobiol. Dis.* **141**, 104877. https://doi.org/10.1016/j.nbd.2020.104877 (2020).
16. MacLean, M., Lopez-Diez, R., Vasquez, C., Gugger, P. F. & Schmidt, A. M. Neuronal-glial communication perturbations in murine SOD1(G93A) spinal cord. *Commun. Biol.* **5**, 177. https://doi.org/10.1038/s42003-022-03128-y (2022).
17. Özdinler, P. H. *et al.* Corticospinal motor neurons and related subcerebral projection neurons undergo early and specific neurodegeneration in hSOD1G(9)(3)A transgenic ALS mice. *J. Neurosci.* **31**, 4166–4177. https://doi.org/10.1523/JNEUROSCI.4184-10.2011 (2011).
18. Miller, S. J., Glatzer, J. C., Hsieh, Y. C. & Rothstein, J. D. Cortical astroglia undergo transcriptomic dysregulation in the G93A SOD1 ALS mouse model. *J. Neurogenet.* **32**, 322–335. https://doi.org/10.1080/01677063.2018.1513508 (2018).
19. Gomes, C. *et al.* Cortical neurotoxic astrocytes with early ALS pathology and miR-146a deficit replicate gliosis markers of symptomatic SOD1G93A mouse model. *Mol. Neurobiol.* **56**, 2137–2158. https://doi.org/10.1007/s12035-018-1220-8 (2019).
20. Migliarini, S. *et al.* Microglia morphological changes in the motor cortex of hSOD1(G93A) transgenic ALS mice. *Brain Sci.* https://doi.org/10.3390/brainsci11060807 (2021).
21. Niessen, H. G. *et al.* In vivo quantification of spinal and bulbar motor neuron degeneration in the G93A-SOD1 transgenic mouse model of ALS by T2 relaxation time and apparent diffusion coefficient. *Exp. Neurol.* **201**, 293–300. https://doi.org/10.1016/j.expneurol.2006.04.007 (2006).
22. Schindelin, J. *et al.* Fiji: An open-source platform for biological-image analysis. *Nat. Methods* **9**, 676–682. https://doi.org/10.1038/nmeth.2019 (2012).
23. Ferreira, T. A. *et al.* Neuronal morphometry directly from bitmap images. *Nat. Methods* **11**, 982–984. https://doi.org/10.1038/nmeth.3125 (2014).
24. Wu, Y. E., Pan, L., Zuo, Y., Li, X. & Hong, W. Detecting activated cell populations using single-cell RNA-seq. *Neuron* **96**, 313-329 e316. https://doi.org/10.1016/j.neuron.2017.09.026 (2017).
25. Kantzer, C. G. *et al.* Anti-ACSA-2 defines a novel monoclonal antibody for prospective isolation of living neonatal and adult astrocytes. *Glia* **65**, 990–1004. https://doi.org/10.1002/glia.23140 (2017).
26. Dobin, A. *et al.* STAR: Ultrafast universal RNA-seq aligner. *Bioinformatics* **29**, 15–21. https://doi.org/10.1093/bioinformatics/bts635 (2013).
27. Lun, A. T. L. *et al.* EmptyDrops: Distinguishing cells from empty droplets in droplet-based single-cell RNA sequencing data. *Genome Biol.* **20**, 63. https://doi.org/10.1186/s13059-019-1662-y (2019).
28. Hao, Y. *et al.* Integrated analysis of multimodal single-cell data. *Cell* **184**, 3573-3587 e3529. https://doi.org/10.1016/j.cell.2021.04.048 (2021).
29. McGinnis, C. S., Murrow, L. M. & Gartner, Z. J. DoubletFinder: Doublet detection in single-cell RNA sequencing data using artificial nearest neighbors. *Cell Syst* **8**, 329-337 e324. https://doi.org/10.1016/j.cels.2019.03.003 (2019).
30. Marsh, S. E. *et al.* Single cell sequencing reveals glial specific responses to tissue processing & enzymatic dissociation in mice and humans. Preprint at: https://www.biorxiv.org/content/https://doi.org/10.1101/2020.1112.1103.408542v408541 (2020).
31. Young, M. D. & Behjati, S. SoupX removes ambient RNA contamination from droplet-based single-cell RNA sequencing data. *Gigascience* https://doi.org/10.1093/gigascience/giaa151 (2020).
32. Subramanian, A. *et al.* Gene set enrichment analysis: A knowledge-based approach for interpreting genome-wide expression profiles. *Proc. Natl. Acad. Sci. U. S. A.* **102**, 15545–15550. https://doi.org/10.1073/pnas.0506580102 (2005).
33. Yu, G., Wang, L. G., Yan, G. R. & He, Q. Y. DOSE: An R/Bioconductor package for disease ontology semantic and enrichment analysis. *Bioinformatics* **31**, 608–609. https://doi.org/10.1093/bioinformatics/btu684 (2015).
34. Wu, T. *et al.* clusterProfiler 4.0: A universal enrichment tool for interpreting omics data. *Innovation (N Y)* **2**, 100141. https://doi.org/10.1016/j.xinn.2021.100141 (2021).
35. Marques, S. *et al.* Oligodendrocyte heterogeneity in the mouse juvenile and adult central nervous system. *Science* **352**, 1326–1329. https://doi.org/10.1126/science.aaf6463 (2016).
36. Mathys, H. *et al.* Temporal tracking of microglia activation in neurodegeneration at single-cell resolution. *Cell Rep.* **21**, 366–380. https://doi.org/10.1016/j.celrep.2017.09.039 (2017).
37. Butovsky, O. & Weiner, H. L. Microglial signatures and their role in health and disease. *Nat. Rev. Neurosci.* **19**, 622–635. https://doi.org/10.1038/s41583-018-0057-5 (2018).

38. McCombe, P. A. & Henderson, R. D. Effects of gender in amyotrophic lateral sclerosis. *Gend. Med.* **7**, 557–570. https://doi.org/10.1016/j.genm.2010.11.010 (2010).
39. Ziff, O. J. *et al.* Meta-analysis of human and mouse ALS astrocytes reveals multi-omic signatures of inflammatory reactive states. *Genome Res.* **32**, 71–84. https://doi.org/10.1101/gr.275939.121 (2022).
40. Loda, A. & Heard, E. Xist RNA in action: Past, present, and future. *PLoS Genet.* **15**, e1008333. https://doi.org/10.1371/journal.pgen.1008333 (2019).
41. Ashburner, M. *et al.* Gene ontology: Tool for the unification of biology. The Gene Ontology Consortium. *Nat. Genet.* **25**, 25–29. https://doi.org/10.1038/75556 (2000).
42. Gene Ontology Consortium. The gene ontology resource: Enriching a GOld mine. *Nucleic Acids Res.* **49**, D325–D334. https://doi.org/10.1093/nar/gkaa1113 (2021).
43. Jankovic, M. *et al.* Current concepts on genetic aspects of mitochondrial dysfunction in amyotrophic lateral sclerosis. *Int. J. Mol. Sci.* https://doi.org/10.3390/ijms22189832 (2021).
44. Krasemann, S. *et al.* The TREM2-APOE pathway drives the transcriptional phenotype of dysfunctional microglia in neurodegenerative diseases. *Immunity* **47**, 566-581 e569. https://doi.org/10.1016/j.immuni.2017.08.008 (2017).
45. Doretto, S. *et al.* Oligodendrocytes as regulators of neuronal networks during early postnatal development. *PLoS One* **6**, e19849. https://doi.org/10.1371/journal.pone.0019849 (2011).
46. Su, X., Vasilkovska, T., Frohlich, N. & Garaschuk, O. Characterization of cell type-specific S100B expression in the mouse olfactory bulb. *Cell Calcium* **94**, 102334. https://doi.org/10.1016/j.ceca.2020.102334 (2021).
47. Sun, Y. *et al.* Therapeutic opportunities of interleukin-33 in the central nervous system. *Front Immunol.* **12**, 654626. https://doi.org/10.3389/fimmu.2021.654626 (2021).
48. Kenigsbuch, M. *et al.* A shared disease-associated oligodendrocyte signature among multiple CNS pathologies. *Nat. Neurosci.* **25**, 876–886. https://doi.org/10.1038/s41593-022-01104-7 (2022).
49. Lee, S. H. *et al.* TREM2-independent oligodendrocyte, astrocyte, and T cell responses to tau and amyloid pathology in mouse models of Alzheimer disease. *Cell Rep.* **37**, 110158. https://doi.org/10.1016/j.celrep.2021.110158 (2021).
50. Jäkel, S. *et al.* Altered human oligodendrocyte heterogeneity in multiple sclerosis. *Nature* **566**, 543–547. https://doi.org/10.1038/s41586-019-0903-2 (2019).
51. Berghoff, S. A. *et al.* Neuronal cholesterol synthesis is essential for repair of chronically demyelinated lesions in mice. *Cell Rep.* **37**, 109889. https://doi.org/10.1016/j.celrep.2021.109889 (2021).
52. Cain, A. *et al.* Multi-cellular communities are perturbed in the aging human brain and with Alzheimer's disease. Preprint at: https://www.biorxiv.org/content/https://doi.org/10.1101/2020.1112.1122.424084v424081 (2020).
53. Davalos, D. *et al.* ATP mediates rapid microglial response to local brain injury in vivo. *Nat. Neurosci.* **8**, 752–758. https://doi.org/10.1038/nn1472 (2005).
54. Vucic, S., Pavey, N., Haidar, M., Turner, B. J. & Kiernan, M. C. Cortical hyperexcitability: Diagnostic and pathogenic biomarker of ALS. *Neurosci. Lett.* **759**, 136039. https://doi.org/10.1016/j.neulet.2021.136039 (2021).
55. Jara, J. H. *et al.* Evidence for an early innate immune response in the motor cortex of ALS. *J. Neuroinflamm.* **14**, 129. https://doi.org/10.1186/s12974-017-0896-4 (2017).
56. Dols-Icardo, O. *et al.* Motor cortex transcriptome reveals microglial key events in amyotrophic lateral sclerosis. *Neurol. Neuroimmunol. Neuroinflamm.* https://doi.org/10.1212/NXI.0000000000000829 (2020).
57. Limone, F. *et al.* Single-nucleus sequencing reveals enriched expression of genetic risk factors sensitises motor neurons to degeneration in ALS. Preprint at: https://www.biorxiv.org/content/https://doi.org/10.1101/2021.1107.1112.452054v452051 (2021).
58. Gomes, C. *et al.* Astrocyte regional diversity in ALS includes distinct aberrant phenotypes with common and causal pathological processes. *Exp. Cell Res.* **395**, 112209. https://doi.org/10.1016/j.yexcr.2020.112209 (2020).
59. van den Bos, M. A. J., Geevasinga, N., Higashihara, M., Menon, P. & Vucic, S. Pathophysiology and diagnosis of ALS: Insights from advances in neurophysiological techniques. *Int. J. Mol. Sci.* https://doi.org/10.3390/ijms20112818 (2019).
60. Burg, T. *et al.* Absence of subcerebral projection neurons is beneficial in a mouse model of amyotrophic lateral sclerosis. *Ann. Neurol.* **88**, 688–702. https://doi.org/10.1002/ana.25833 (2020).
61. Phatnani, H. P. *et al.* Intricate interplay between astrocytes and motor neurons in ALS. *Proc. Natl. Acad. Sci. U. S. A.* **110**, E756-765. https://doi.org/10.1073/pnas.1222361110 (2013).
62. Matson, K. J. E. *et al.* A single cell atlas of spared tissue below a spinal cord injury reveals cellular mechanisms of repair. Preprint at: https://www.biorxiv.org/content/https://doi.org/10.1101/2021.1104.1128.441862v441861 (2021).
63. Kaya, T. *et al.* T cells induce interferon-responsive oligodendrocytes during white matter aging. Preprint at: https://www.biorxiv.org/content/https://doi.org/10.1101/2022.1103.1126.485917v485911.full (2022).
64. Edgar, R., Domrachev, M. & Lash, A. E. Gene expression omnibus: NCBI gene expression and hybridization array data repository. *Nucleic Acids Res.* **30**, 207–210. https://doi.org/10.1093/nar/30.1.207 (2002).
65. Ferraiuolo, L. *et al.* Dysregulation of astrocyte-motoneuron cross-talk in mutant superoxide dismutase 1-related amyotrophic lateral sclerosis. *Brain* **134**, 2627–2641. https://doi.org/10.1093/brain/awr193 (2011).
66. Sun, S. *et al.* Translational profiling identifies a cascade of damage initiated in motor neurons and spreading to glia in mutant SOD1-mediated ALS. *Proc. Natl. Acad. Sci. U. S. A.* **112**, E6993-7002. https://doi.org/10.1073/pnas.1520639112 (2015).
67. Butovsky, O. *et al.* Modulating inflammatory monocytes with a unique microRNA gene signature ameliorates murine ALS. *J. Clin. Invest.* **122**, 3063–3087. https://doi.org/10.1172/JCI62636 (2012).
68. Butovsky, O. *et al.* Targeting miR-155 restores abnormal microglia and attenuates disease in SOD1 mice. *Ann. Neurol.* **77**, 75–99. https://doi.org/10.1002/ana.24304 (2015).
69. Fukada, Y. *et al.* Gene expression analysis of the murine model of amyotrophic lateral sclerosis: Studies of the Leu126delTT mutation in SOD1. *Brain Res.* **1160**, 1–10. https://doi.org/10.1016/j.brainres.2007.05.044 (2007).
70. Yoshihara, T. *et al.* Differential expression of inflammation- and apoptosis-related genes in spinal cords of a mutant SOD1 transgenic mouse model of familial amyotrophic lateral sclerosis. *J. Neurochem.* **80**, 158–167. https://doi.org/10.1046/j.0022-3042.2001.00683.x (2002).
71. Kudo, L. C. *et al.* Integrative gene-tissue microarray-based approach for identification of human disease biomarkers: Application to amyotrophic lateral sclerosis. *Hum. Mol. Genet.* **19**, 3233–3253. https://doi.org/10.1093/hmg/ddq232 (2010).
72. Chen, H. *et al.* Differential expression and alternative splicing of genes in lumbar spinal cord of an amyotrophic lateral sclerosis mouse model. *Brain Res.* **1340**, 52–69. https://doi.org/10.1016/j.brainres.2010.03.075 (2010).
73. Wang, R., Yang, B. & Zhang, D. Activation of interferon signaling pathways in spinal cord astrocytes from an ALS mouse model. *Glia* **59**, 946–958. https://doi.org/10.1002/glia.21167 (2011).
74. D'Arrigo, A. *et al.* Transcriptional profiling in the lumbar spinal cord of a mouse model of amyotrophic lateral sclerosis: A role for wild-type superoxide dismutase 1 in sporadic disease?. *J. Mol. Neurosci.* **41**, 404–415. https://doi.org/10.1007/s12031-010-9332-2 (2010).
75. Baker, D. J. *et al.* Lysosomal and phagocytic activity is increased in astrocytes during disease progression in the SOD1 (G93A) mouse model of amyotrophic lateral sclerosis. *Front. Cell Neurosci.* **9**, 410. https://doi.org/10.3389/fncel.2015.00410 (2015).

Acknowledgements

The authors would like to thank Helena Pavlikova and Marketa Hemerova for their excellent technical assistance and Frances Zatrepalkova for proofreading the manuscript. This study was supported by grants 23-05327S and 19-02046S from the Czech Science Foundation, by the Charles University Grant Agency (Grant Number 158320), by the Institutional support RVO 86652036, by MEYS CR (CZ.1.05/1.1.00/02.0109), by the Czech Academy of Sciences (Strategy AV21, grant number VP29), by European Union's Horizon 2020 research and innovation programme under the EJP RD COFUND- EJP N° 825575 and by EU – Next generation EU, LX22NPO5107 (MEYS). Microscopy was done at the Microscopy Service Centre of the Institute of Experimental Medicine CAS supported by the MEYS CR (LM2023050 Czech-Bioimaging).

Author contributions

T.F. and Z.M. interpreted the data, wrote the manuscript and prepared all figures. T.F., Z.M., P.A., O.V., J.T., M.K. and D.K. performed experiments. T.F., Z.M., P.A., L.V., J.T,. O.V. and S.B. analyzed data. J.Z. wrote a macro for immunohistochemical analysis. M.A. and L.V. conceived and supervised the study. All authors reviewed and edited the manuscript.

Competing interests

The authors declare no competing interests.

Additional information

Supplementary Information The online version contains supplementary material available at https://doi.org/10.1038/s41598-023-33608-y.

Correspondence and requests for materials should be addressed to L.V. or M.A.

ALS-like pathology diminishes swelling of spinal astrocytes in the SOD1 animal model

Tereza Filipi[1,2], Jana Tureckova[1*], Ondrej Vanatko[1,2], Martina Chmelova[1], Monika Kubiskova[1,2], Natalia Sirotova[1,3], Stanislava Matejkova[4], Lydia Vargova[1], Miroslava Anderova[1]

[1]Department of Cellular Neurophysiology, Institute of Experimental Medicine, Czech Academy of Sciences, Prague, Czech Republic

[2]Second Faculty of Medicine, Charles University, Prague, Czech Republic

[3]Faculty of Science, Charles University, Prague, Czech Republic

[4]Analytical Laboratory, Institute of Organic Chemistry and Biochemistry, Czech Academy of Sciences, Prague, Czech Republic

*** Correspondence:**
Jana Tureckova
Jana.Tureckova@iem.cas.cz

Keywords: Amyotrophic lateral sclerosis, SOD1, astrocytes, volume regulation, extracellular space, potassium uptake

Abstract

Astrocytes are crucial for the functioning of the nervous system as they maintain the ion homeostasis via volume regulation. Pathological states, such as Amyotrophic lateral sclerosis (ALS), affect astrocytes and might even cause a loss of such functions. In this study, we examined astrocytic swelling/volume recovery in both the brain and spinal cord of the SOD1 animal model to determine the level of their impairment caused by the ALS-like pathology. Astrocyte volume changes were measured in acute brain or spinal cord slices during and after exposure to hyperkalemia. We then compared the results with alterations of extracellular space (ECS) diffusion parameters, morphological changes, expression of the Kir4.1 channel and the potassium concentration measured in the cerebrospinal fluid, to further disclose the link between potassium and astrocytes in the ALS-like pathology. Morphological analysis revealed astrogliosis in both the motor cortex and the ventral horns of the SOD1 spinal cord. The activated morphology of SOD1 spinal astrocytes was associated with the results from volume measurements, which showed decreased swelling of these cells during hyperkalemia. Furthermore, we observed lower shrinkage of ECS in the SOD1 spinal ventral horns. Immunohistochemical analysis then confirmed decreased expression of the Kir4.1 channel in the SOD1 spinal cord, which corresponded with the diminished volume regulation. Despite astrogliosis, cortical astrocytes in SOD1 mice did not show alterations in swelling nor changes in Kir4.1 expression, and we did not identify significant changes in ECS parameters. Moreover, the potassium level in the cerebrospinal fluid did not deviate from the physiological concentration. The results we obtained thus suggest that ALS-like pathology causes impaired potassium uptake associated with Kir4.1 downregulation in the spinal astrocytes, but based on our data from the cortex, the functional impairment seems to be independent of the morphological state.

1 Introduction

Amyotrophic lateral sclerosis (ALS) is a fatal disease characterized by motor neuron (MN) degeneration, resulting in muscle atrophy. The atrophy severely lowers the quality of life and culminates in early death, with a median survival of three to five years from diagnosis. There is currently no cure or prevention available, mainly because the pathological mechanisms of the disease are incompletely understood.

MNs were for a long time considered the only cell type affected by the pathology, but numerous studies have discovered that non-neuronal cells, such as glia, undergo changes and play a role in ALS progression too. Astrocytes were reported to have changed morphology and to lose neuro-supportive functions in the mutated superoxide dismutase (mSOD1) mouse – a model of ALS. The ablation of mSOD1 in astrocytes then caused significantly slower disease progression, emphasizing the active role of astrocytes in MN degeneration (Yamanaka et al., 2008).

Changes in astrocyte gene expression have been described in the context of ALS, and several mechanisms have been proposed for the presumed astrocytic contribution to MN death. They include glutamate excitotoxicity and ionic imbalance due to impaired astrocytic clearance. Physiologically, maintaining ion homeostasis is one of the most important functions of astrocytes in the CNS. They sustain the K^+ concentration in the extracellular space (ECS) on a physiological level (around 3 mmol/l) (Larsen et al., 2016) employing both ion channels (primarily inwardly rectifying K^+ channels; Kir) pumps and transporters (Na^+ /K^+-ATPase; NKA and Na^+/K^+/2Cl^- cotransporter; NKCC), which are necessary to prevent neuronal hyperexcitability. During the various pathological conditions, excessive release of K^+ from neurons occurs, and due to energy deprivation and failure of astrocytic NKA, its concentration can reach up to 50-60 mM in case of ischemia or traumatic injury (van Putten et al., 2021). Disruption of K^+ homeostasis results in increased activity of potassium channels and activation of NKCC1, which drives the import of Na^+, K^+ and Cl^-, and results in extensive swelling of astrocytes and shrinkage of the CNS ECS (Hellas and Andrew, 2021, Kahle et al., 2015, Song and Yu, 2014). This can cause additional ion imbalance, affect neuronal excitability and synaptic transmission, and disrupt the movement of molecules and ions critical for nutrition delivery and signaling. That in turn leads to increased tissue density, cellular stress responses including inflammation and oxidative stress, and eventually results in cell damage or death (Amlerova et al., 2024, Nedergaard and Verkhratsky, 2012). Changes in ECS volume can be characterized by ECS diffusion parameters, extracellular volume fraction α and tortuosity λ, which reflect the contemporary structure of the brain and govern the extracellular diffusion of neuroactive substances (Thorne and Nicholson, 2006, Nicholson and Hrabetova, 2017).

Considering the importance of ion homeostasis for proper CNS operation, we aimed to explore the astrocytic homeostatic functions in ALS. For the purpose of our study, we generated a mouse with an ALS-like phenotype, SOD1(G93A) mutation, and fluorescently labeled astrocytes, on the FVB/N background. Since the SOD1 model on the FVB/N background has not been thoroughly characterized yet and only recently became commercially available, we decided to examine astrocytes in both the brain and spinal cord in terms of their homeostatic functions and morphological changes, to fill the knowledge gap. In addition to elucidating the altered functional properties of astrocytes in ALS progression, our data can also serve as a stepping-stone for others working with the SOD1 model on FVB/N background.

2 Materials and Methods

2.1 Animals

For all experiments, we used a transgenic mouse on FVB/N background with fluorescently labeled astrocytes, expressing human SOD1(G93A). As a control, we used their non-carrier littermates. To generate the mouse, we crossbred C57Bl/6J-Tg (SOD1*G93A)1Gur/J (JAX Strain: 004435) males with GFAP/EGFP (Nolte et al., 2001) females. The visualization of astrocytes in GFAP/EGFP mice is feasible due to the expression of enhanced green fluorescent protein (EGFP) under the control of the human glial fibrillary acidic protein (GFAP) promoter. To obtain the congenic strain, mice were backcrossed to FVB/N background for at least 10 generations. These mice are further termed as SOD1/GFAP/EGFP and CTRL/GFAP/EGFP. In behavioral testing, we also employed the transgenic mice overexpressing human SOD1(G93A) (JAX Strain: 004435 C57BL/6 J-Tg (SOD1*G93A)1Gur/J) and their non-carrier littermates (Gurney et al., 1994). For these mice, we used the abbreviation SOD1/C57Bl6 and CTRL/C57Bl6 respectively.

All procedures involving the use of laboratory animals were performed following the European Communities Council Directive 24 November 1986 (86/609/EEC) and animal care guidelines approved by the Institute of Experimental Medicine, Academy of Sciences of the Czech Republic (Animal Care Committee in April 2019; approval number 40/2019). All efforts were made to minimize both the suffering and the number of mice used.

2.2 Behavioral testing

We conducted the wire grid hang test and the rota-rod test (Mouse RotaRod NG 47650, Ugo Basile, Italy) to assess muscle strength, function, and coordination throughout the disease. Weight was also measured as an additional parameter of the symptom progression. Testing consisted of a single three-attempt session every week, beginning at P30, and lasting for 14 weeks. Before the experiment, all mice were trained.. Data are presented as mean or mean ± standard error of the mean (SEM) for n mice. Repeated measures of two-way ANOVA with Holm-Sidak's multiple comparison correction were used to analyze the differences between groups.

2.2.1 Wire Grid hang test

Each mouse was placed on a custom-made wire lid, approximately 60 cm above a wood chip covered bottom, and turned upside down. The latency to fall was measured. At the beginning of the testing period, we trained each mouse three consecutive times for at least 180 seconds. In the experimental session, the mouse had three attempts to hold on to the lid. We noted the best score out of the three with a maximum of 180 seconds.

2.2.2 Rotarod test

The mouse was placed on a stationary rod facing against the direction of rotation. The rod started rotating at a constant speed of 15 rpm, and the latency to fall was measured. Each mouse was trained three consecutive times of at least 180 seconds at 5, 10 and 15 rpm speed. In the experimental session, the mouse had three attempts to remain on the rod. We noted the best score out of the three with a maximum of 180 seconds.

2.3 Immunohistochemistry and image analysis

To obtain tissue for immunohistochemical analyses, the mice were deeply anesthetized with pentobarbital (PTB) (100 mg/kg, i.p.) and perfused transcardially with 20 ml of saline solution followed by 20 ml of cooled 4% paraformaldehyde (PFA) in 0.1 M phosphate buffer. The brains and spinal cords were then postfixed overnight with PFA and treated with a sucrose gradient (ranging from 10 % to 30 %) for cryoprotection. Coronal 30-µm-thick slices were prepared using a cryostat (Leica CM1850, Leica Microsystems, Wetzlar, Germany). For immunohistochemical staining, the slices were washed in a phosphate buffer saline followed by blocking of the nonspecific binding sites with 5%

Chemiblocker (Millipore, Billerica, MA), and 0.2% Triton in phosphate buffer saline. The blocking solution was also used as the diluent for the antisera. The slices were incubated with the primary antibodies overnight, and the secondary antibodies were applied for 2 hours at 4–8 °C. The following antibodies were used: anti-Kir4.1 (dilution 1:300; Alomone Labs, Jerusalem, IL; catalog number: APC-035-GP), goat anti-Guinea Pig IgG conjugated with Cy3 (dilution 1:200; Chemicon, Temecula, CA, US; catalog number: AP108C). Cell nuclei were visualized by DAPI staining (Merck, Darmstadt, Germany). Following staining, the slices were mounted, and the fluorescence signal was imaged and scanned using a spinning disc microscope (Olympus, SpinSR10) equipped with dry UPLXAPO 40× objective.

The areas corresponding to cells with endogenous EGFP expression under GFAP promoter were quantified using FIJI image processing software (ImageJ 2.9.0/1.53t) (Schindelin et al., 2012). Segmentation was performed by thresholding the EGFP channel and the fluorescence-positive area was measured and related to the area of primary and secondary motor and primary somatosensory cortex or spinal ventral horn area. The area corresponding to EGFP reflects both the increased number of GFAP-expressing cells and the enlargement of astrocytic soma and the thickening of their processes. A similar thresholding approach for segmentation was also used for the Kir4.1 antibody signal. The immunopositive regions were segmented using the threshold dialog and the mean gray values were calculated in the segmented area. The statistical analysis of the differences among groups was performed using unpaired t-test. Error bars in plots represent SEM.

2.4 Preparation of acute brain and spinal cord slices for functional measurements

Experiments were performed on acute brain and spinal cord slices of SOD1/GFAP/EGFP and CTRL/GFAP/EGFP mice at the age of 4 months. The mice were deeply anesthetized with PTB (100 mg/kg, i.p.), and perfused transcardially with a cold (4–8°C) isolation buffer. Brains and spinal cords were dissected and placed into a cold isolation buffer (4–8 °C), oxygenated with 95% O2 and 5% CO2 (Carbogen, Siad, Branany, Czech Republic). The spinal cord was then embedded into the low-melting agarose (Sigma-Aldrich). Brain and spinal cord coronal slices (300 μm for 3D-morphometry and 400 μm for the TMA method) were cut using an HM650 V vibratome (MICROM International GmbH, Waldorf, Germany). The slices were then incubated for 40 minutes at 34 °C in the isolation solution. After the incubation period, the slices were kept at room temperature (23–25 °C) in artificial cerebrospinal fluid (aCSF).

2.5 Experimental solutions for functional measurements

The compositions of all experimental solutions are listed in Table 1. All solutions were equilibrated with 95% O2 and 5% CO2 (Carbogen, Siad, Branany, Czech Republic) to a final pH of 7.4, while the osmolality was measured using a vapor pressure osmometer (Vapro 5520, Wescor, Logan, USA).

2.6 Three-dimensional confocal morphometry

Time-dependent changes in astrocyte volume and morphology were studied using 3D-confocal morphometry in the motor cortex and in the ventral horns of the spinal cord. The method was previously described in Awadova et al. (2018), Pivonkova et al. (2018). Briefly, brain or spinal cord slices were carefully placed into the recording chamber and mounted on the stage of a confocal microscope. The slices were held down with a U-shaped platinum wire with a grid of nylon threads. The recording chamber was continuously perfused with recording solutions (aCSF or aCSF_{K^+}) via peristaltic pump PCD 31.2 (Kouril, Kyjov, Czech Republic) at a rate of ~7.5 mL/min. The exchange of solutions in the recording chamber took place within 2 minutes. All measurements were performed at room temperature. Fluorescence images were acquired on a multiphoton laser scanning microscope FV1200MPE (Olympus) with 60× LUMPLFLN water objective (NA = 1.0, WD 2 mm). EGFP fluorescence was excited in a 2-photon absorption mode at 950 nm by a tunable Ti-Sapphire laser system MaiTai DeepSee (Spectra Physics, CA). A fluorescence signal selected by 495 – 540-nm band-pass emission filter was detected by GaAsP detector. Cortical astrocytes (layers II – V of the motor cortex) and astrocytes in the anterior horns of the spinal cord were imaged in a z-stack with a uniform spacing of 0.5 µm and a resolution of 512 × 512 pixels with the voxel size 0.41 × 0.41 × 0.5 µm.

The signal acquisition was set so that the cell body did not contain oversaturated pixels. The imaging was done as follows: three full 3D stacks of images were acquired in the isotonic aCSF solution to assess the rate of image acquisition-induced photobleaching by linear correction. During the cell volume changes induced by $aCSF_{K+}$ 20 mM or 50 mM treatment, individual 3D images were acquired in 5-minute intervals, 4 times in total. Finally, the cell volume recovery was checked following the re-application of isotonic aCSF solution (washout) after 20 and 40 minutes.

Measurements of fluorescence intensity (FI) and soma size (Ss) were performed in Fiji image processing software (ImageJ 2.9.0/1.53t) (https://fiji.sc) (Schindelin et al., 2012). Variations of FI due to cell volume changes were monitored as follows: x-y-z image stacks acquired in each individual time point were reduced to 2D frames by an average intensity projection along the z-axis. These reduced images were composed to a time stack and aligned with StackReg (ImageJ plugin by Philippe Thévenaz, Biomedical Imaging Group, Swiss Federal Institute of Technology, Lausanne). Integral fluorescence intensities within a circular ROI of ~2 µm in diameter located within the cell soma were measured. Average intensity projections of the recorded 3D stacks were segmented by an automatic threshold based on the Isodata Algorithm (Ridler and Calvard, 1978). The cell area in the frame containing the segmented cell body was treated as the 2D measure of the Ss. Soma volume (Vs) is then proportional to $\sqrt{Ss3}$, assuming isotropic volume changes. For each CNS part (brain or spinal cord) at least 3 mice were used, with a minimum of 2 slices per mouse. Changes in the total astrocyte volume are presented as the mean ± SEM. Statistical significance was determined using two-way ANOVA. Differences between the groups were considered statistically significant when $p < 0.05$ (*), very significant when $p < 0.01$ (**), and extremely significant when $p < 0.001$ (***).

2.7 TMA method

The slices were placed into the experimental chamber connected with upright Zeiss Axioscope microscope (Zeiss, Germany) and manipulators (Luigs and Neumann, Germany). Measurements were performed at room temperature (22–24°C) at a depth of 200 µm, during a continuous perfusion with aCSF solution enriched with 0.1 mM tetramethylammonium ion (TMA^+) and saturated with carbogen. Recordings were carried out every 5 minutes.

The ECS diffusion parameters, volume fraction α (α = ECS volume/total tissue volume), tortuosity λ (λ^2 = free diffusion coefficient/apparent diffusion coefficient) and nonspecific uptake (k' [s^{-1}]), were measured in acute brain and spinal cord slices using the real-time iontophoretic method (RTI) as described in detail in Nicholson and Phillips (1981) and (Sykova and Nicholson, 2008). In brief, the extracellular marker TMA^+ (molecular weight 74.1 Da) was introduced into the tissue through an iontophoretic micropipette. The TMA^+ imitated the diffusion of small ions and molecules in the ECS, and its time-dependent changes in the extracellular concentration were measured by double-barreled ion-selective microelectrodes (ISM). The manufacturing of double-barreled TMA^+- ISMs was described in detail previously (Syková, 1992). Briefly, the reference barrel was filled with 150 mM NaCl and an ion-sensitive barrel contained an ion exchanger IE190 (WPI, Inc., Sarasota, USA, RRID:

SCR_008593) at the tip, and 100 mM TMA^+ solution as a backfilling solution. Prior to each experiment, the TMA^+-ISMs were calibrated in a series of five different solutions with increasing TMA^+ concentrations: 0.1, 0.3, 1.0, 3.0 and 10.0 in a background of 3 mM KCl and 150 mM NaCl. The TMA^+ signals were fitted to the Nikolski equation to acquire the slope and interference of each ISM (Nicholson, 1993). The iontophoretic micropipettes backfilled with 100 mM TMA chloride were glued to individual ISMs with a tip separation of 50-100 µm. Prior to the experimental measurements, the ISMs arrays were calibrated in 0.3% agar gel (Merck, Germany). The 20 nA bias current was continuously applied (Single Channel Iontophoresis Generator ION-100; Dagan Corporation, Minneapolis, Minnesota, USA) to maintain a constant electrode transport number. A current step of 200 nA and 24s duration (stimulator master 8, A.M.P.I, Jerusalem, Israel) generated a diffusion curve. The obtained diffusion curves were analyzed by a non-linear curve fitting simplex algorithm, operating on a modified diffusion equation using the VOLTORO program (kindly provided by C. Nicholson, New York University School of Medicine, USA, unpublished data) to acquire the values of the electrode transport number (n) and the free diffusion coefficient of TMA^+ (D). Knowing the n and D values, the parameters α, λ and k' could be determined from the measured tissue. The measurements were performed at room temperature (22-24°C) in aCSF, and the obtained values were averaged. Diffusion measurements were performed in the brain cortex and the anterior horn of the lumbar part of the spinal cord at a depth of 200 µm. The stable control values were acquired in the aCSF, followed by a 20 minute application of increased potassium concentrations (20mM or 50mM $aCSF_{K+}$) and by a 40 minute wash-out in aCSF. The diffusion curves were captured and analyzed every 5 minutes.

Data are expressed as mean ± SEM, where n represents the number of slices/measurements. Statistical analyses were performed using Graph Pad statistical package (https://www.graphpad.com) - between experimental groups using two-way ANOVA analysis, followed by Sidak's multiple comparison test and one-way ANOVA with Dunnet's multiple comparison test to analyze changes within a single group (CTRL and SOD1 separately). Differences between the groups were considered statistically significant when $p < 0.05$ (*), very significant when $p < 0.01$ (**), and extremely significant when $p < 0.001$ (***).

2.8 Elemental analysis of CSF

2.8.1 CSF isolation

The experiment was performed using SOD1/GFAP/EGFP and CTRL/GFAP/EGFP mice at the age of 4 months. To isolate the cerebrospinal fluid, we used modified protocol from (Kaur et al., 2023). Briefly, we used borosilicate glass capillaries (Sutter Instruments, Novato, CA, United States) and P-97 Brown-Flaming puller (Sutter Instruments, Novato, CA, United States) and prepared the capillary, using pulling settings as specified in the protocol. The mice were initially anesthetized with 3% isoflurane (Abbot, IL, United States) and maintained at 1-2% isoflurane using a vaporizer (Tec-3, Cyprane Ltd., Keighley, United Kingdom). We omitted the use of a stereotactic instrument but followed the protocol with cisterna magna exposure and then the CSF extraction. We looked for any traces of blood contamination and used only clear samples for further analysis (see Fig. 7). The average amount of isolated CSF per mouse was 15 µl. The body temperature of the mouse was maintained at 37 ± 1°C using a heating pad throughout the procedure and the mouse was sacrificed immediately after.

2.8.2 Elemental analysis

The ion concentration in the cerebrospinal fluid was determined using inductively coupled plasma optical emission spectroscopy (ICP-OES) coupled with an electrothermal evaporation (ETV) unit. ICP-OES is a widely used highly sensitive analytical method capable of determining most elements. In brief, a sample in the form of a solution is converted to a fine aerosol, which is then carried by a stream of argon into a high-temperature argon plasma, where evaporation, atomization, and excitation take place. The characteristic radiation emitted by the excited atoms is then processed in the spectrometer. The ETV is an alternative sample introduction system, which allows direct analysis of solid or liquid samples. The sample was weighed in a graphite boat and heated in a graphite furnace using an optimized temperature program in an argon atmosphere, with the maximum achievable temperature of 3000 °C. The addition of a small amount of CCl_2F_2 into the furnace facilitates the conversion of analytes to more volatile forms, thus ensuring complete analyte evaporation. The generated dry aerosol is carried by argon stream directly into the plasma. This approach offers lower detection limits and matrix-independent calibration, thus allowing the analysis of smaller sample amounts, thanks to nearly loss-free transport of sample directly into the plasma. For analysis, 10 µl of cerebrospinal fluid was pipetted into a graphite boat and the sample amount was checked by weighing it. Due to low sample volumes, only one replica per sample was possible. An Arcos I (Spectro, Kleve, Germany) ICP-OES instrument coupled to an ETV 4000c unit (Spectral Systems, Fürstenfeldbruck, Germany) was used for the analysis.

3 Results

3.1 Behavioral testing revealed phenotypical differences between C57Bl/6 and FVB/N mSOD1 mice

To confirm the phenotype of our animal model created by crossbreeding of C57Bl6 SOD1(G93A) and GFAP/EGFP mice (Nolte et al., 2001), we conducted the hanging wire motor test (Fig. 1a) and Rotarod test (Fig. 1b). We tested a comparable number of mice for all four groups: SOD1/C57Bl6; CTRL/C57Bl6; SOD1/GFAP/EGFP and CTRL/GFAP/EGFP with an equal distribution of males and females within each group.

First, we compared SOD1/GFAP/EGFP (n = 34) and CTRL/GFAP/EGFP (n = 36) mice (Fig. 1c, d). Based on the results, we can confirm that our crossbred mice manifest typical ALS symptoms such as loss of strength in both forelimbs and hind limbs and poor motor coordination (Gurney et al., 1994). Mutants compared to controls performed significantly worse in both tests from two months of age, which is generally considered an onset point for the SOD1(G93A) model (Mead et al., 2011, Gerber et al., 2012, Mancuso et al., 2011). The hanging wire test showed continuous strength decline, with the mice being almost unable to hold themselves on the grid at the end stage, which suggests severe strength loss, mainly in the hind limbs (Fig. 1c). The Rotarod measurements showed significantly impaired motor coordination in mutant mice starting around three months of age (Fig. 1d). Our results are in agreement with the data from SOD1(G93A) mice from the standpoint of the onset. Nevertheless, we decided to compare the overall performance of the two strains as well, to see whether the different backgrounds have any effect on the phenotype.

Interestingly, we discovered significant differences between the SOD1/GFAP/EGFP and SOD1/C57Bl6 mice performance during the symptomatic stage (Fig. 1e, f). The strength in both forelimbs and hind limbs was comparable until the onset, but then the gross phenotype of SOD1/GFAP/EGFP mice worsened much faster and their performance at three months of age was comparable to that observed in the final stage (four months of age) of SOD1/C57Bl6 and continued to decline (Fig. 1e). The motor coordination tested by Rotarod also seemed to be more impaired in SOD1/GFAP/EGFP mice. Again, their performance at three months of age was comparable to the final stage (four months of age) of SOD1/C57Bl6 (Fig. 1f).

Overall, the onset point remains similar for both strains; however, the course of the disease seems to differ between the SOD1/GFAP/EGFP and SOD1/C57Bl6 mice. The SOD1/GFAP/EGFP mice decline faster and they reach the "final stage" values of the original model about a month earlier. Our data thus suggest that a different genetic background does not affect the onset of the disease manifestation but rather affects the rate of disease progression or worsening of the overall symptoms.

3.2 Fluorescence analysis confirmed astrogliosis

To define the state of astrocytes in the SOD1/GFAP/EGFP model, we took advantage of their eGFP-labeling and performed a fluorescence analysis looking for the signs of astrogliosis in both the brain and spinal cord. Astrogliosis is marked by cellular hypertrophy, shortened cell processes and increased GFAP expression, and was described in the spinal cord of the original SOD1(G93A) model on the C57BL6 background (Miller et al., 2017, Guttenplan et al., 2020). The regions of interest for fluorescence analysis were the motor- the somatosensory cortex, and the ventral horn of the lumbar spinal cord. To ensure we analyzed the whole area of interest, we took advantage of the tile scanning technique (see Fig. 2a, c). 120 ± 3 days old mice were used for the analysis.

Our results in the motor and somatosensory cortex (Fig. 2b) revealed a significantly larger fluorescent area in the SOD1 mice, and we observed the same situation in the ventral horns of the lumbar spinal cord (Fig. 2d). This suggests a higher GFAP positivity (thus a visible change in morphology and/or increase of GFAP-positive cells) caused by ALS-like pathology. These results confirm that astrocytes become activated in both the brain and spinal cord during the disease progression in the model on the FVB/N background. This is consistent with the results from the SOD1/C57Bl6 original model, in which astrocytic activation is considered one of the disease hallmarks.

3.3 Spinal SOD1/GFAP/EGFP astrocytes exhibit disrupted volume regulation during higher potassium concentrations

The analysis of EGFP fluorescence revealed morphological changes in both cortical and spinal astrocytes suggesting their shift toward an activated state. We were interested to see whether this shift has affected astrocytic ability to swell, which is connected to potassium uptake that contributes to maintaining potassium homeostasis. Potassium levels tend to be higher during pathological stages, so we conducted an experiment measuring astrocytic volume during exposure to different potassium concentrations. We used 20 mM and 50 mM $aCSF_{K+}$ solutions to evoke elevated potassium levels occurring e.g. during closed brain injury and ischemia, respectively (Rossi et al., 2007, Muller and Somjen, 2000, Pietrobon and Moskowitz, 2014). The measurements were conducted using acute brain and spinal cord slices from SOD1/GFAP/EGFP and CTRL/GFAP/EGFP mice exposed to either 20mM or 50mM $aCSF_{K+}$ for 20 minutes followed by a 40-minute application of aCSF (further termed as washout). Changes in astrocytic volume were recorded every 5 minutes during the application and every 20 minutes during the washout (see Fig. 3a). Astrocyte volume at t = 0 was set to 100 % and the swelling was expressed relative to this baseline as an increase in percentage. 120 ± 3 days old mice were used for the analysis.

Volume changes of cortical astrocytes were measured specifically in the motor and the somatosensory cortex of acute brain slices. Surprisingly, the measurements and following data analysis revealed that SOD1 cortical astrocytes can handle higher potassium levels with the same efficacy as healthy astrocytes during both 20 and 50mM K^+ application (Fig. 3b, c) despite the observed astrogliosis. After initial measurements cells swelled up to ~190 % and almost ~340 % respectively. All cells were able to recover their volume in the following 40 minutes, suggesting there is no impairment in potassium level maintenance.

Spinal astrocytes were measured specifically in the ventral horns of the spinal cord. The results of our measurements show that the SOD1 spinal astrocytes have unimpaired swelling capacity in the 20 mM K^+ environment (Fig. 3d) asthey swell comparable to healthy cells. The higher potassium concentration; however, represents a challenge. The SOD1 astrocytes swelled significantly less in the 50 mM K^+ than the CTRL astrocytes throughout the whole application (Fig. 3e). While the SOD1 astrocytes swelled up to only ~ 275 %, the CTRL astrocytes swelled to ~400 % of their original volume. The difference in swelling in the high potassium environment suggests inefficient uptake of the extracellular potassium, which could result in potassium homeostasis imbalance in the SOD1 spinal cord. Despite the extensive swelling, both SOD1 and CTRL astrocytes were able to recover their volume during the washout, even though in the CTRL cells this was only partially.

3.4 A higher potassium concentration alters the extracellular space diffusion parameters in the SOD1/GFAP/EGFP spinal cord

To investigate alterations in the dynamics of the ECS diffusion properties, we used the RTI method and measured the brain and spinal cord of 120 ± 3 day old mice. We hypothesized that the alterations detected in SOD1/GFAP/EGFP mice astrocyte morphology and their functional properties analyzed by 3D-morphometry could be manifested as variations in the ECS parameter values. To address this, we employed the same experimental protocol as outlined earlier. Briefly, brain and spinal cord slices from SOD1/GFAP/EGFP and CTRL/GFAP/EGFP were exposed to two distinct $aCSF_{K+}$ concentrations (20mM and 50mM) separately, for 20 minutes, followed by a 40-minute washout period with aCSF. The alterations in ECS parameters from the initial values determined before the application were monitored at 5-minute intervals throughout both the application phase (20 minutes) and the subsequent washout period (40 minutes). The quantification of the ECS parameters volume fraction (α) and tortuosity (λ) was done in the cerebral milieu of the motor cortex and the ventral horns of the spinal cord.

The initial values in the cortex of CTRL mice ($\alpha = 0.189 \pm 0.006$, $\lambda = 1.59 \pm 0.05$, n = 16, expressed as mean ± SEM) did not significantly differ from those acquired in SOD1 mice ($\alpha = 0.195 \pm 0.006$, $\lambda = 1.64 \pm 0.04$, n = 18). Application of 20mM $aCSF_{K+}$ (Fig. 4a, b) for 20 minutes induced cell swelling in both experimental groups, leading to a shrinkage of the ECS volume, manifested as a compensatory decrease of the ECS volume fraction (α: CTRL 0.122 ± 0.006, SOD1 0.128 ± 0.005, $p < 0.0001$), while no significant changes in tortuosity were detected (λ: CTRL 1.605 ± 0.03, SOD1 1.677 ± 0.03). During the 40 min washout, the ECS volume fraction fully recovered to initial values in both CTRL and SOD1 mice or even exceeded them, however, no significant differences between groups were found.

The exposure of brain slices to 50mM $aCSF_{K+}$ (Fig. 4c, d) revealed a statistically significant decrease in the volume fraction in both groups ($p < 0.001$) compared to the initial values, with no significant difference observed between CTRL ($\alpha = 0.072 \pm 0.01$, n = 9) and SOD1 mice ($\alpha = 0.095 \pm 0.02$, n = 9). Tortuosity was not significantly affected by the 50mM $aCSF_{K+}$ application, either in CTRL or SOD1 mice; the maximum values reached in the 20th min of application did not differ between CTRL and SOD1 mice either (λ: 1.73 ± 0.05 and 1.75 ± 0.05, respectively). The subsequent washout procedure demonstrated a complete recovery of the volume fraction towards the end of the experiment in both groups.

The analysis of values obtained prior to the application in the spinal cord showed that there were no differences in the initial values of the ECS volume fraction or tortuosity between the groups of mice (CTRL: $\alpha = 0.193 \pm 0.007$, $\lambda = 1.68 \pm 0.05$; SOD1: $\alpha = 0.196 \pm 0.003$, $\lambda = 1.75 \pm 0.07$). Following exposure of the spinal cord tissue to 20mM $aCSF_{K+}$, the volume fraction decreased from the initial values in both experimental groups (CTRL: $\alpha = 0.164 \pm 0.003$, n = 8, SOD1: $\alpha = 0.151 \pm 0.008$; $p < 0.001$, n = 9); the maximum decrease reached in the 20th min did not differ between the groups (Fig. 5a, b). No changes from the initial values were detected in tortuosity (CTRL: $\lambda = 1.76 \pm 0.04$; SOD1: $\lambda = 1.81 \pm 0.02$). The washout resulted in full recovery of the ECS volume in both groups: CTRL ($\alpha = 0.195 \pm 0.004$) and SOD1 ($\alpha = 0.196 \pm 0.009$) after 40 min of aCSF application.

Exposure of the spinal cord slices to 50mM $\text{aCSF}_{\text{K+}}$ resulted in a more profound decrease in the ECS volume fraction in CTRL (n = 6) compared to SOD1 (n = 6) mice ($\alpha = 0.130 \pm 0.01$ and 0.171 ± 0.008, respectively). Moreover, this decrease was faster in CTRL mice ($p < 0.0001$ already in 10th min) than in SOD1 group ($p = 0.03$ in 20th min) (Fig. 5c). Full recovery of ECS volume fraction was detected in CTRL mice ($\alpha = 0.189 \pm 0.005$), while the values at the end of the washout in SOD1 mice exceeded the initial values, indicating that the ECS volume after washout was larger than before application ($\alpha = 0.226 \pm 0.011$, $p = 0.0006$). To further analyze the inter-group differences in the ECS volume changes during the washout period, the α values during washout were expressed as a percentage of volume increase/decrease in relation to the value of α reached in the 20th min of application, which was set as 100%. At the end of the washout (40th min), the ECS volume reached 123 ± 10 % of its initial value in CTRL mice and 259 ± 82 % in SOD1 mice. However, this analysis did not show any significant differences between CTRL and SOD1 mice, most likely due to the huge variability in the recovery rate in individual experiments. Interestingly, perfusion with 50mM $\text{aCSF}_{\text{K+}}$ evoked a steep increase in tortuosity values in CTRL mice ($p < 0.0005$), while tortuosity in SOD1 mice remained unchanged (Fig. 5d).

3.5 Downregulation of potassium channel Kir4.1 was confirmed by immunohistochemical analysis

Due to the observed differences in astrocyte swelling during higher potassium concentrations, we were interested whether this could be associated with the expression of Kir4.1 (Fig. 6a), as these channels undergo downregulation in numerous CNS pathologies (Wilcock et al., 2009, Harada et al., 2013, Hanani and Spray, 2020). Kir4.1, predominantly expressed in astrocytes, is a subtype of Kir channels, which are crucial for maintaining the resting membrane potential and regulating K^+ homeostasis in cells. To assess the expression, we employed immunohistochemistry followed by fluorescence analysis. We looked at the protein expression in the motor and the somatosensory cortex as well as in the spinal ventral horns of 120 ± 3 day old SOD1/GFAP/EGFP and CTRL/GFAP/EGFP mice. Our results suggest that there is no significant difference between Kir4.1 expression in the cortex, as the values we obtained were almost equal in both SOD1 and CTRL mice (Fig. 6b). However, the fluorescence analysis in the ventral horns of the spinal cord showed significant downregulation of the Kir4.1 channel (Fig. 6c). This downregulation could be associated with the lower swelling observed in spinal SOD1 astrocytes during the 50 mM $\text{aCSF}_{\text{K+}}$ application.

3.6 Elemental analysis revealed low magnesium concentration in the cerebrospinal fluid of mutated mice

The data from functional measurements and immunohistochemical analysis suggested that the SOD1/GFAP/EGFP mice could suffer from potassium imbalance. Higher potassium levels are generally associated with pathological stages, however, to the best of our knowledge, the actual potassium concentration in the cerebrospinal fluid of SOD1/C57Bl6 or the SOD1/GFAP/EGFP mouse model is not known. We thus decided to use the elemental analysis and determine the concentration of extracellular potassium and other elements in the cerebrospinal fluid (CSF) of the 120 ± 3 day old SOD1/GFAP/EGFP mice experiencing stiffness and loss of ability to move their hind limbs together with ~20% weight loss as is typical for the final stage of the disease. We employed electrothermal vaporization (ETV) coupled with inductively coupled plasma optical emission spectrometry (ICP-OES) and measured samples of CSF collected from both CTRL and SOD1 mice. The CSF was isolated using protocol adapted from (Kaur et al., 2023), and only clear samples without any sign of blood (Fig. 7a) were processed and analyzed. In addition to potassium, we also analyzed Ca, Fe, Mg, Na, P and S (Table 2). The potassium concentration in the CSF from SOD1 mice was comparable to the concentration in CTRLs (Fig. 7b) and both were within the range of the physiological concentration, which can slightly vary depending on factors such as age or experimental condition, but is typically ~3 mmol/l (Larsen et al., 2016). Interestingly, we detected a significantly lower concentration of magnesium in the CSF of SOD1 mice (Fig. 7c). Magnesium is among other things involved in muscle function and neuronal signaling, and a lower magnesium concentration has been reported in post mortem analysis of ALS patients as well (Yasui et al., 1997). Concentrations of other tested elements did not differ between the controls and mutated mice.

4 Discussion

ALS is a fatal neurological disease with rapid progression and no effective treatment strategies. Even though it is primarily viewed as a motor-neuron disease, glial cells actively contribute to the onset/progression, and therefore represent promising targets for therapeutic approaches in the future. Astrocytes are considered especially promising, due to their crucial role in maintaining neural function and sustaining homeostasis of ions and transmitters. Nevertheless, it is necessary to understand the complex processes that are affected by the ALS pathology first, in order to identify optimal therapeutic strategies.

In this study, we detailed a mouse strain, created by crossbreeding the GFAP/EGFP (Nolte et al., 2001) with the SOD1(G93A) model of ALS (Gurney et al., 1994), resulting in mice with ALS-like phenotype and fluorescently labeled astrocytes. The original SOD1(G93A) model is based on a C57Bl6 background, while the GFAP/EGFP mice have FVB/N background. By extensive breeding we obtained a SOD1 mouse on FVB/N background (see Methods). This mouse just recently became commercially available for experimental use (jax.org/strain/013199), however, without the labeled astrocytes. Behavioral testing of our mice revealed significant differences between disease progression of the original model and the one with the FVB/N background. The researchers providing this model to the Jackson Laboratory also highlighted this. It is very likely the different genetic background causing the discrepancies; however, the exact mechanisms through which it affects the disease progression are unclear. Previous studies on this topic revealed that various ALS models have phenotype variations affecting the progression. It can be, for instance, a variation in microglia–mediated neuroinflammation (Heiman-Patterson et al., 2011, Nikodemova and Watters, 2011) and/or the hyperactivity of metabolic processes. Jackson laboratories in particular report hyperactivity of metabolism in terms of increased oxygen consumption, abnormal energy expenditure or decreased circulating insulin levels for the B6SJL background (jax.org/strain/002726). The different backgrounds affected the performance on both the hanging wire grid and Rotarod, but especially the motor coordination tested by Rotarod seemed to be much more affected in the SOD1/GFAP/EGFP model than in the SOD1/C57Bl6. Based on the gross phenotype, the progression is more rapid, nevertheless the mice still exhibit the distinctive features typical for ALS and represent thus another valid model for ALS research.

Our data from the fluorescence analysis of astrocytes confirmed the ALS-like pathology, also on the cellular level. We identified astrogliosis in both the ventral horns of the spinal cord and in the motor and somatosensory cortex, which confirms that astrocytes become activated during ALS, change their morphology, and may alter their functions. The astrocytic activation was observed in the spinal cord of the original SOD1/C57Bl6 model (Nagai et al., 2007, Baker et al., 2015), however, cortical astrocytes are a subject of debate. Some studies confirmed their activation in the motor cortex of SOD1 mice (Miller et al., 2018, Gomes et al., 2019, Gomes et al., 2020), but others (Filipi et al., 2023, Niessen et al., 2006) did not report any pathological changes, suggesting the pathology may be limited to the spinal and bulbar motor neurons in this particular model. To the best of our knowledge, no studies have assessed the astrocytic activation in the SOD1 model on FVB/N background yet, and we thus cannot compare our findings. Nevertheless, it is likely that with the faster progression rate of the gross phenotype, the cellular phenotype could also worsen/be easier to detect in comparison with the original SOD1/C57Bl6.

Besides morphology, astrocytes significantly change their gene profile in ALS (Baker et al., 2015, Miller et al., 2018, Ferraiuolo et al., 2011), especially in association with alterations of their two essential functions - glutamate uptake and potassium clearance.. To broaden the knowledge of the latter, we took advantage of fluorescently labeled astrocytes and measured their swelling, reflecting their ability of K^+ uptake and changes in the extracellular space during exposure to high K^+ concentrations. K^+ physiological concentration in the nervous system is ~3 mM and rises during pathological conditions such as ischemic stroke, traumatic brain injury, and epileptic seizures (Ohno et al., 2021). It happens primarily due to cellular damage, ion pump dysfunctions, excitotoxicity, or even blood-brain barrier dysfunction (Janigro, 2012, Keep et al., 1999, Lapilover et al., 2012, David et al., 2009, Larsen et al., 2016). The disruption of potassium homeostasis can affect neuronal activity and lead to further damage and dysfunction if not properly regulated.

Altered astrocytic ability of maintaining K^+ homeostasis has been previously proposed in neurodegenerative disorders such as Huntington disease and Alzheimer’s disease as well as in ALS (Ding et al., 2024, Khakh et al., 2017, Ohno et al., 2021). Ding et al. (2024), Stevenson et al. (2023) recently observed a reduced K^+ clearance rate in the motor cortex of the SOD1/C57Bl6 mouse model, and those changes correlated with motor neuron loss (Ding et al., 2024). Our data however, showed a comparable degree of swelling in both CTRL and SOD1 cortical astrocytes, suggesting that the K^+ uptake remains unimpaired in the cortex of the SOD1/GFAP/EGFP mice. The uptake is however, only one of the complex clearance mechanisms maintaining the K^+ homeostasis. A possible interpretation for the divergence in our data has been proposed by Stevenson et al. (2023), who explain the reduced clearance by reduced coupling of astrocytes that prevent spatial buffering rather than by a direct change in potassium channel expression, hence the K^+ uptake itself. The SOD1 spinal astrocytes, on the other hand, swelled significantly less than CTRL astrocytes during the highly elevated (50 mM) potassium concentration and volume recovery was appropriately faster. This suggests that swelling in our case reflects a change in the uptake mechanism, not a mechanism resulting in volume regulation. We hypothesize that this weaker reaction of SOD1 astrocytes can result from the altered mechanisms of astrocyte swelling, for example due to a loss or dysfunction of potassium channels or ion co-transporters such as NKCC1. The key channels in the removal of K^+ from the extracellular space are Kir4.1, which are expressed exclusively in glial cells and primarily in astrocytes. Their altered expression has been previously described in rat (Bataveljic et al., 2012) and mouse (Kaiser et al., 2006) models of ALS with SOD1(G93A) mutation. Consistent with our results, lower expression of Kir4.1 was shown in the spinal cord (Kaiser et al., 2006) but not in the cerebral cortex (Bataveljic et al., 2012, Stevenson et al., 2023). Finally, the effect of increased K^+ concentration on the activity of other transport mechanisms, such as glutamate transporters and others, should be mentioned. Since increased extracellular K^+ concentration induces depolarization of astrocyte membranes (Du et al., 2018), other cellular voltage-dependent processes are likely to be affected. Therefore, we cannot exclude that the reduced astrocyte swelling observed under exposure to high K^+ levels is not only due to changes in

Kir4.1 expression, but also reflects changes in the expression/function of glutamate or ion co-transporters.

Astrogliosis and the volume regulation impairment we observed are closely connected to changes in the ECS diffusion parameters. Results from RTI measurements performed in the brain and spinal cord slices unveiled alterations in the ECS parameters following the exposure to two distinct potassium concentrations - 20 and 50 mM K^+. Application of both K^+ concentrations resulted in a noted decrease in the ECS volume fraction, indicating a compensatory shrinkage of the ECS caused by swelling of cells and/or their components. Our measurements revealed that the effect of lower potassium concentration (20 mM) does not show any significant differences in a typical time course of the ECS parameter changes between the CTRL and SOD1 mice in either the brain or the spinal cord.

In the cortex, the inter-group differences were also not evoked with the higher concentration of potassium (50 mM). In contrast, the measurements in the spinal cord indicated that 50 mM K^+ has a more pronounced effect in CTRL than in SOD1 mice - a drop of 32% (CTRL) and 13% (SOD1) from the initial values of the ECS volume fraction and a significant increase in tortuosity in CTRL but not in SOD1 mice. Regarding tortuosity, it is worth mentioning that its values in the spinal cord can be affected by the presence and density of the myelinated fibers that represent a major source of the diffusion barriers (Thorne et al., 2005) and influence even the initial tortuosity values, which were higher in the spinal cord than in the brain. The increase of tortuosity in the spinal cord of the CTRL mice can be therefore attributed at least partially to the closer alignment of myelin fibers, due to cellular swelling and the subsequent reduction in extracellular space that was larger in CTRL than in SOD1 mice. Our previous studies revealed that both ECS volume fraction and/or tortuosity could be strongly affected by the dynamic changes of the extracellular matrix (ECM) (Zamecnik et al., 2012, Zamecnik et al., 2004, Sucha et al., 2020). Alterations in the ECM composition were certainly shown in SOD1 rats in several studies, where they reported abnormally organized or damaged protective perineuronal net structures around the spinal MNs, as well as different expression profiles of chondroitin sulfate proteoglycans (CSPGs) (Forostyak et al., 2020, Forostyak et al., 2014, Cheung et al., 2024). We could thus expect that ECM alterations in the SOD1 tissue may affect the initial values of the ECS diffusion parameters. However, this assumption was not confirmed by our study as we did not detect any significant differences in the initial values of α and λ between CTRL and SOD1 mice either in the brain or spinal cord. It is not very likely that slowly developing and prolonged changes in the ECM composition might affect the rapidly developing ECS diffusion changes during acute cell swelling. We can only speculate that changes in the content of ECM, rich in water molecules bound to its negative charges, may affect the possibility of the cellular expansion and thus indirectly modulate cell swelling.

Comparison of the RTI measurements and astrocytic volume regulation analyses revealed similar responses, resulting from astrocyte swelling and compensatory shrinkage of the ECS volume in reaction to increased potassium concentrations and similar recovery during the washout period. Both techniques detected significant differences between CTRL and SOD1 mice only in the spinal cords during 50mM K^+. As demonstrated in our previous studies, such agreement of RTI and 3-D morphometry results is quite exceptional since the RTI-detected changes reflect the volume alterations of all cell types, not only those of the astrocytes (Kolenicova et al., 2020, Tureckova et al., 2021). Our findings therefore emphasize the crucial role of astrocytes in hyperkalemia-evoked cell swelling. This aligns with a study of Walch et al. (2020) showing that glial cells, particularly astrocytes, display marked vulnerability to alterations induced by potassium, while neurons show resistance to such disruptions. Walch et al. (2020) demonstrated that elevated extracellular potassium concentrations induce rapid and significant swelling of astrocytes, underscoring their crucial role in responding to changes in potassium levels. While astrocytes swiftly returned to baseline volume upon reverting to a control solution, they exhibited similar swelling responses upon reintroduction of elevated potassium levels. Conversely, neuronal volume remained largely unaffected by these potassium-induced changes, emphasizing the unique sensitivity of astrocytes to fluctuations in extracellular potassium and their pivotal role in maintaining cellular homeostasis (Walch et al., 2020).

As mentioned previously, the potassium homeostasis can be disrupted during pathological stages; however, it is not just potassium levels that can be altered during ALS. An imbalance of other ions such as Ca^{2+}, Na^{+} or Mg^{2+} is considered a significant aspect of the ALS pathology. Previous studies for instance reported reduced expression of calcium-buffering in post-mortem isolated MNs in ALS patients (Alexianu et al., 1994), an increase in persistent sodium currents in spinal and cortical MNs in SOD1 mice(Pieri et al., 2009, Kuo et al., 2005, Kuo et al., 2004), and alterations of the fast transient sodium currents generated by Na_v channels in spinal MNs in SOD1 mice (Zona et al., 2006). Nevertheless, the precise measurement of these elements in animal models or patients is not very frequent. Our data from the analysis of the CSF showed similar concentrations of K^{+}, Ca^{2+}, Na^{+}, Fe^{2+}, P and S in CTRLs and SOD1 samples. Potassium levels were previously determined in ALS SOD1/C57Bl6 mice by (Ding et al., 2024). Using *in vivo* recording with K^{+}- sensitive electrodes, they reported a significantly increased level of K^{+} in the cortex of diseased mice. We did not observe such a difference in the CSF of SOD1/GFAP/EGFP mice, which is most likely due to the different methodological approach. As (Stevenson et al., 2023) showed, the rate of potassium clearance and concentration can differ even within parts of the cortex. Therefore, analysis of CSF would not detect any region-specific potassium level alterations. When discussing potassium clearance in the context of ALS, it is also worth mentioning oligodendrocytes, which contribute to the clearance of excessive K^{+}. Similar to astrocytes, though, the Kir4.1 channel that is largely responsible for the clearance (Schirmer et al., 2018) was reported to be downregulated in the spinal cord of SOD1(G93A) rats (Peric et al., 2021). Interestingly, we detected a significantly decreased concentration of magnesium in CSF of ALS mice. Magnesium is involved in muscle function, the cellular antioxidant mechanism and neuronal signaling as it inhibits NMDA receptors, which helps to prevent excitotoxicity (Shindo et al., 2020). Thus, our data are in agreement with (Yasui et al., 1997), who found lower magnesium content in bones and ligaments in post mortem samples of ALS patients. Generally, magnesium deficiency has been considered a possible risk factor for ALS, which translated in further research when trying to explore the possibilities of magnesium supplementation to modify the course of the disease. However, at least in the SOD1 model, a study from (Pamphlett et al., 2003) reported no increased survival or delayed disease onset of mice being supplemented by higher doses of magnesium.

5 Conclusion

For the purposes of this study, we generated a crossbred mouse model of ALS in which EGFP is expressed specifically in astrocytes. This model allowed us to perform a functional study to assess the capability of astrocytes to regulate extracellular ion concentrations. We confirmed that astrocytes adopt reactive morphology in the motor cortex and ventral horns of the spinal cord during ALS-like pathology in the SOD1/GFAP/EGFP model. Our findings from functional measurements suggest a spinal cord-specific alteration in astrocytic ability to take up potassium ions during exposure to high potassium concentrations, which is associated with a decrease in Kir4.1 expression. In cortical astrocytes, the ability of potassium uptake appears to remain unchanged and the expression of Kir4.1 is unaffected despite reactive morphology. These findings are manifested both at the level of astrocyte swelling and changes in ECS parameters. The observed differences in astrocyte buffering capacity highlight the complex interplay between regional astrocyte function and ALS pathophysiology, emphasizing the need for further investigations into region-specific mechanisms underlying potassium dysregulation in ALS.

6 Conflict of Interest

The authors declare that the research was conducted in the absence of any commercial or financial relationships that could be construed as a potential conflict of interest.

7 Author Contributions

TF performed 3D-morphometry measurements and analysis, IHC measurements, CSF collection, interpreted all data, wrote manuscript and prepared figures. JT performed IHC analysis and contributed to the manuscript editing. OV and MK performed the behavioral testing. MCH performed RTI measurements and analysis. NS contributed to 3D-morphometry analysis. SM performed the elemental analysis. LV contributed to the manuscript editing and MA conceived and supervised the study.

8 Funding

This study was supported by the European Union's Horizon 2020 Research and Innovation Program (registration number 956325), by project LX22NPO5107 (MEYS): Financed by EU—Next Generation EU. Microscopy was done at the Microscopy Service Center of the Institute of Experimental Medicine CAS supported by the MEYS CR (LM2023050 Czech-Bioimaging). The work was also supported by the Ministry of Education, Youth and Sports of the Czech Republic (Research Infrastructure NanoEnviCZ, LM2018124) and The European Union-European Structural and Investments Funds in the frame of the Research Development and Education-project Pro-NanoEnviCz operational program (Project No. CZ.02.1.01/0.0/0.0/16_013/0001821).

9 Acknowledgments

The authors would like to thank Helena Pavlikova and Marketa Hemerova for their excellent technical assistance and Frances Zatrepalkova for proofreading the manuscript.

Table 1 Contents of experimental solutions.

Compounds	aCSF [mM]	Isolation solution [mM]	20 mM $aCSF_{K+}$ [mM]	50 mM $aCSF_{K+}$ [mM]
NaCl	122	-	105	75
NMDG	-	110	-	-
KCl	3	2.5	20	50
$NaHCO_3$	28	24.5	28	28
Na_2HPO_4	1.25	1.25	1.25	1.25
Glucose	10	20	10	10

$CaCl_2$	1.5	0.5	1.5	1.5
$MgCl_2$	1.3	7	1.3	1.3
Osmolality (mOsmol/kg)	~300	~300	~300	~300

Abbreviations: NMDG (N-methyl-D-glucamine); aCSF (artificial cerebrospinal fluid); 20 or 50 mM $aCSF_{K+}$ (artificial cerebrospinal fluid with elevated K^+ concentration).

Table 2 Concentration of elements in the CSF of GFAP/EGFP mice

mM/l	SOD1	CTRL
Ca	1.12 ± 0.1	1.25 ± 0.05
Fe	0.01 ± 0.01	0.01 ± 0.01
K	3.20 ± 0.21	3.49 ± 0.26
Mg	0.76 ± 0.03	0.81 ± 0.05
Na	152.20 ± 2.53	149.73 ± 7.64
P	1.38 ± 0.24	1.45 ± 0.14
S	0.68 ± 0.25	0.83 ± 0.2

Abbreviations: SOD1, superoxide dismutase transgenic mice on the FVB/N background; CTRL, control mice on the FVB/N background.

ALEXIANU, M. E., HO, B. K., MOHAMED, A. H., LA BELLA, V., SMITH, R. G. & APPEL, S. H. 1994. The role of calcium-binding proteins in selective motoneuron vulnerability in amyotrophic lateral sclerosis. *Ann Neurol,* 36**,** 846-58.

AMLEROVA, Z., CHMELOVA, M., ANDEROVA, M. & VARGOVA, L. 2024. Reactive gliosis in traumatic brain injury: a comprehensive review. *Front Cell Neurosci,* 18**,** 1335849.

AWADOVA, T., PIVONKOVA, H., HERMANOVA, Z., KIRDAJOVA, D., ANDEROVA, M. & MALINSKY, J. 2018. Cell volume changes as revealed by fluorescence microscopy: Global vs local approaches. *J Neurosci Methods,* 306**,** 38-44.

BAKER, D. J., BLACKBURN, D. J., KEATINGE, M., SOKHI, D., VISKAITIS, P., HEATH, P. R., FERRAIUOLO, L., KIRBY, J. & SHAW, P. J. 2015. Lysosomal and phagocytic activity is increased in astrocytes during disease progression in the SOD1 (G93A) mouse model of amyotrophic lateral sclerosis. *Front Cell Neurosci,* 9**,** 410.

BATAVELJIC, D., NIKOLIC, L., MILOSEVIC, M., TODOROVIC, N. & ANDJUS, P. R. 2012. Changes in the astrocytic aquaporin-4 and inwardly rectifying potassium channel expression in the brain of the amyotrophic lateral sclerosis SOD1(G93A) rat model. *Glia,* 60**,** 1991-2003.

CHEUNG, S. W., BHAVNANI, E., SIMMONS, D. G., BELLINGHAM, M. C. & NOAKES, P. G. 2024. Perineuronal nets are phagocytosed by MMP-9 expressing microglia and astrocytes in the SOD1(G93A) ALS mouse model. *Neuropathol Appl Neurobiol,* 50**,** e12982.

DAVID, Y., CACHEAUX, L. P., IVENS, S., LAPILOVER, E., HEINEMANN, U., KAUFER, D. & FRIEDMAN, A. 2009. Astrocytic dysfunction in epileptogenesis: consequence of altered potassium and glutamate homeostasis? *J Neurosci,* 29**,** 10588-99.

DING, F., SUN, Q., LONG, C., RASMUSSEN, R. N., PENG, S., XU, Q., KANG, N., SONG, W., WEIKOP, P., GOLDMAN, S. A. & NEDERGAARD, M. 2024. Dysregulation of extracellular potassium distinguishes healthy ageing from neurodegeneration. *Brain,* 147**,** 1726-1739.

DU, Y., WANG, W., LUTTON, A. D., KIYOSHI, C. M., MA, B., TAYLOR, A. T., OLESIK, J. W., MCTIGUE, D. M., ASKWITH, C. C. & ZHOU, M. 2018. Dissipation of transmembrane potassium gradient is the main cause of cerebral ischemia-induced depolarization in astrocytes and neurons. *Exp Neurol,* 303**,** 1-11.

FERRAIUOLO, L., HIGGINBOTTOM, A., HEATH, P. R., BARBER, S., GREENALD, D., KIRBY, J. & SHAW, P. J. 2011. Dysregulation of astrocyte-motoneuron cross-talk in mutant superoxide dismutase 1-related amyotrophic lateral sclerosis. *Brain,* 134**,** 2627-41.

FILIPI, T., MATUSOVA, Z., ABAFFY, P., VANATKO, O., TURECKOVA, J., BENESOVA, S., KUBISKOVA, M., KIRDAJOVA, D., ZAHUMENSKY, J., VALIHRACH, L. & ANDEROVA, M. 2023. Cortical glia in SOD1(G93A) mice are subtly affected by ALS-like pathology. *Sci Rep,* 13**,** 6538.

FOROSTYAK, S., FOROSTYAK, O., KWOK, J. C. F., ROMANYUK, N., REHOROVA, M., KRISKA, J., DAYANITHI, G., RAHA-CHOWDHURY, R., JENDELOVA, P., ANDEROVA, M., FAWCETT, J. W. & SYKOVA, E. 2020. Transplantation of Neural Precursors Derived from Induced Pluripotent Cells Preserve Perineuronal Nets and Stimulate Neural Plasticity in ALS Rats. *Int J Mol Sci,* 21.

FOROSTYAK, S., HOMOLA, A., TURNOVCOVA, K., SVITIL, P., JENDELOVA, P. & SYKOVA, E. 2014. Intrathecal delivery of mesenchymal stromal cells protects the structure of altered perineuronal nets in SOD1 rats and amends the course of ALS. *Stem Cells,* 32**,** 3163-72.

GERBER, Y. N., SABOURIN, J. C., RABANO, M., VIVANCO, M. & PERRIN, F. E. 2012. Early functional deficit and microglial disturbances in a mouse model of amyotrophic lateral sclerosis. *PLoS One,* 7**,** e36000.

GOMES, C., CUNHA, C., NASCIMENTO, F., RIBEIRO, J. A., VAZ, A. R. & BRITES, D. 2019. Cortical Neurotoxic Astrocytes with Early ALS Pathology and miR-146a Deficit Replicate Gliosis Markers of Symptomatic SOD1G93A Mouse Model. *Mol Neurobiol,* 56**,** 2137-2158.

GOMES, C., SEQUEIRA, C., BARBOSA, M., CUNHA, C., VAZ, A. R. & BRITES, D. 2020. Astrocyte regional diversity in ALS includes distinct aberrant phenotypes with common and causal pathological processes. *Exp Cell Res,* 395**,** 112209.

GURNEY, M. E., PU, H., CHIU, A. Y., DAL CANTO, M. C., POLCHOW, C. Y., ALEXANDER, D. D., CALIENDO, J., HENTATI, A., KWON, Y. W., DENG, H. X. & ET AL. 1994. Motor neuron degeneration in mice that express a human Cu,Zn superoxide dismutase mutation. *Science,* 264**,** 1772-5.

GUTTENPLAN, K. A., WEIGEL, M. K., ADLER, D. I., COUTHOUIS, J., LIDDELOW, S. A., GITLER, A. D. & BARRES, B. A. 2020. Knockout of reactive astrocyte activating factors slows disease progression in an ALS mouse model. *Nat Commun,* 11**,** 3753.

HANANI, M. & SPRAY, D. C. 2020. Emerging importance of satellite glia in nervous system function and dysfunction. *Nat Rev Neurosci,* 21**,** 485-498.

HARADA, Y., NAGAO, Y., SHIMIZU, S., SERIKAWA, T., TERADA, R., FUJIMOTO, M., OKUDA, A., MUKAI, T., SASA, M., KURACHI, Y. & OHNO, Y. 2013. Expressional analysis of inwardly rectifying Kir4.1 channels in Noda epileptic rat (NER). *Brain Res,* 1517**,** 141-9.

HEIMAN-PATTERSON, T. D., SHER, R. B., BLANKENHORN, E. A., ALEXANDER, G., DEITCH, J. S., KUNST, C. B., MARAGAKIS, N. & COX, G. 2011. Effect of genetic background on phenotype variability in transgenic mouse models of amyotrophic lateral sclerosis: a window of opportunity in the search for genetic modifiers. *Amyotroph Lateral Scler,* 12**,** 79-86.

HELLAS, J. A. & ANDREW, R. D. 2021. Neuronal Swelling: A Non-osmotic Consequence of Spreading Depolarization. *Neurocrit Care,* 35**,** 112-134.

JANIGRO, D. 2012. Are you in or out? Leukocyte, ion, and neurotransmitter permeability across the epileptic blood-brain barrier. *Epilepsia,* 53 Suppl 1**,** 26-34.

KAHLE, K. T., KHANNA, A. R., ALPER, S. L., ADRAGNA, N. C., LAUF, P. K., SUN, D. & DELPIRE, E. 2015. K-Cl cotransporters, cell volume homeostasis, and neurological disease. *Trends Mol Med,* 21**,** 513-23.

KAISER, M., MALETZKI, I., HULSMANN, S., HOLTMANN, B., SCHULZ-SCHAEFFER, W., KIRCHHOFF, F., BAHR, M. & NEUSCH, C. 2006. Progressive loss of a glial potassium channel (KCNJ10) in the spinal cord of the SOD1 (G93A) transgenic mouse model of amyotrophic lateral sclerosis. *J Neurochem,* 99**,** 900-12.

KAUR, A., SHUKEN, S., YANG, A. C. & IRAM, T. 2023. A protocol for collection and infusion of cerebrospinal fluid in mice. *STAR Protoc,* 4**,** 102015.

KEEP, R. F., ULANSKI, L. J., 2ND, XIANG, J., ENNIS, S. R. & LORRIS BETZ, A. 1999. Blood-brain barrier mechanisms involved in brain calcium and potassium homeostasis. *Brain Res,* 815**,** 200-5.

KHAKH, B. S., BEAUMONT, V., CACHOPE, R., MUNOZ-SANJUAN, I., GOLDMAN, S. A. & GRANTYN, R. 2017. Unravelling and Exploiting Astrocyte Dysfunction in Huntington's Disease. *Trends Neurosci,* 40**,** 422-437.

KOLENICOVA, D., TURECKOVA, J., PUKAJOVA, B., HARANTOVA, L., KRISKA, J., KIRDAJOVA, D., VORISEK, I., KAMENICKA, M., VALIHRACH, L., ANDROVIC, P., KUBISTA, M., VARGOVA, L. & ANDEROVA, M. 2020. High potassium exposure reveals the altered ability of astrocytes to regulate their volume in the aged hippocampus of GFAP/EGFP mice. *Neurobiol Aging,* 86**,** 162-181.

KUO, J. J., SCHONEWILLE, M., SIDDIQUE, T., SCHULTS, A. N., FU, R., BAR, P. R., ANELLI, R., HECKMAN, C. J. & KROESE, A. B. 2004. Hyperexcitability of cultured spinal motoneurons from presymptomatic ALS mice. *J Neurophysiol,* 91**,** 571-5.

KUO, J. J., SIDDIQUE, T., FU, R. & HECKMAN, C. J. 2005. Increased persistent Na(+) current and its effect on excitability in motoneurones cultured from mutant SOD1 mice. *J Physiol,* 563**,** 843-54.

LAPILOVER, E. G., LIPPMANN, K., SALAR, S., MASLAROVA, A., DREIER, J. P., HEINEMANN, U. & FRIEDMAN, A. 2012. Peri-infarct blood-brain barrier dysfunction facilitates induction of spreading depolarization associated with epileptiform discharges. *Neurobiol Dis,* 48**,** 495-506.

LARSEN, B. R., STOICA, A. & MACAULAY, N. 2016. Managing Brain Extracellular K(+) during Neuronal Activity: The Physiological Role of the Na(+)/K(+)-ATPase Subunit Isoforms. *Front Physiol,* 7**,** 141.

MANCUSO, R., OLIVAN, S., OSTA, R. & NAVARRO, X. 2011. Evolution of gait abnormalities in SOD1(G93A) transgenic mice. *Brain Res,* 1406**,** 65-73.

MEAD, R. J., BENNETT, E. J., KENNERLEY, A. J., SHARP, P., SUNYACH, C., KASHER, P., BERWICK, J., PETTMANN, B., BATTAGLIA, G., AZZOUZ, M., GRIERSON, A. & SHAW, P. J. 2011. Optimised and rapid pre-clinical screening in the SOD1(G93A) transgenic mouse model of amyotrophic lateral sclerosis (ALS). *PLoS One,* 6**,** e23244.

MILLER, S. J., GLATZER, J. C., HSIEH, Y. C. & ROTHSTEIN, J. D. 2018. Cortical astroglia undergo transcriptomic dysregulation in the G93A SOD1 ALS mouse model. *J Neurogenet,* 32**,** 322-335.

MILLER, S. J., ZHANG, P. W., GLATZER, J. & ROTHSTEIN, J. D. 2017. Astroglial transcriptome dysregulation in early disease of an ALS mutant SOD1 mouse model. *J Neurogenet,* 31**,** 37-48.

MULLER, M. & SOMJEN, G. G. 2000. Na(+) and K(+) concentrations, extra- and intracellular voltages, and the effect of TTX in hypoxic rat hippocampal slices. *J Neurophysiol,* 83**,** 735-45.

NAGAI, M., RE, D. B., NAGATA, T., CHALAZONITIS, A., JESSELL, T. M., WICHTERLE, H. & PRZEDBORSKI, S. 2007. Astrocytes expressing ALS-linked mutated SOD1 release factors selectively toxic to motor neurons. *Nat Neurosci,* 10**,** 615-22.

NEDERGAARD, M. & VERKHRATSKY, A. 2012. Artifact versus reality--how astrocytes contribute to synaptic events. *Glia,* 60**,** 1013-23.

NICHOLSON, C. 1993. Ion-selective microelectrodes and diffusion measurements as tools to explore the brain cell microenvironment. *J Neurosci Methods,* 48**,** 199-213.

NICHOLSON, C. & HRABETOVA, S. 2017. Brain Extracellular Space: The Final Frontier of Neuroscience. *Biophys J,* 113**,** 2133-2142.

NICHOLSON, C. & PHILLIPS, J. M. 1981. Ion diffusion modified by tortuosity and volume fraction in the extracellular microenvironment of the rat cerebellum. *J Physiol,* 321**,** 225-57.

NIESSEN, H. G., ANGENSTEIN, F., SANDER, K., KUNZ, W. S., TEUCHERT, M., LUDOLPH, A. C., HEINZE, H. J., SCHEICH, H. & VIELHABER, S. 2006. In vivo quantification of spinal and bulbar motor neuron degeneration in the G93A-SOD1 transgenic mouse model of ALS by T2 relaxation time and apparent diffusion coefficient. *Exp Neurol,* 201**,** 293-300.

NIKODEMOVA, M. & WATTERS, J. J. 2011. Outbred ICR/CD1 mice display more severe neuroinflammation mediated by microglial TLR4/CD14 activation than inbred C57Bl/6 mice. *Neuroscience,* 190**,** 67-74.

NOLTE, C., MATYASH, M., PIVNEVA, T., SCHIPKE, C. G., OHLEMEYER, C., HANISCH, U. K., KIRCHHOFF, F. & KETTENMANN, H. 2001. GFAP promoter-controlled EGFP-expressing transgenic mice: a tool to visualize astrocytes and astrogliosis in living brain tissue. *Glia,* 33**,** 72-86.

OHNO, Y., KUNISAWA, N. & SHIMIZU, S. 2021. Emerging Roles of Astrocyte Kir4.1 Channels in the Pathogenesis and Treatment of Brain Diseases. *Int J Mol Sci,* 22.

PAMPHLETT, R., TODD, E., VINK, R., MCQUILTY, R. & CHEEMA, S. S. 2003. Magnesium supplementation does not delay disease onset or increase survival in a mouse model of familial ALS. *J Neurol Sci,* 216**,** 95-8.

PERIC, M., NIKOLIC, L., ANDJUS, P. R. & BATAVELJIC, D. 2021. Dysfunction of oligodendrocyte inwardly rectifying potassium channel in a rat model of amyotrophic lateral sclerosis. *Eur J Neurosci,* 54**,** 6339-6354.

PIERI, M., CARUNCHIO, I., CURCIO, L., MERCURI, N. B. & ZONA, C. 2009. Increased persistent sodium current determines cortical hyperexcitability in a genetic model of amyotrophic lateral sclerosis. *Exp Neurol,* 215**,** 368-79.

PIETROBON, D. & MOSKOWITZ, M. A. 2014. Chaos and commotion in the wake of cortical spreading depression and spreading depolarizations. *Nat Rev Neurosci,* 15**,** 379-93.

PIVONKOVA, H., HERMANOVA, Z., KIRDAJOVA, D., AWADOVA, T., MALINSKY, J., VALIHRACH, L., ZUCHA, D., KUBISTA, M., GALISOVA, A., JIRAK, D. & ANDEROVA, M. 2018. The Contribution of TRPV4 Channels to Astrocyte Volume Regulation and Brain Edema Formation. *Neuroscience,* 394**,** 127-143.

RIDLER, T. W. & CALVARD, S. 1978. Picture Thresholding Using an Iterative Selection Method. *Ieee Transactions on Systems Man and Cybernetics,* 8**,** 630-632.

ROSSI, D. J., BRADY, J. D. & MOHR, C. 2007. Astrocyte metabolism and signaling during brain ischemia. *Nat Neurosci,* 10**,** 1377-86.

SCHINDELIN, J., ARGANDA-CARRERAS, I., FRISE, E., KAYNIG, V., LONGAIR, M., PIETZSCH, T., PREIBISCH, S., RUEDEN, C., SAALFELD, S., SCHMID, B., TINEVEZ, J. Y., WHITE, D. J., HARTENSTEIN, V., ELICEIRI, K., TOMANCAK, P. & CARDONA, A. 2012. Fiji: an open-source platform for biological-image analysis. *Nat Methods,* 9**,** 676-82.

SCHIRMER, L., MOBIUS, W., ZHAO, C., CRUZ-HERRANZ, A., BEN HAIM, L., CORDANO, C., SHIOW, L. R., KELLEY, K. W., SADOWSKI, B., TIMMONS, G., PROBSTEL, A. K., WRIGHT, J. N., SIN, J. H., DEVEREUX, M., MORRISON, D. E., CHANG, S. M., SABEUR, K., GREEN, A. J., NAVE, K. A., FRANKLIN, R. J. & ROWITCH, D. H. 2018. Oligodendrocyte-encoded Kir4.1 function is required for axonal integrity. *Elife,* 7.

SHINDO, Y., YAMANAKA, R., HOTTA, K. & OKA, K. 2020. Inhibition of Mg(2+) Extrusion Attenuates Glutamate Excitotoxicity in Cultured Rat Hippocampal Neurons. *Nutrients,* 12.

SONG, M. & YU, S. P. 2014. Ionic regulation of cell volume changes and cell death after ischemic stroke. *Transl Stroke Res,* 5**,** 17-27.

STEVENSON, R., SAMOKHINA, E., MANGAT, A., ROSSETTI, I., PURUSHOTHAM, S. S., MALLADI, C. S., MORLEY, J. W. & BUSKILA, Y. 2023. Astrocytic K(+) clearance during disease progression in amyotrophic lateral sclerosis. *Glia,* 71**,** 2456-2472.

SUCHA, P., CHMELOVA, M., KAMENICKA, M., BOCHIN, M., OOHASHI, T. & VARGOVA, L. 2020. The Effect of Hapln4 Link Protein Deficiency on Extracellular Space Diffusion Parameters and Perineuronal Nets in the Auditory System During Aging. *Neurochem Res,* 45**,** 68-82.

SYKOVÁ, E. 1992. Ion-selective electrodes. *Monitoring neuronal cells: a practical approach (Stamford J, ed)***,** 261-282.

SYKOVA, E. & NICHOLSON, C. 2008. Diffusion in brain extracellular space. *Physiol Rev,* 88**,** 1277-340.

THORNE, R. G., HRABETOVA, S. & NICHOLSON, C. 2005. Diffusion measurements for drug design. *Nat Mater,* 4**,** 713; author reply 714.

THORNE, R. G. & NICHOLSON, C. 2006. In vivo diffusion analysis with quantum dots and dextrans predicts the width of brain extracellular space. *Proceedings of the National Academy of Sciences of the United States of America,* 103**,** 5567-72.

TURECKOVA, J., KAMENICKA, M., KOLENICOVA, D., FILIPI, T., HERMANOVA, Z., KRISKA, J., MESZAROSOVA, L., PUKAJOVA, B., VALIHRACH, L., ANDROVIC, P., ZUCHA, D., CHMELOVA, M., VARGOVA, L. & ANDEROVA, M. 2021. Compromised Astrocyte Swelling/Volume Regulation in the Hippocampus of the Triple Transgenic Mouse Model of Alzheimer's Disease. *Front Aging Neurosci,* 13**,** 783120.

VAN PUTTEN, M., FAHLKE, C., KAFITZ, K. W., HOFMEIJER, J. & ROSE, C. R. 2021. Dysregulation of Astrocyte Ion Homeostasis and Its Relevance for Stroke-Induced Brain Damage. *Int J Mol Sci,* 22.

WALCH, E., MURPHY, T. R., CUVELIER, N., ALDOGHMI, M., MOROZOVA, C., DONOHUE, J., YOUNG, G., SAMANT, A., GARCIA, S., ALVAREZ, C., BILAS, A., DAVILA, D., BINDER, D. K. & FIACCO, T. A. 2020. Astrocyte-Selective Volume Increase in Elevated Extracellular Potassium Conditions Is Mediated by the Na(+)/K(+) ATPase and Occurs Independently of Aquaporin 4. *ASN Neuro,* 12**,** 1759091420967152.

WILCOCK, D. M., VITEK, M. P. & COLTON, C. A. 2009. Vascular amyloid alters astrocytic water and potassium channels in mouse models and humans with Alzheimer's disease. *Neuroscience,* 159**,** 1055-69.

YAMANAKA, K., CHUN, S. J., BOILLEE, S., FUJIMORI-TONOU, N., YAMASHITA, H., GUTMANN, D. H., TAKAHASHI, R., MISAWA, H. & CLEVELAND, D. W. 2008. Astrocytes as determinants of disease progression in inherited amyotrophic lateral sclerosis. *Nat Neurosci,* 11**,** 251-3.

YASUI, M., OTA, K. & YOSHIDA, M. 1997. Effects of low calcium and magnesium dietary intake on the central nervous system tissues of rats and calcium-magnesium related disorders in the amyotrophic lateral sclerosis focus in the Kii Peninsula of Japan. *Magnes Res,* 10**,** 39-50.

ZAMECNIK, J., HOMOLA, A., CICANIC, M., KUNCOVA, K., MARUSIC, P., KRSEK, P., SYKOVA, E. & VARGOVA, L. 2012. The extracellular matrix and diffusion barriers in focal cortical dysplasias. *Eur J Neurosci,* 36**,** 2017-24.

ZAMECNIK, J., VARGOVA, L., HOMOLA, A., KODET, R. & SYKOVA, E. 2004. Extracellular matrix glycoproteins and diffusion barriers in human astrocytic tumours. *Neuropathol Appl Neurobiol,* 30**,** 338-50.

ZONA, C., PIERI, M. & CARUNCHIO, I. 2006. Voltage-dependent sodium channels in spinal cord motor neurons display rapid recovery from fast inactivation in a mouse model of amyotrophic lateral sclerosis. *J Neurophysiol,* 96**,** 3314-22.

Figure legends

Figure 1 Evaluation of pathology by behavioral testing A) Representative picture of the wire grind hang test execution. B) Representative picture of the Rotarod test execution. C) The hanging wire test confirmed the motor strength decline in SOD1/GFAP/EGFP mice compared to CTRLs. D) Rotarod measurements analysis revealed the decline of motor coordination in SOD1/GFAP/EGFP mice compared to CTRLs and thus confirmed the phenotype. E) Comparison of motor strength revealed significantly faster progression in SOD1 GFAP/EGFP mice compared to the initial SOD1/C57Bl6. F) Similar results were observed in Rotarod results, showing a faster decrease of motor coordination in SOD1 GFAP/EGFP mice. Data are presented as mean ± SEM. n = the number of mice. Repeated measures of two-way ANOVA with Holm-Sidak's multiple comparison correction were used to analyze the differences between groups

Figure 2 Assessment of astrocyte reactivity based on GFAP expression levels A) Representative tile scans of motor cortex used for fluorescence analysis. The SOD1 cortex is showing signs of astrogliosis. B) Fluorescence analysis of astrogliosis in the motor and somatosensory cortex of SOD1 and CTRL mice showed astrogliosis in SOD1 mice. C) Representative pictures of astrocytes in the ventral horns of the spinal cord. D) Fluorescence analysis of astrogliosis in the spinal cord confirmed a gliosis and morphological shift of astrocytes towards the reactive shape. Data are presented as mean ± SEM. n = the number of brain hemispheres or spinal cord slices, respectively. Unpaired t-test was used to analyze the differences between groups. CTRL, control mice on the FVB/N background; SOD1, superoxide dismutase transgenic mice on the FVB/N background.

Figure 3 Swelling of astrocytes in response to different potassium concentrations (A) Superimposed confocal images of an EGFP-labeled cortical astrocyte were recorded throughout the measurement. A control image was taken during the application of artificial cerebrospinal solution (aCSF). The volume of astrocytes was recorded every 5 min during the application of aCSF_{K+} for 20 min. The last 2 stacks of astrocyte images were recorded at an interval of 20 min during 40-min in aCSF. (B, C) The time course of volume changes of cortical (B) and spinal (C) astrocytes throughout the measurement in 20mM aCSF_{K+}. (D, E) Time course of volume changes of cortical (D) and spinal (E) astrocytes throughout the measurement in 50mM aCSF_{K+}. Data are presented as mean ± SEM. n = number of cells. Two-way ANOVA with Holm-Sidak's multiple comparison correction were used to analyze the differences between groups CTRL, control mice on the FVB/N background; SOD1, superoxide dismutase transgenic mice on the FVB/N background.

Figure 4 Measurements of ECS parameters in mouse acute brain slices Averaged data of α – volume fraction and λ - tortuosity measured in CTRL and SOD1 mice at resting conditions (22-24°C, Ctrl) and at 5-minute intervals during application of 20mM (A, B) or 50mM (C, D) aCSF_{K+} and washout (aCSF). Data are presented as mean ± SEM. n = the number of slices. Two-way ANOVA with Holm-Sidak's multiple comparison correction were used to analyze the differences between groups Ctrl, control (initial measurements); CTRL, control mice on the FVB/N background; SOD1, superoxide dismutase transgenic mice on the FVB/N background.

Figure 5 Measurements of ECS in acute spinal cord slices Averaged data of α – volume fraction and λ - tortuosity measured in CTRL and SOD1 mice at resting conditions (22-24°C, Ctrl), and at 5-minute intervals during application of 20mM (A, B) and 50mM (C, D) aCSF$_{K+}$ and washout (aCSF). Data are presented as mean ± SEM. n = the number of slices. Two-way ANOVA with Holm-Sidak's multiple comparison correction were used to analyze the differences between groups Ctrl, control (initial measurements); CTRL, control mice on the FVB/N background; SOD1, superoxide dismutase transgenic mice on the FVB/N background.

Figure 6 Immunohistochemical analysis of Kir4.1 expression A) A representative picture of Kir4.1 staining in the motor cortex. B) Fluorescence analysis of Kir4.1 in the primary and secondary motor cortex and somatosensory cortex. C) Fluorescence analysis of Kir4.1 in the ventral horns of the spinal cord. Data are presented as mean ± SEM. n = the number of brain hemispheres or spinal cord slices, respectively. Unpaired t-test was used to analyze the differences between groups. CTRL, control mice on the FVB/N background; SOD1, superoxide dismutase transgenic mice on the FVB/N background

Figure 7 Elemental analysis of CSF isolated from GFAP/EGFP mice A) A sample of CSF demonstrating the purity of all samples used for the analysis. B) A comparison of potassium concentrations in the CSF of control vs. SOD1 mice. C) A comparison of magnesium levels in the CSF of control vs. SOD1 mice. Data are presented as mean ± SEM. n = the number of mice. Unpaired t-test with Welch´s correction was used to analyze the differences between groups.CTRL, control mice on the FVB/N background; SOD1, superoxide dismutase transgenic mice on the FVB/N background.

Figure 1.TIF

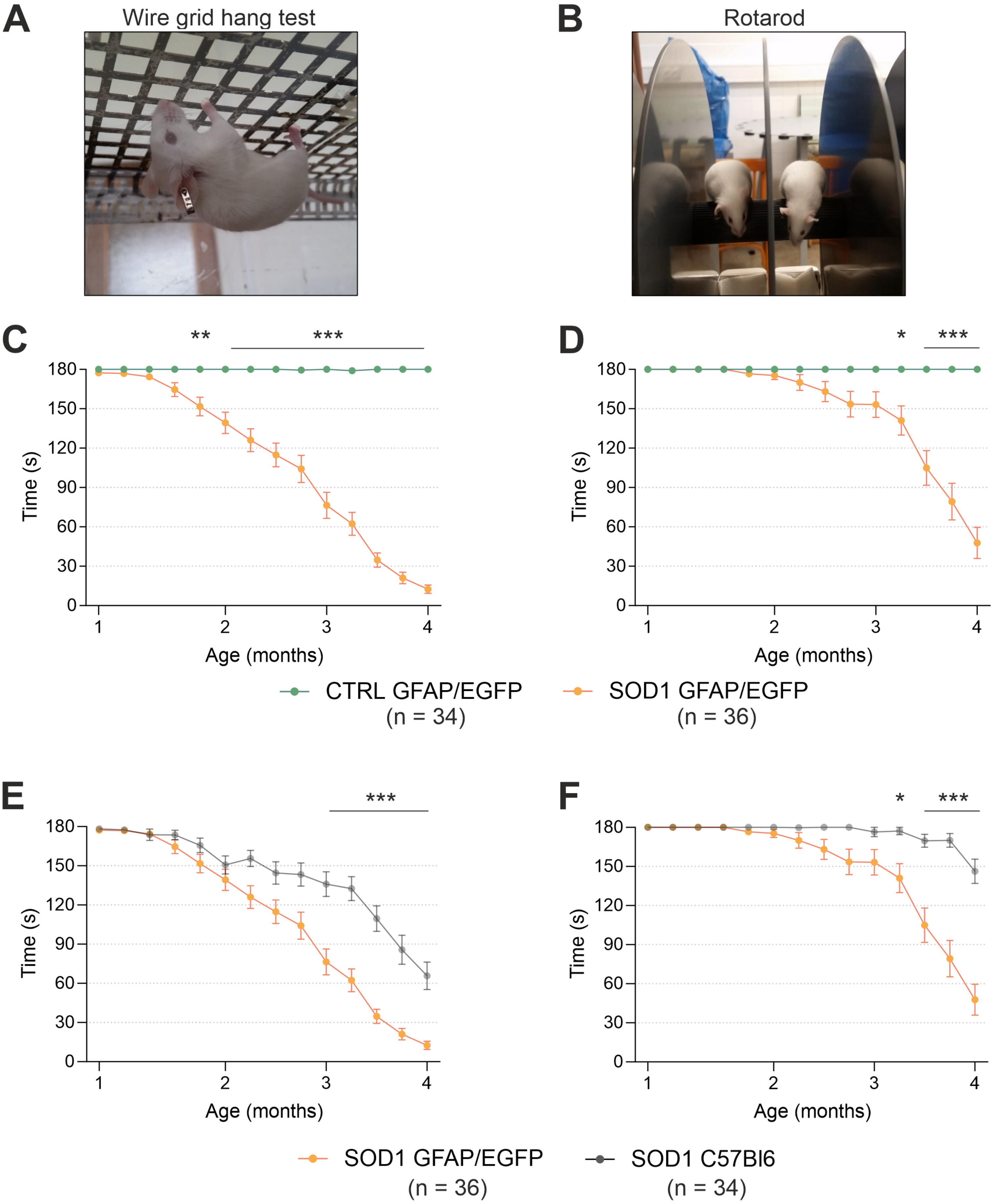
A
Wire grid hang test
B
Rotarod
C
**
***
180
150
120
90
60
30
0
Time (s)
1
2
3
4
Age (months)
D
*
***
180
150
120
90
60
30
0
Time (s)
1
2
3
4
Age (months)
CTRL GFAP/EGFP
(n = 34)
SOD1 GFAP/EGFP
(n = 36)
E
***
180
150
120
90
60
30
0
Time (s)
1
2
3
4
Age (months)
F
*
***
180
150
120
90
60
30
0
Time (s)
1
2
3
4
Age (months)
SOD1 GFAP/EGFP
(n = 36)
SOD1 C57Bl6
(n = 34)

Figure 2.TIF

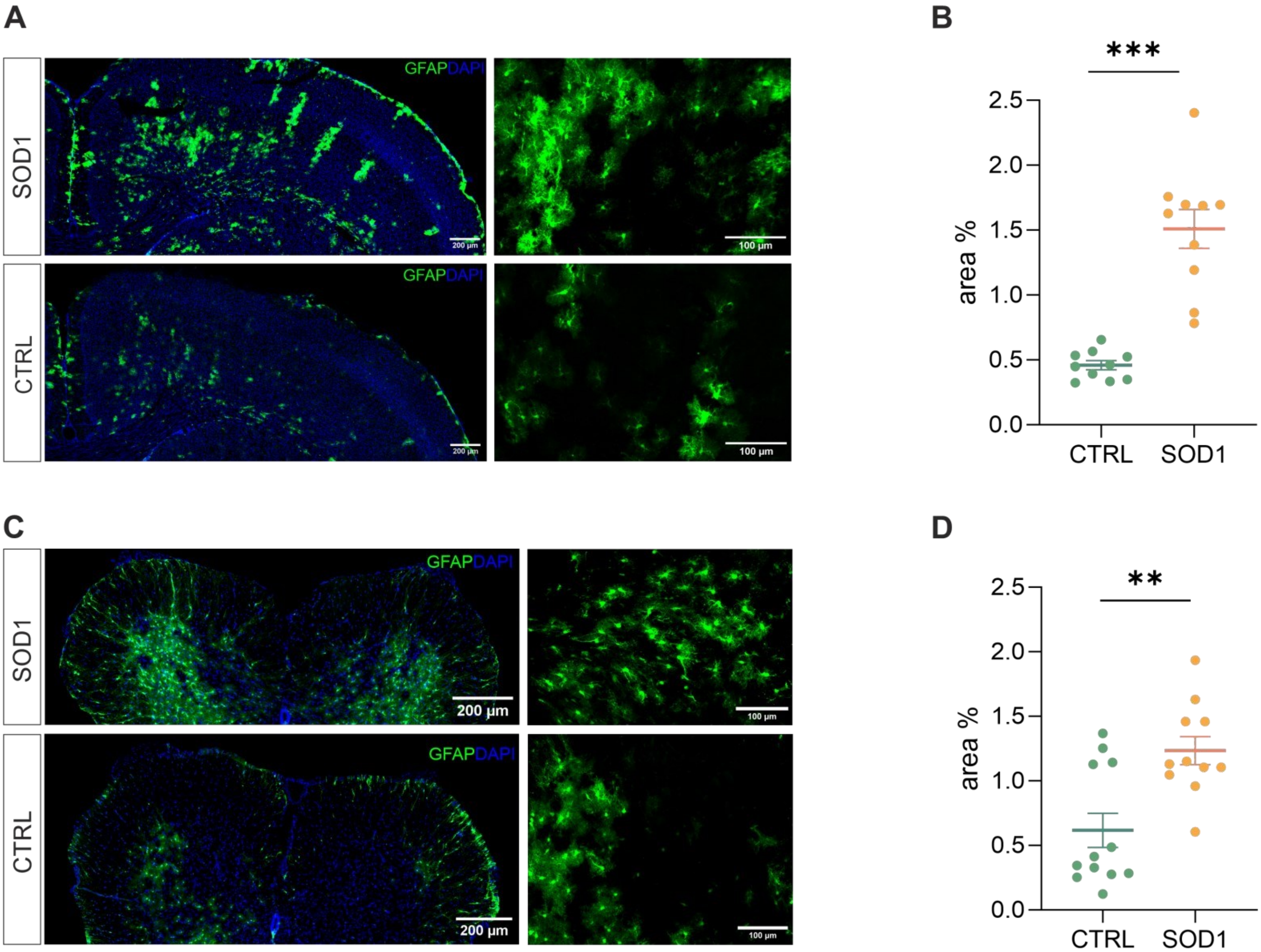
A
SOD1
CTRL
GFAPDAPI
200 µm
100 µm
B
***
area %
2.5
2.0
1.5
1.0
0.5
0.0
CTRL
SOD1
C
SOD1
CTRL
GFAPDAPI
200 µm
100 µm
D
**
area %
2.5
2.0
1.5
1.0
0.5
0.0
CTRL
SOD1

Figure 3.JPEG

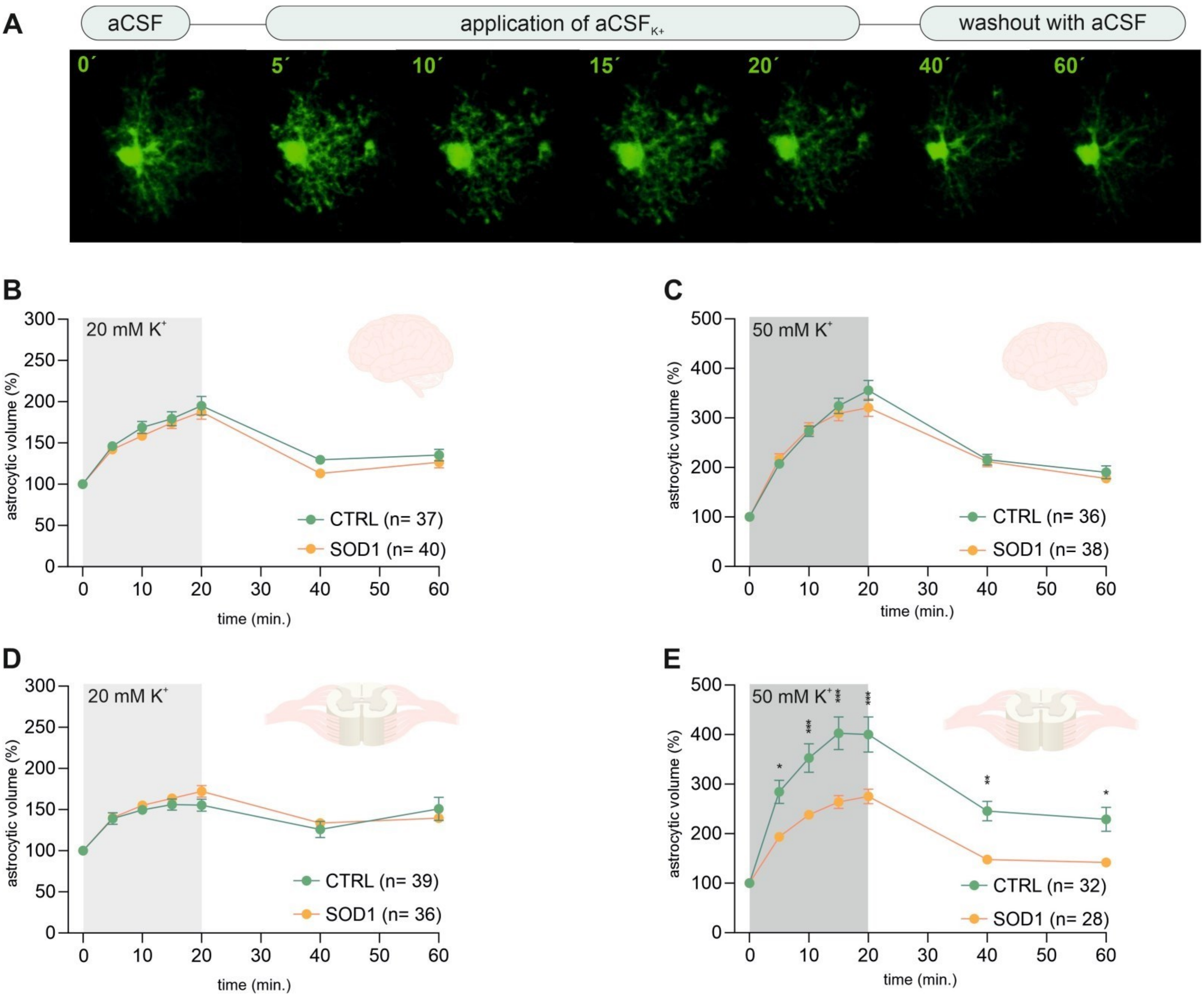

Figure 4.TIF

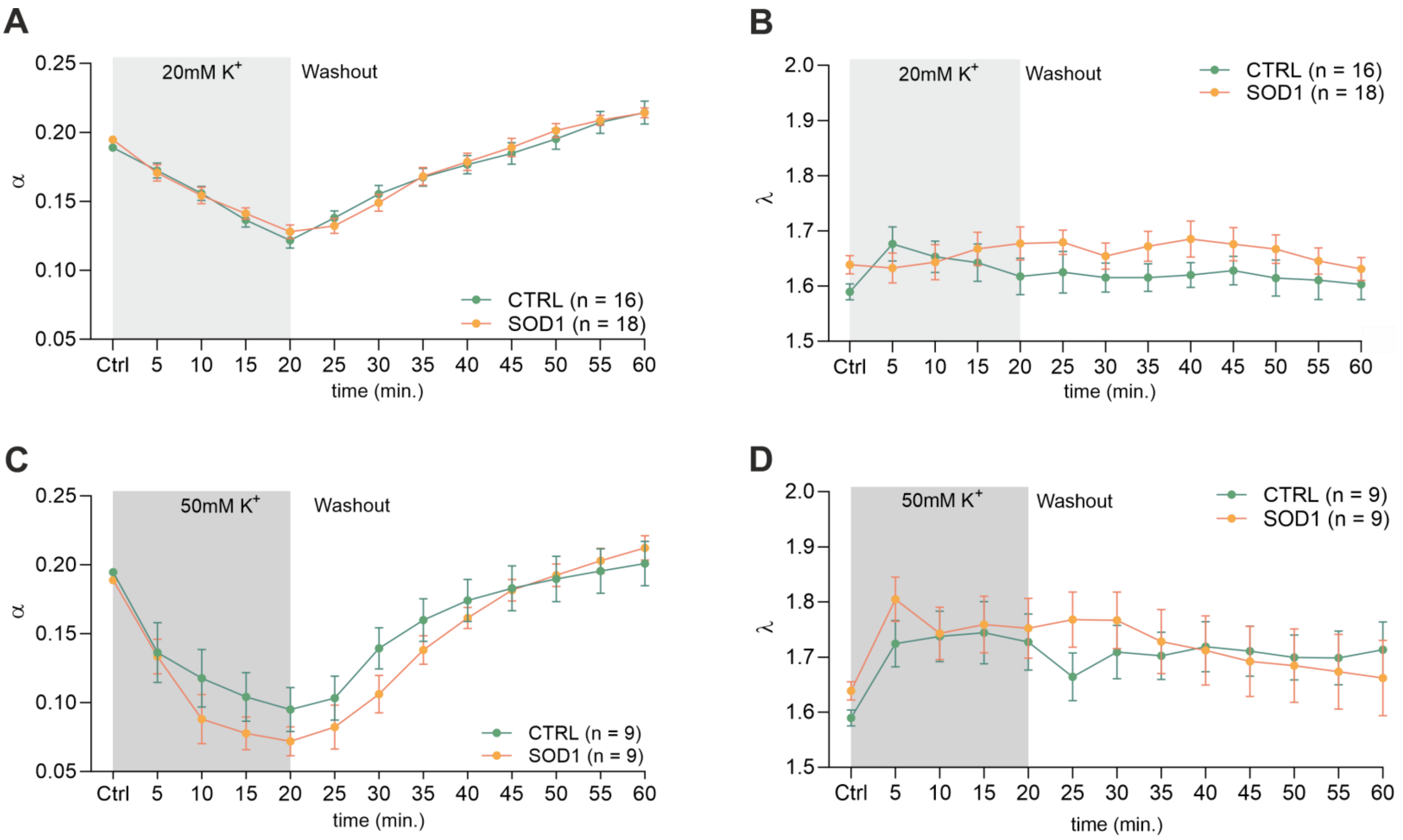
A
0.25
0.20
0.15
0.10
0.05
α
20mM K⁺
Washout
CTRL (n = 16)
SOD1 (n = 18)
Ctrl 5 10 15 20 25 30 35 40 45 50 55 60
time (min.)
B
2.0
1.9
1.8
1.7
1.6
1.5
λ
20mM K⁺
Washout
CTRL (n = 16)
SOD1 (n = 18)
Ctrl 5 10 15 20 25 30 35 40 45 50 55 60
time (min.)
C
0.25
0.20
0.15
0.10
0.05
α
50mM K⁺
Washout
CTRL (n = 9)
SOD1 (n = 9)
Ctrl 5 10 15 20 25 30 35 40 45 50 55 60
time (min.)
D
2.0
1.9
1.8
1.7
1.6
1.5
λ
50mM K⁺
Washout
CTRL (n = 9)
SOD1 (n = 9)
Ctrl 5 10 15 20 25 30 35 40 45 50 55 60
time (min.)

Figure 5.TIF

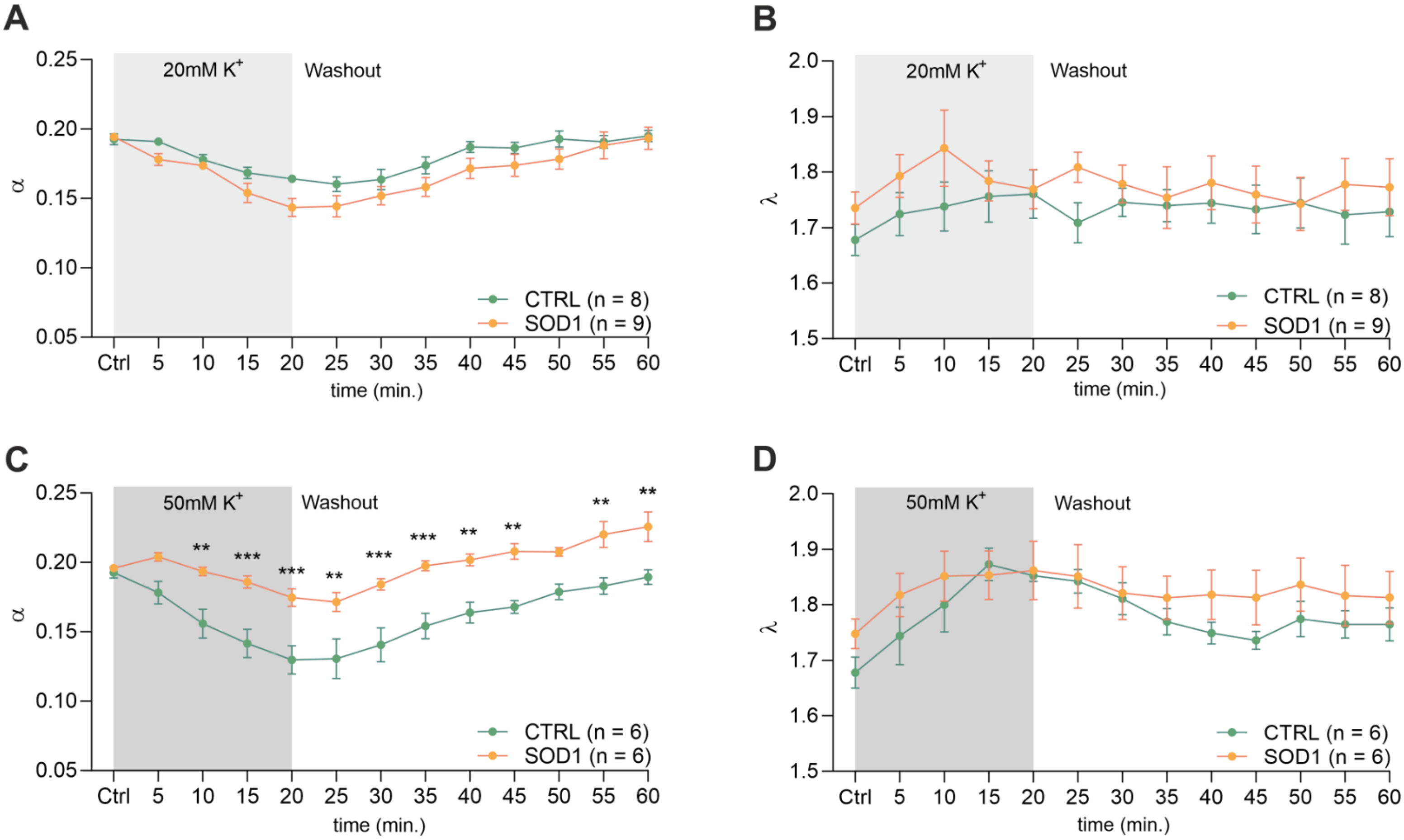
A
0.25
0.20
0.15
0.10
0.05
α
20mM K$^+$
Washout
CTRL (n = 8)
SOD1 (n = 9)
Ctrl 5 10 15 20 25 30 35 40 45 50 55 60
time (min.)
B
2.0
1.9
1.8
1.7
1.6
1.5
λ
20mM K$^+$
Washout
CTRL (n = 8)
SOD1 (n = 9)
Ctrl 5 10 15 20 25 30 35 40 45 50 55 60
time (min.)
C
0.25
0.20
0.15
0.10
0.05
α
50mM K$^+$
Washout
** *** *** ** *** *** ** ** ** **
CTRL (n = 6)
SOD1 (n = 6)
Ctrl 5 10 15 20 25 30 35 40 45 50 55 60
time (min.)
D
2.0
1.9
1.8
1.7
1.6
1.5
λ
50mM K$^+$
Washout
CTRL (n = 6)
SOD1 (n = 6)
Ctrl 5 10 15 20 25 30 35 40 45 50 55 60
time (min.)

Figure 6.TIF

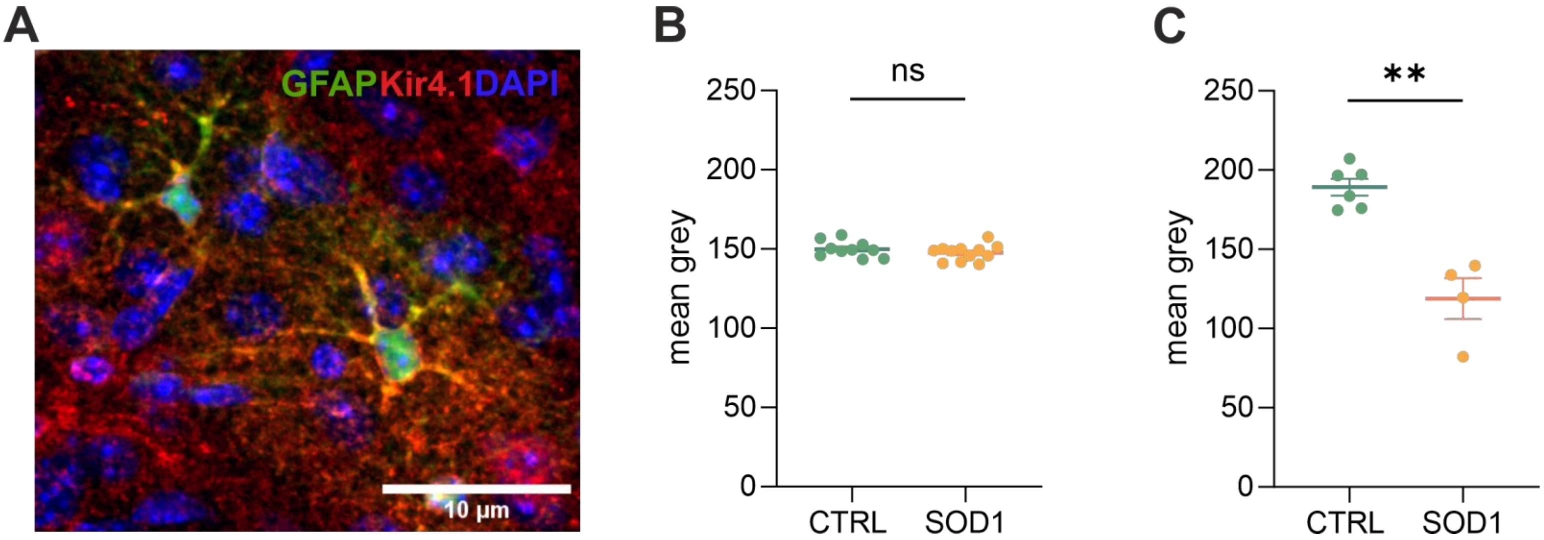
A
GFAP
Kir4.1
DAPI
10 µm
B
ns
250
200
150
100
50
0
mean grey
CTRL
SOD1
C
**
250
200
150
100
50
0
mean grey
CTRL
SOD1

Figure 7.TIF

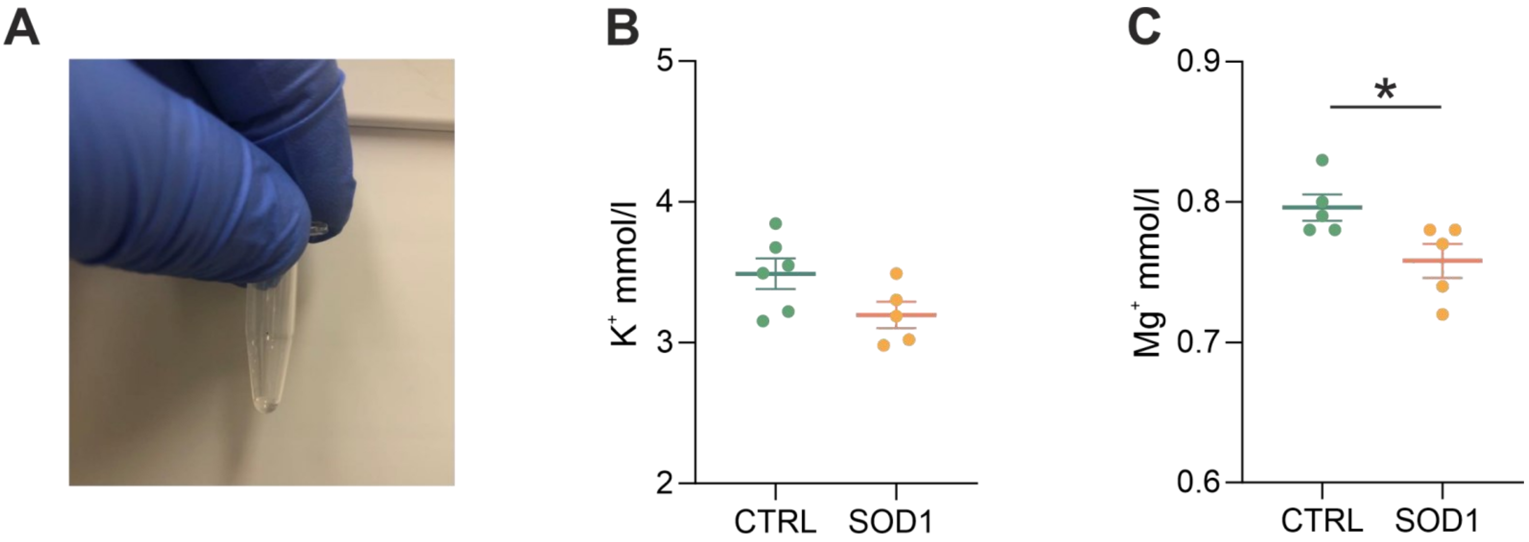

frontiers in Aging Neuroscience

ORIGINAL RESEARCH
published: 27 January 2022
doi: 10.3389/fnagi.2021.783120

Compromised Astrocyte Swelling/Volume Regulation in the Hippocampus of the Triple Transgenic Mouse Model of Alzheimer's Disease

Jana Tureckova[1*†], *Monika Kamenicka*[1,2†], *Denisa Kolenicova*[1,2], *Tereza Filipi*[1,2], *Zuzana Hermanova*[1,2], *Jan Kriska*[1], *Lenka Meszarosova*[1], *Barbora Pukajova*[1], *Lukas Valihrach*[3], *Peter Androvic*[3], *Daniel Zucha*[3,4], *Martina Chmelova*[1,2], *Lydia Vargova*[1,2] and *Miroslava Anderova*[1,2]

[1] Department of Cellular Neurophysiology, Institute of Experimental Medicine, Czech Academy of Sciences, Prague, Czechia, [2] Second Faculty of Medicine, Charles University, Prague, Czechia, [3] Laboratory of Gene Expression, Institute of Biotechnology, Czech Academy of Sciences, Vestec, Czechia, [4] Faculty of Chemical Technology, University of Chemistry and Technology, Prague, Czechia

OPEN ACCESS

Edited by:
Ana Isabel Rodríguez Pérez,
University of Santiago de Compostela, Spain

Reviewed by:
Carmen Vivar,
Centro de Investigación y de Estudios Avanzados del Instituto Politécnico Nacional de México (CINVESTAV), Mexico
Alexander A. Mongin,
Albany Medical College, United States

**Correspondence:*
Jana Tureckova
jana.tureckova@iem.cas.cz

† These authors have contributed equally to this work and share first authorship

Specialty section:
This article was submitted to Alzheimer's Disease and Related Dementias,
a section of the journal Frontiers in Aging Neuroscience

Received: 25 September 2021
Accepted: 27 December 2021
Published: 27 January 2022

Citation:
Tureckova J, Kamenicka M, Kolenicova D, Filipi T, Hermanova Z, Kriska J, Meszarosova L, Pukajova B, Valihrach L, Androvic P, Zucha D, Chmelova M, Vargova L and Anderova M (2022) Compromised Astrocyte Swelling/Volume Regulation in the Hippocampus of the Triple Transgenic Mouse Model of Alzheimer's Disease.
Front. Aging Neurosci. 13:783120.
doi: 10.3389/fnagi.2021.783120

In this study, we aimed to disclose the impact of amyloid-β toxicity and tau pathology on astrocyte swelling, their volume recovery and extracellular space (ECS) diffusion parameters, namely volume fraction (α) and tortuosity (λ), in a triple transgenic mouse model of Alzheimer's disease (3xTg-AD). Astrocyte volume changes, which reflect astrocyte ability to take up ions/neurotransmitters, were quantified during and after exposure to hypo-osmotic stress, or hyperkalemia in acute hippocampal slices, and were correlated with alterations in ECS diffusion parameters. Astrocyte volume and ECS diffusion parameters were monitored during physiological aging (controls) and during AD progression in 3-, 9-, 12- and 18-month-old mice. In the hippocampus of controls α gradually declined with age, while it remained unaffected in 3xTg-AD mice during the entire time course. Moreover, age-related increases in λ occurred much earlier in 3xTg-AD animals than in controls. In 3xTg-AD mice changes in α induced by hypo-osmotic stress or hyperkalemia were comparable to those observed in controls, however, AD progression affected α recovery following exposure to both. Compared to controls, a smaller astrocyte swelling was detected in 3xTg-AD mice only during hyperkalemia. Since we observed a large variance in astrocyte swelling/volume regulation, we divided them into high- (HRA) and low-responding astrocytes (LRA). In response to hyperkalemia, the incidence of LRA was higher in 3xTg-AD mice than in controls, which may also reflect compromised K^+ and neurotransmitter uptake. Furthermore, we performed single-cell RT-qPCR to identify possible age-related alterations in astrocytic gene expression profiles. Already in 3-month-old 3xTg-AD mice, we detected a downregulation of genes affecting the ion/neurotransmitter uptake and cell volume regulation, namely genes of glutamate transporters, α2β2 subunit of Na^+/K^+-ATPase, connexin 30 or Kir4.1 channel. In conclusion, the aged hippocampus of 3xTg-AD mice displays an enlarged ECS volume fraction and an increased number of obstacles, which emerge earlier than in physiological aging. Both these changes may strongly affect intercellular communication and influence astrocyte ionic/neurotransmitter uptake, which becomes impaired during aging and this phenomenon is manifested earlier in 3xTg-AD mice. The increased incidence of astrocytes with limited ability to take up ions/neurotransmitters may further add to a cytotoxic environment.

Keywords: astrocytes, ECS diffusion, volume changes, astrocyte heterogeneity, ion uptake, Alzheimer's disease

INTRODUCTION

Alzheimer's disease (AD) is a chronic progressive neurodegenerative disorder which affects 35.6 million people worldwide, and the numbers are expected to double every twenty years (Prince et al., 2013). The neurodegeneration occurs in the prefrontal cortex, entorhinal cortex and hippocampus, which are brain structures related to learning and memory, and which are further linked to the limbic system associated with cognitive and emotional processes (Minati et al., 2009; Kulijewicz-Nawrot et al., 2012). Therefore, AD mainly affects the memory and cognitive functions and, in its later stage, results in dementia. Although the disease has been intensively studied for more than a hundred years and several processes underlying neuronal loss have been proposed during this period, the overall understanding of the AD pathology remains incomplete. The most frequently declared causes of AD comprise neurodegeneration driven by amyloid-β (Aβ) toxicity and tau pathology, synaptic dysfunction as well as the loss of synaptic density, glutamate excitotoxicity, and oxidative stress (Smith et al., 2000; Hardy and Selkoe, 2002; Ingelsson et al., 2004; Walton and Dodd, 2007; Kriska et al., 2021). However, the pathological processes behind AD not only cause neuronal death, but also involve functional changes in other cell types, such as glia or pericytes, alterations in inter-cellular communication, changes in the composition of perineural networks, and vascular system disruption (De Strooper and Karran, 2016; Goetzl and Miller, 2017).

Astrocytes represent multifunctional cells, which play an essential role in brain development, metabolism, in the control of the central nervous system (CNS) microenvironment, in modulating synaptic transmission and neurotransmitter release, and they also perform an important vascular function. During the progression of AD, astrocytes undergo morphological and functional changes and, ultimately, they become reactive (Kulijewicz-Nawrot et al., 2012, 2013; Acosta et al., 2017; Assefa et al., 2018). Impaired astrocytic functioning leads to altered glutamate (Glu) and ion homeostasis, as well as an increased release of Glu, γ-aminobutyric acid (GABA), cytokines and inflammatory mediators (Hynd et al., 2004; Ben Haim et al., 2015). Moreover, reactive astrocytes together with microglia, associate with Aβ deposits and are involved in neuritic plaque formation (Itagaki et al., 1989; Serrano-Pozo et al., 2013).

Here we focus on the AD related changes in the astrocytic uptake of ions and neurotransmitters from the extracellular space (ECS), which maintains their optimal concentration for the effective functioning of synaptic transmission. The intracellular accumulation of ions is followed by the entry of water, which leads to a transient increase in cell volume. In a healthy adult brain, astrocyte swelling triggers compensatory mechanisms that lead to an alleged regulatory volume decrease (RVD) (Okada et al., 2009; Wilson and Mongin, 2018). However, the ability of astrocytes to swell, as well as to regulate their volume, declines in the healthy aged brain. Under pathological conditions, in which the concentration of ions in the ECS increases significantly (Pasantes-Morales and Vazquez-Juarez, 2012), the compromised uptake of ions/neurotransmitters in astrocytes and/or loss of the ability to regulate their volume observed during aging may significantly add to the progression of AD. Such changes in astrocyte volume and morphology, together with the composition and structure of the extracellular matrix (ECM), affect the diffusion parameters of ECS. As the composition of ECS is crucial in the process of waste clearance, it is also feasible that changes in the ECS diffusivity contribute to the pathology of AD, due to the insufficient Aβ removal (Nedergaard and Goldman, 2020). Moreover, recent studies have shown that some ECM molecules can actively participate in the pathogenesis of the AD development, and promote an intracellular accumulation of protein aggregates such as Aβ, tau and α-synuclein (Holmes et al., 2013).

The main goal of this study was to assess astrocyte ability to control the ion or neurotransmitter uptake in the triple transgenic model of AD (3xTg-AD) containing three mutations associated with familial AD. To achieve this objective, we employed three-dimensional (3D) confocal morphometry, a method which enables the study of single-cell morphology changes during exposure to pathological stimuli, namely hypo-osmotic stress, or high K^+ concentrations (Chvatal et al., 2007a,b). Cell volume changes mirror alterations in the expression/function of the different ion channels and transporters responsible for the uptake of ions and neurotransmitters, as well as for RVD. To identify such changes in the expression of astrocytic transport proteins, we employed a single-cell reverse transcription quantitative polymerase chain reaction (sc RT-qPCR). Finally, these observations were correlated with alterations in the diffusion parameters of ECS, reflecting both changes in cellular volume and ECS structure. All studied parameters were monitored during physiological aging and during the progression of AD.

MATERIALS AND METHODS

Animals

Experimental animals were generated by crossbreeding of the triple transgenic model of AD, containing three mutations associated with familial AD (APP Swedish, MAPT P301L, and PSEN1 M146V) (Oddo et al., 2003) and GFAP/EGFP strain (Nolte et al., 2001). These hybrids enable the visualization of astrocytes for the use of morphological studies due to the enhanced green fluorescent protein (EGFP), expressed under the control of the human glial fibrillary acidic protein (GFAP) promoter. The experiments were performed on GFAP/EGFP mice (FVB/NJ, controls) and GFAP/EGFP x 3xTg-AD mice (C57Bl/6; hereinafter referred to as 3xTg-AD) at the ages of 3, 9, 12, and 18 months (3M, 9M, 12M, 18M).

All procedures involving the use of laboratory animals were performed in accordance with the European Communities Council Directive November 24, 1986 (86/609/EEC) and animal care guidelines approved by the Institute of Experimental Medicine ASCR Animal Care Committee, approval number 95/2015, 49/2019. All efforts were made to minimize both the suffering and the number of animals used. The mice were kept on a 12-h light/dark cycle with access to food and water *ad libitum*.

Solutions

The compositions of brain isolation solution and artificial cerebrospinal fluid (aCSF), solution modeling hypo-osmotic stress ($aCSF_{H-100}$), and solution modeling hyperkalemia ($aCSF_{K+}$) are listed in **Table 1**. All solutions were equilibrated with 95% O_2 and 5% CO_2 (Carbogen, Siad, Branany, Czechia) to a final pH of 7.4, and osmolality of ∼300 mOsmol/kg was measured using a vapor pressure osmometer (Vapro 5520, Wescor, Logan, UT, United States).

Preparation of Acute Brain Slices

The experimental mice were deeply anesthetized with 1% pentobarbital (100mg/kg; i.p.), transcardially perfused with cold (4 – 8°C) isolation solution (**Table 1**), and decapitated. The brains were dissected out and coronal 300-μm-thick slices were cut using a vibrating microtome (Leica Biosystems, Buffalo Grove, IL, United States). The slices were incubated for 40 min at 34°C in the isolation solution, and then transferred to aCSF (**Table 1**) in which they were kept throughout the experiment at room temperature. To minimize the damage to the nervous tissue isolated from aged mice, N-methyl-D-glucamine-based isolation solution (**Table 1**) was always used during slice preparation and incubation after the brain cutting, as described for aged mice/rats in the study by Ting et al. (2014).

TABLE 1 | Composition of the solutions.

Compounds	Isolation solution (mM)	aCSF (mM)	$aCSF_{H-100}$ (mM)	$aCSF_{K+}$ (mM)
NaCl	-	122	67	75
NMDG	110	-	-	-
KCl	2.5	3	3	50
$NaHCO_3$	24.5	28	28	28
$NaHPO_4$	1.25	1.25	1.25	1.25
Glucose	20	10	10	10
$CaCl_2$	0.5	1.5	1.5	1.5
$MgCl_2$	7	1.3	1.3	1.3
Osmolality (mOsmol/kg)	300 ± 10	300 ± 10	200 ± 10	300 ± 10

Key: NMDG, N-methyl-D-glucamine; aCSF, artificial cerebrospinal fluid; $aCSF_{H-100}$, hypo-osmotic solution; $aCSF_{K+}$, solution with elevated potassium concentration.

Real-Time Iontophoretic Method

The real-time iontophoretic (RTI) method was used to define the ECS diffusion parameters: ECS volume fraction (α), tortuosity (λ), and nonspecific uptake (k') (Nicholson and Phillips, 1981; Sykova and Nicholson, 2008). ECS volume fraction is the space available for diffusion and is defined as the ratio of the volume of the ECS to total tissue volume in a representative volume of brain tissue (α = ECS/total tissue volume). Tortuosity is defined as square root of the ratio of the free diffusion coefficient in a medium with free diffusion, and the apparent diffusion coefficient in the brain tissue. Tortuosity reflects the compromised extracellular diffusion in the tissue in comparison with a free diffusion medium due to the presence of diffusion barriers created, for example, by cell processes, ECM molecules, or "dead spaces" (Hrabetova et al., 2003; Thorne and Nicholson, 2006; Sykova and Nicholson, 2008). Nonspecific uptake represents the loss of diffusing ions/molecules from the ECS into cells or capillaries.

In brief, an extracellular marker, tetramethylammonium ions (TMA$^+$, MW = 74.1), to which cell membranes are relatively impermeable, are introduced into the tissue through the iontophoretic microelectrode, and imitate the extracellular diffusion of small ions and molecules. The time-dependent changes in the concentration of TMA$^+$ in the ECS are determined by ion-selective microelectrodes (ISMs). Double-barrelled TMA$^+$-ISMs were prepared so that the tip of the ion-sensitive barrel was filled with an ion-exchanger IE190 (WPI, Inc., Sarasota, FL, United States, RRID:SCR_008593); the rest of the barrel was backfilled with 100 mM TMA$^+$. The reference channel contained 150 mM NaCl. Prior to the experiments, TMA$^+$-ISMs micropipettes were calibrated using the fixed-interference method in a series of five different concentrations of TMA$^+$ (mM): 0.1, 0.3, 1.0, 3.0, 10.0 in a background of 150 mM NaCl and 3 mM KCl. The signal was recorded by a locally constructed differential amplifier (Voipio et al., 1994), which subtracts the signals from the reference and ion-selective barrels. Calibration voltages were fitted to the Nikolsky equation, to determine the slope and the interference of each ISM (Nicholson, 1993).

The TMA$^+$-ISM and an iontophoretic micropipette, backfilled with 100 mM TMA$^+$ chloride, were glued together using dental cement with a tip separation of 90–150 μm. The 20 nA bias current was applied continuously (Single Channel Iontophoresis Generator ION-100, Dagan Corporation, Minneapolis, MN, United States) to maintain a constant electrode transport number. The diffusion curves were generated by a current step to 200 nA of 24 s duration (Master 8, A.M.P.I, Jerusalem, Israel) and captured on a digital oscilloscope (NIC Nicolet Dual Channel Digital Oscilloscope 3091). In order to calibrate the electrode array before tissue measurements, the diffusion curves were recorded in 0.3% agar gel (Sigma Aldrich, Germany), dissolved in a solution of 150 mM NaCl, 3 mM KCl and 1 mM TMA^+. The curves were then analyzed by a non-linear curve fitting simplex algorithm, operating on a modified diffusion equation, using the VOLTORO program (kindly provided by C. Nicholson, New York University School of Medicine, United States). Calibration determines the values of the free diffusion coefficient of TMA^+ (D), the distance between electrodes (r) and the transport number (n_t), a dimensionless parameter that denotes the fraction of the applied current that carries the TMA^+ out of the micropipette during an iontophoretic pulse. With the known D, r and n_t-values, the parameters α (volume fraction), λ (tortuosity) and k' (non-specific uptake) can be determined.

Data are presented as the mean ± SEM. Statistical analyses for diffusion measurements were performed by Student's *t*-test with Benjamini-Hochberg *post hoc* test to control the false discovery rate when conducting multiple comparisons (age-related differences within control or 3xTg-AD mice) or two-way ANOVA test with Tukey *post hoc* test (differences between control and age-matched 3xTg-AD mice). Differences between the groups were considered statistically significant when $p < 0.05$, very significant when $p < 0.01$, and extremely significant when $p < 0.001$.

Cell Volume Measurement and Quantification

Time-dependent changes in astrocyte volume were studied using 3D - confocal morphometry in the CA1 region of hippocampal slices. The method was previously described by Chvatal et al. (2007a,b). During all the experiments, brain slices were placed into the recording chamber and fixed with a U-shaped platinum wire with a grid of nylon threads. The recording chamber was continuously perfused with aCSF or solutions modeling hypo-osmotic stress ($aCSF_{H-100}$) or hyperkalemia ($aCSF_{K+}$). Cell images for the volume quantification were taken every 5 min during the 20-min exposure to $aCSF_{H-100}$ or $aCSF_{K+}$ and every ten minutes during the following 40-min washout. The cells were recorded as a set of two-dimensional (2D) sectional images, with a resolution of 1024 × 1024 pixels using FV1200MPE confocal microscope with 60 × LUMPLFLN water objective (Olympus, Shinjuku, Japan). EGFP was excited by an Ar laser at 488 nm, and the emitted signal was recorded over the range of 488 nm using a DM405/488 filter. Each 3D image of the cell was sectioned into 65 - 85 consecutive 2D images at a uniform spacing of 1 μm. To avoid the inclusion of damaged cells into the experiments, especially those with partly damaged processes in the vicinity of the slice surface, we always chose cells with processes emerging 20 – 30 μm beneath the surface were always chosen, as described earlier in our previous work (Benesova et al., 2009).

Image processing and morphometric measurements were performed using the program Cell Analyst, developed at the Department of Cellular Neurophysiology, Institute of Experimental Medicine, Prague, Czechia (Chvatal et al., 2007a,b). For each time point, 4 - 5 mice were used, and 2 - 3 slices were prepared from the hippocampus of both hemispheres. These half-slices were used for quantification of the volume of 1 or 2 EGFP-positive cells. Changes in the total astrocyte volume are presented as the mean ± SEM. Statistical significance was determined in the time course of astrocyte volume changes during aging by two-way ANOVA with Tukey's *post hoc* test. Differences between the groups were considered statistically significant when $p < 0.05$, very significant when $p < 0.01$, and extremely significant when $p < 0.001$.

Immunohistochemistry

The mice were deeply anesthetized with pentobarbital (100 mg/kg, i.p.), and transcardially perfused with 20 ml of saline with heparin (2500 IU/100 mL; Zentiva, Prague, Czechia) followed by 20 ml of 4% paraformaldehyde. The brains were dissected, postfixed in 4% paraformaldehyde overnight, and placed stepwise in solutions with gradually increasing sucrose concentrations (10, 20, and 30%) for cryoprotection. Coronal slices (30 μm) were prepared using Hyrax C50 cryostat (Zeiss, Gottingen, Germany). The slices were incubated in a blocking solution containing 5% ChemiBLOCKER (Merck, Darmstadt, Germany) and 0.5% Triton X-100 (Merck, Darmstadt, Germany) in phosphate buffer saline (PBS) for 1 h. They were then incubated overnight at 4°C with primary antibodies diluted in a blocking solution, followed by a 2-h incubation with species-specific secondary antibodies diluted in blocking solution at room temperature. Primary antibody against Amyloid beta (1:1000, EMD Millipore; Merck, Darmstadt, Germany) was used. Corresponding secondary antibody (goat anti-rabbit IgG, goat anti-mouse IgG, conjugated with Alexa-Fluor 594; Thermo Fisher Scientific; Waltham, MA, United States) was diluted to 1:200. To visualize the cell nuclei, the slices were incubated with 300 nM 4^r, 6-diamidino-2-phenylindole (DAPI) in PBS for 5 min at room temperature. After immunostaining, the slices were mounted onto microscope slides using Aqua-Poly/Mount (Polysciences Inc, Eppelheim, Germany).

Gene Expression Profiling

Preparation of Single Cell Suspension From the Hippocampal CA1 Region

The mice aged 3, 9, 12, and 18 M were anesthetized with sodium-pentobarbital (100 mg/kg, i.p.), and perfused transcardially with cold (4 – 8 °C) isolation buffer containing (in mM) NaCl 136.0, KCl 5.4, Hepes 10.0, glucose 5.5, osmolality 290 ± 3 mOsmol/kg. The hippocampus was removed and used for the preparation of cell suspension using a papain dissociation kit (Worthington, Lakewood, NJ, United States). The dissociated cells were layered on top of 5 ml of Ovomucoid inhibitor solution (Worthington, Lakewood, NJ, United States) and subsequently harvested by centrifugation (140 × *g* for 6 min). This method routinely yielded $\sim 2 \times 10^6$ cells per mouse brain. Cell aggregates were removed by filtering with 70 μm cell strainers (Becton Dickinson, NJ, United States), and the cells were kept on ice until sorting.

Collection of Single Enhanced Green Fluorescent Protein-Positive Cells

The astrocytes were collected using flow cytometry (fluorescence-activated cell sorting [FACS]; BD Influx, San Jose, CA, United States). FACS was calibrated manually to deposit single cells in the center of each collection tube. Hoechst 33258 (Life Technologies, Carlsbad, CA, United States) was added to the suspension of cells to check cell viability. Single cells were sorted into 96-well plates (Life Technologies), each well contained 5 mL of nuclease-free water with bovine serum albumin (1 mg/ml, Fermentas, Rockford, IL, United States) and RNaseOut 20 U (Life Technologies). The plates were then placed on a precooled rack. The astrocytes were collected based on their positivity for EGFP and their viability. The plates with collected cells were immediately frozen at 80°C and stored until the analysis.

Single-Cell Gene Expression Profiling

The collected single cells were analyzed by sc RT-qPCR. In total, the expression of 96 genes was determined (**Supplementary Table 1**). Primers were designed using PrimerBLAST. When possible, each primer pair was separated by at least one intron on the corresponding genomic DNA. For each assay, specificity was tested by melt curve analysis and gel electrophoresis. The effectivity of each assay was determined using a standard dilution over 6 orders of magnitude. In RT-qPCR analysis, samples were reverse-transcribed into cDNA using SuperScript III (ThermoFisher Scientific). The reverse transcription was performed using the standard protocol recommended by the manufacturer, except with the total volume of 10 μl, equimolar mix of oligo-dT and random hexamers (50 μM) and a reduced concentration of SuperScript III enzyme (50 U), was used. To monitor the risk of inhibition, RNA TATAA Universal RNA Spike II was added into each reaction based on the manufacturer's instructions (TATAA Biocenter, Sweden). Five microliters of non-diluted cDNA were further pre-amplified using a mix of all primers. Preamplified cDNA was diluted 4 times and analyzed using BioMark instrument (Fluidigm, United States). A detailed description of each procedure can be found elsewhere (Rusnakova et al., 2013; Valny et al., 2018).

Data Processing

In total, 461 cells from 37 mice were analyzed (3M: 4 controls, 4 3xTg-AD, 9M: 4 controls, 5 3xTg-AD, 12M: 6 controls, 5 3xTg-AD, 18M: 4 controls, 5 3xTg-AD). RT-qPCR data were pre-processed in Fluidigm Real-Time PCR Analysis software (4.1.2, Fluidigm, United States) and analyzed with GenEx software (Ver. 6.1.1.550, MultiD, Sweden). C_q-values measured from amplifications that generated melting curves with aberrant T_m were removed, as well as C_q-values larger than 28. All missing data, for each gene separately, were then replaced with the highest C_q +2 (25% of the lowest measurable concentration). C_q-values with non-missing data were transformed into relative quantities (scaled to the sample with the lowest expression) and converted into log 2 scale. The data are presented as the mean ± SEM. Statistical analyses of the differences in gene expression among groups were performed using ANOVA for multiple comparisons, with Tukey's *post hoc* test, or Student's *t*-test when appropriate. Differences between the groups were considered statistically significant when $p < 0.05$, very significant when $p < 0.01$, and extremely significant when $p < 0.001$.

RESULTS

We hypothesized that morphological changes of individual cellular elements or changes in the composition of the ECM during AD, may affect the volume and diffusion properties of ECS. To test this hypothesis, we performed measurements of the extracellular diffusion parameters in the CA1 region of hippocampal slices by the RTI method during the exposure to the pathological models of hypo-osmotic stress and hyperkalemia. Additionally, the astrocyte functional changes, such as the uptake of ions from ECS and the ability to regulate their volume, were tested using the 3D confocal morphometry method. Finally, we used sc RT-qPCR to assess expression changes of genes which are responsible for astrocytic key homeostatic functions. All experiments were performed in 3-, 9-, 12- and 18M controls and 3xTg-AD mice. Since no sex differences were noted, data from males and females were pooled.

Validation of the Triple Transgenic Mouse Model of Alzheimer's Disease

For the purpose of the morphological study, the 3xTg-AD mice (Oddo et al., 2003) were crossbred with GFAP/EGFP mice (Nolte et al., 2001). The hybrid mice retained the 3xTg-AD phenotype and in addition, they expressed EGFP under the GFAP promoter, allowing the visualization of astrocytes. Immunohistochemical staining of Aβ confirmed its expression in the motor cortex and hippocampus, similarly to the original model (**Figure 1A**). In the hippocampal CA1 region, the intracellular expression in pyramidal neurons was already observed in the 3M mice, while the external presence of Aβ plaques was not evident until 18 months of age (**Figure 1B**). Single-cell RT-qPCR verified the expression of all three mutations (AppSwe, TauP301L, Psen1M146) in EGFP-positive cells (**Figure 1C**).

Diffusion Parameters in the Hippocampus of Triple Transgenic Mouse Model of Alzheimer's Disease

In this study, we identified a significant continuous decrease in α during physiological aging in the CA1 region of the hippocampus (3M - ∼0.212; 9M - ∼0.188; 12M - ∼0.169; 18M - ∼0.123). In contrast, we detected no age-related decrease in α in 3xTg-AD mice (3M - ∼0.212; 9M - ∼0.188; 12M - ∼0.199; 18M - ∼0.197) (**Figure 2A**). The values of α in 3xTg-AD mice and their age-matched controls began to differ significantly at 12 months of age; this difference was extremely significant at 18 months (**Figure 2C**).

In the CA1 region of the hippocampus of the control mice, we observed an increasing tendency in the λ values, which were significantly higher in 12M and 18M mice than in 3M mice. In 18M mice, an additional increase in λ was detected; the value was significantly higher in comparison with all other age groups (3M - ∼1.491; 9M - ∼1.543; 12M - ∼1.560 ± 0.017; 18M - ∼1.695 ± 0.016). The data of the 3xTg-AD mice also showed that λ increases over age (**Figure 2B**). This increase was faster than in the control animals, and most pronounced in 12M and 18M mice (3M - ∼1.511; 9M - ∼1.562; 12M - ∼1.650; 18M - ∼1.736). The values of λ in 12M mice were significantly higher in the 3xTg-AD mice than in the age-matched controls, but the difference disappeared in 18M mice (**Figure 2C**).

In conclusion, physiological aging was accompanied by a decrease in ECS volume fraction, while this tendency was completely lost during AD progression. However, an increase in the number of obstacles observed in AD progression occurred earlier than in physiological aging.

Changes in the Diffusion Parameters of Extracellular Space Induced by Hypo-Osmotic Stress or Hyperkalemia

To further disclose the differences between 3xTg-AD mice and controls, experimental cell swelling in brain slices was evoked by exposure to hypo-osmotic stress ($aCSF_{H-100}$) or severe hyperkalemia ($aCSF_{K+}$). The ECS diffusion parameters were determined during basal conditions and during a 20-min perfusion with $aCSF_{H-100}$ or $aCSF_{K+}$, followed by a 40-min application of aCSF (further termed washout). As the basal values of α and λ varied, we evaluated both the absolute and relative changes of the ECS parameters. To estimate the relative changes, the control values were set to 100%, and the relative changes were calculated.

In all ages and groups, the application of $aCSF_{H-100}$ induced a significant decrease in α with a complete or partial recovery during washout (**Figure 3**). A significant difference between the control and 3xTg-AD mice in the minimal α values during the application (20 min after the induction of hypo-osmotic stress), was observed only at 3 months of age, where the values of α were lower in the control mice (~0.072) than in 3xTg-AD mice (~0.116). Despite the higher basal α values in 3xTg-AD mice in 18M mice, the minimal values at 20 minutes of application did not differ between the control and 3xTg-AD mice. During the washout in the control animals, we detected a complete recovery of α in age of 3-, 9-, and 12 months, and partial recovery in the oldest, 18M group. In 3xTg-AD mice, α fully recovered to basal values in 3M and 9M animals; only partial recovery was detected in 12- and 18M-old mice. To further analyze the ECS volume changes during the washout period, they were expressed as a percentage of volume increase/decrease in relation to the value of α reached in the 20th min of application, which was set as 0%. This analysis showed a significant difference between the control and 3xTg-AD animals in the 20th min of washout in 9M mice and the 40^{th} minute of washout in 12M mice (**Figure 3**). These results already indicate a slower and compromised recovery in the 3xTg-AD mice in 9M- and 12M-age groups. Tortuosity increased during the application of $aCSF_{H-100}$ and returned to the basal values during washout in all the groups. The only difference between the control and 3xTg-AD mice was observed at 12M, where λ values were higher in the 3xTg-AD mice than in controls during almost the entire experiment due to a distinctly larger basal value (**Supplementary Figure 1A**). Relative values of volume fraction and tortuosity did not show any significant changes between the control and 3xTg-AD mice (**Supplementary Figure 2**).

In summary, changes in ECS volume fraction and tortuosity evoked by hypo-osmotic stress were comparable between the 3xTg-AD mice and their age-matched controls, however compromised and slower recovery of ECS volume fraction in the 3xTg-AD mice was detected in 9- and 12M mice.

The application of the $aCSF_{K+}$ solution evoked a significant decrease of α in all the experimental groups, followed by a partial recovery towards basal values during washout with aCSF solution, apart from 18M control mice, where no recovery was detected (**Figure 4**). Significant differences between the control and 3xTg-AD mice were only observed at 18M of age, where α values in the 3xTg-AD animals where higher than those in the controls before the application and during washout but the minimal values reached during the application did not differ. The recovery analysis showed a significant difference between the control and 3xTg-AD animals in the 20th and 40th min of washout in 18M-old mice (**Figure 4**). While the values of α in the oldest control group did not recover at all, partial recovery was still detected in the 3xTg-AD mice, presumably due to the higher initial value of α. Severe hyperkalemia evoked an increase in λ in all experimental groups, followed by a recovery to basal values during washout. Similarly, to $aCSF_{H-100}$ application, we only found differences between the control and 3xTg-AD mice at 12 months of age, where λ values in the 3xTg-AD mice during the basal conditions, $aCSF_{K+}$ application and washout were higher than those in the controls (**Supplementary Figure 1B**). The relative values of volume fraction and tortuosity did not show any significant differences between the control and 3xTg-AD mice (**Supplementary Figure 3**). The complete data are summarized in **Supplementary Tables 2, 3**.

In summary, comparable changes in ECS volume fraction and tortuosity evoked by hyperkalemia, were observed between the 3xTg-AD mice and their age-matched controls within 3 – 12M of age. However, in 18M mice, due to a higher initial ECS volume fraction a better recovery in the 3xTg-AD than in control mice was detected.

Astrocyte Swelling Induced by Hypo-Osmotic Stress or High Extracellular K^+ Concentration in Triple Transgenic Mouse Model of Alzheimer's Disease

Swelling of astrocytes and their ability of volume regulation were tested in acute brain slices from 3M, 9M, 12M, and 18M mice exposed to $aCSF_{H-100}$ or $aCSF_{K+}$. The 20-min exposure was followed by a 40-min washout. Changes in the total astrocytic volume (ΔV_c) were recorded every 5 min during the $aCSF_{H-100}$ or $aCSF_{K+}$ application and every 20 min during the washout. The astrocyte volume at $t = 0$ was set to 100% and the astrocytic swelling was expressed relative to this baseline as a percentual increase/decrease.

In our previous study (Kolenicova et al., 2020) we showed that the volume of astrocytes induced by hyperkalemia varies with age. While in 3- and 12M animals astrocytes swelled markedly (up to a maximum of ~170% in 3M), in 9- and 18M mice, the swelling was lower (maximum ~140 % in 18M). These

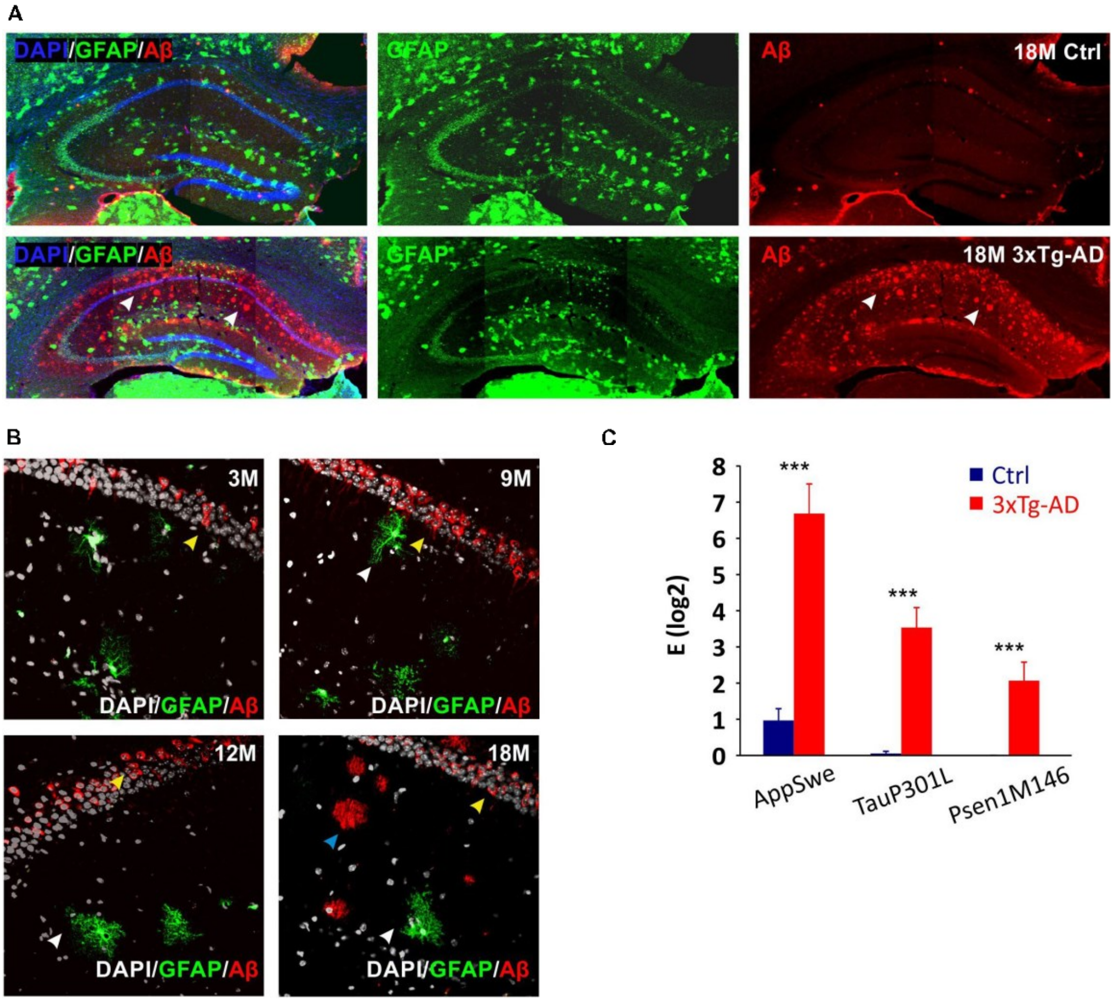

FIGURE 1 | Confirmation of the 3xTg-AD phenotype in hybrids generated by crossbreeding with GFAP/EGFP mice. (A) Overview images of amyloid-β (Aβ) expression in hippocampus of 18M-old controls and 3xTg-AD mice. White arrows point to the expression of amyloid plaques in the CA1 region of the hippocampus in a transgenic model of Alzheimer's disease. (B) Details of Aβ expression in hippocampal CA1 area of 3-, 9-, 12- and 18M-old mice. Yellow arrows point to the intracellular expression in pyramidal neurons (all ages), blue arrows point to the extracellular plaques (18 months only) andwhite arrows point to the EGFP labeled astrocytes lacking intracellular Aβ expression. (C) Relative mRNA expression of 3xTg-AD marker genes in EGFP-positive hippocampal astrocytes isolated from 3M-old mice. The expression of all three mutated genes was maintained in hybrid mice. Data are presented as mean ± SEM. Statistical significance was determined by Student's *t*-test. Asterisks indicate significant differences (***$p < 0.001$). Ctrl, control; 3xTg-AD, triple transgenic model of AD crossbred with GFAP/EGFP mice; GFAP, glial fibrillary acidic protein; EGFP, enhanced green fluorescent protein; Aβ, amyloid-β; AppSwe, Swedish mutation in amyloid precursor protein gene; TauP301L, P301L mutation of tau protein gene; Psen1M146, M146V mutation of presenilin1 gene; 3M, 9M, 12M, 18M, 3-, 9-, 12-, 18-month-old animals.

differences were not observed under the exposure to hypo-osmotic stress, mirroring that hyperkalemia activates different mechanisms responsible for the swelling than hypo-osmotic stress. In the present study, such age-dependent cell volume variations were not observed in astrocytes from 3xTg-AD mice in response to hyperkalemia as only minor differences were observed between the age groups (**Figure 5**; **Supplementary Table 5**). Similar to physiological aging, hypo-osmotic stress revealed no age-related differences in astrocyte swelling of 3xTg-AD mice (**Figure 5**; **Supplementary Table 4**).

The quantification of volume changes evoked by the hypo-osmotic stress in 3M and 18M animals revealed no differences between the controls and 3xTg-AD mice. In 3M mice ΔV_c reached the maximal values of ∼120% in the controls, and ∼121% in the 3xTg-AD (**Figure 6A**). In 18M mice it was ∼118% in the controls and ∼121% in 3xTg-AD mice (**Figure 6D**). Significant differences between the controls and 3xTg-AD mice were observed in both 9- and 12M. In 9M mice, the astrocyte volume increased to ∼128% in the controls, while it reached only ∼108% in 3xTg-AD after 20 minutes of $aCSF_{H-100}$ application (**Figure 6B**). In 12M mice, the volume increased to the maximum values of ∼119% in the controls and ∼109% in 3xTg-AD (**Figure 6C**). The complete data are summarized in **Supplementary Table 4**.

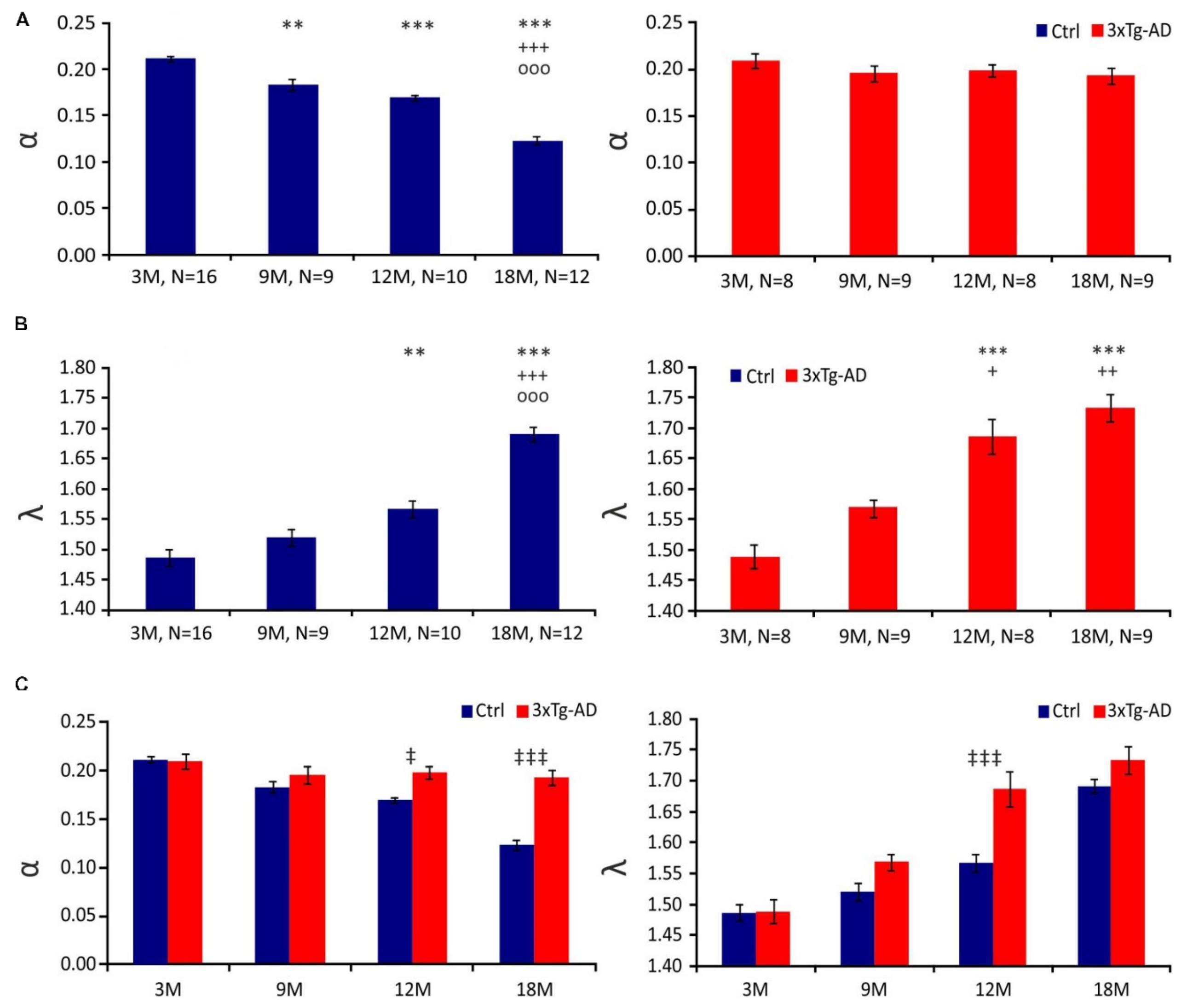

FIGURE 2 | Diffusion parameters of extracellular space during aging of control (Ctrl) and 3xTg-AD mice at 3, 9, 12 and 18 months (3, 9, 12 and 18M). Average values of the volume fraction α (A) and tortuosity λ (B) during aging in Ctrl (left) and 3xTg-AD mice (right). Note the continuous decrease in α during a physiological aging which is missing in 3xTg mice. A marked increase in λ occurred in 3xTg-AD animals earlier than in Ctrl mice. Comparison of values of α (left) and λ (right) between Ctrl and age-matched 3xTg-AD mice (C). Data are expressed as mean ± SEM. Statistical significance was determined by Student's *t*-test with Benjamini-Hochberg post-hoc test. Asterisks, crosses, circles and double daggers indicate significant differences ($p < 0.05$ [*/+/o/‡ significant]; $p < 0.01$[**/++/oo/‡‡ very significant]; $p < 0.001$ [***/+++/ooo/‡‡‡ extremely significant]). * indicates a significant difference related to the values of 3M-old mice; + indicates a significant difference related to the values of 9M-old mice; o indicates a significant difference related to the values of 12M-old mice, ‡ indicates a significant difference between Ctrl and age-matched 3xTg-AD mice. Ctrl, control mice; 3xTg-AD, triple transgenic model of AD; 3M, 9M, 12M, 18M, 3-, 9-, 12-, 18-month-old animals; N, number of animals.

The quantification of volume changes evoked by hyperkalemia in 9M and 18M animals revealed no differences between the controls and 3xTg-AD mice. In 9M mice, ΔV_c reached the maximal values of ∼133% in the controls and ∼123% in 3xTg-AD (**Figure 6F**). In 18M mice, it was ∼136.6% in the controls and ∼131% in 3xTg-AD mice (**Figure 6H**). Significant differences between control and 3xTg-AD were observed in 3M and 12M mice. In 3M mice, the astrocyte swelling reached maximal values of ∼169% in the controls, while only ∼129 in 3xTg-AD (**Figure 6E**). In 12M mice, the highest values of swelling reached to ∼164% in the controls and only ∼117% in 3xTg-AD (**Figure 6G**). The complete data are summarized in **Supplementary Table 5**.

Overall, we found that astrocyte swelling due to both hypo-osmotic stress and hyperkalemia was lower in the 3xTg-AD mice than in the controls. In addition, the astrocytic swelling in the AD model did not change with increasing age.

To assess the contribution of the cell somas and processes to the total changes in astrocyte volume, we calculated the

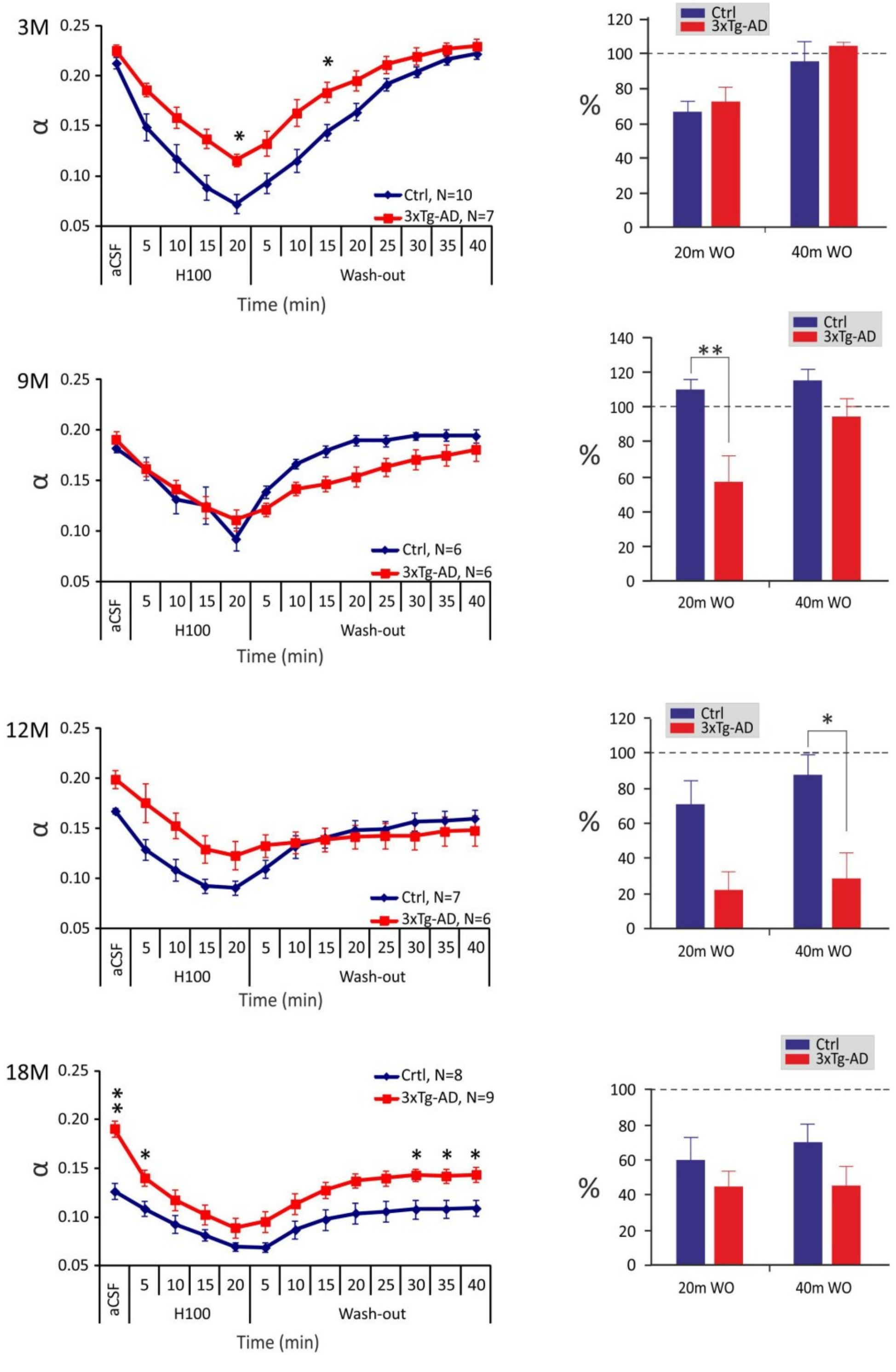

FIGURE 3 | Age-dependent changes of the absolute values of the ECS diffusion parameters in control and 3xTg-AD mice evoked by hypo-osmotic stress. The left side: Time course of the volume fraction (α) changes during a 20-min application of aCSF$_{H-100}$ and a 40-min washout in 3-, 9-, 12- and 18M-old control animals and age-matched 3xTg-AD mice. The right side: Volume fraction recovery during washout at 20 min intervals is expressed as changes in the values reached in the 20th min of application, set as 0%. Data are presented as mean ± SEM. Statistical significance was determined by two-way ANOVA test with Tukey's *post hoc* test. Asterisks indicate significant differences between Ctrl and 3xTg-AD mice ($*p < 0.05$, $**p < 0.01$). Ctrl, control mice; 3xTg-AD, triple transgenic model of AD; aCSF, artificial cerebrospinal fluid; H100, hypotonic artificial cerebrospinal fluid; WO, wash-out; 3M, 9M, 12M, 18M, 3-, 9-, 12-, 18-month-old animals; N, number of animals.

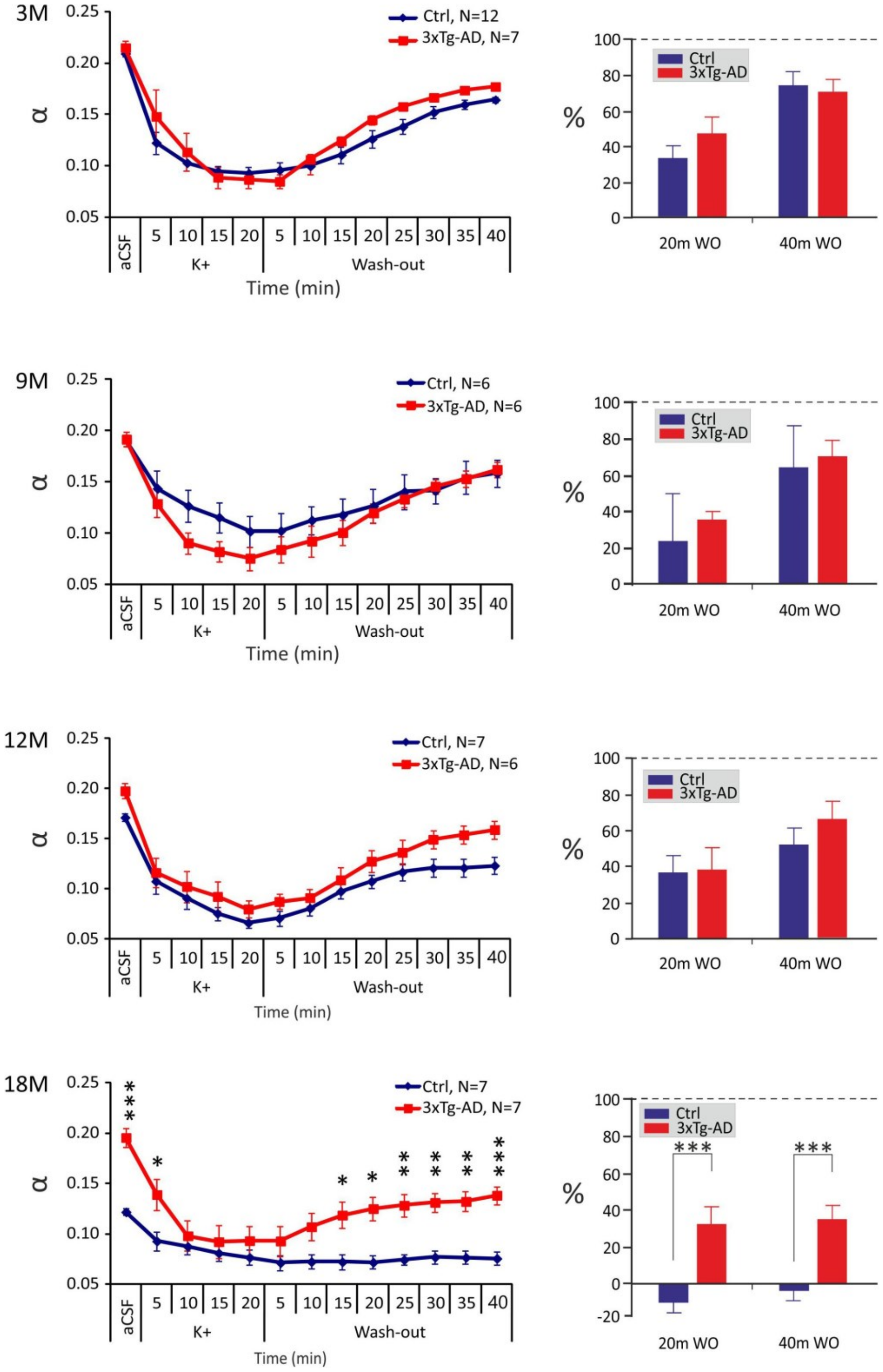

FIGURE 4 | Age-dependent changes of the absolute values of the ECS diffusion parameters in control (Crtl) and 3xTg-AD mice evoked by severe hyperkalemia (50 mM K^+). The left side: Time course of the volume fraction (α) changes during a 20-min application of $aCSF_{K+}$ and a 40-min washout in 3-, 9-, 12- and 18M-old control animals and age-matched 3xTg-AD mice. The right side: Volume fraction recovery during washout at 20 min intervals is expressed as changes in the values reached in the 20th min of application, set as 0%. Data are presented as mean ± SEM. Statistical significance was determined by two-way ANOVA test with Tukey's *post hoc* test. Asterisks indicate significant differences between Ctrl and 3xTg-AD mice ($*p < 0.05$, $**p < 0.01$, $***p < 0.001$). Ctrl, control mice; 3xTg-AD, triple transgenic model of AD; aCSF, artificial cerebrospinal fluid, K+, artificial cerebrospinal fluid with elevated K+ concentration; WO, wash-out; 3M, 9M, 12M, 18M, 3-, 9-, 12-, 18-month-old animals; N, number of animals.

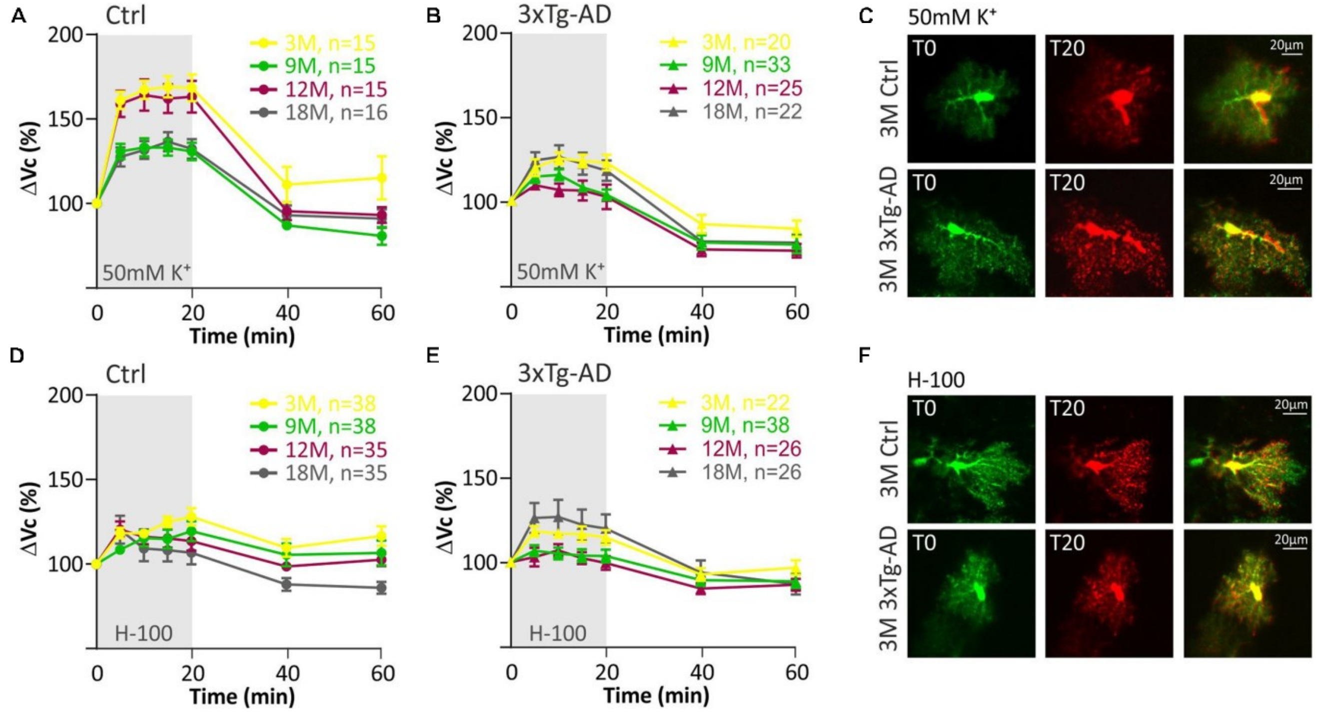

FIGURE 5 | Swelling of hippocampal astrocytes in response to severe hyperkalemia (50 mM K^+) or hypo-osmotic stress in aging controls and 3xTg-AD mice. (A,B) Time course of the total volume changes (ΔVc) in EGFP-positive cells during a 20-min application of $aCSF_{K+}$ and a 40-min washout. Note that in controls (left) the astrocyte swelling is comparable in 3M- and 12M- and in 9M- and 18M-old animals. No such age-related changes were observed in 3xTg-AD mice (right). (C) Representative images of EGFP-expressing astrocytes before (T0, red) and after the 20-minute exposure to 50 mM K^+ (T20, green). Overlays show merged images of cells with their initial volume (red) and swollen cells (green). Green area represents swelling induced by 50 mM K^+. (D,E) Time course of the total volume changes (ΔVc) in EGFP-positive cells during a 20-min application of $aCSF_{H-100}$ and a 40-min washout. Note that no changes were observed between age groups in either controls or 3xTg-AD. (F) Representative images of EGFP-expressing astrocytes before (T0, red) and after the 20-min exposure to H-100 (T20, green). Overlays show merged images of cells with their initial volume (red) and swollen cells (green). Green area represents swelling induced by H-100. Data are presented as mean ± SEM. Statistical significance was determined by two-way ANOVA test with Tukey's *post hoc* test. Ctrl, control; 3xTg-AD, triple transgenic model of AD crossbred with GFAP/EGFP mice; GFAP, glial fibrillary acidic protein; EGFP, enhanced green fluorescent protein; aCSF, artificial cerebrospinal fluid; H-100, hypotonic artificial cerebrospinal fluid; 50 mM K^+, artificial cerebrospinal fluid with elevated K^+ concentration; 3M, 9M, 12M, 18M, 3-, 9-, 12-, 18-month-old animals; n, number of cells.

ratio of the processes volume change to the volume change of the soma (**Figure 7**). The exposure to $aCSF_{H-100}$, revealed no significant differences in $V_{processes}/V_{soma}$ ratio between the controls and 3xTg-AD mice (**Figure 7A**). The only significant differences were found in 3M-old animals during washout following the exposure to $aCSF_{K+}$. While swelling of the processes significantly predominated in the controls, in 3xTg-AD mice the ratio approached one, indicating an equal contribution of both cell parts to the total volume changes (**Figure 7B**). As shown in our previous study (Kolenicova et al., 2020), the volume changes of somas and processes mainly reflect the redistribution of transport mechanisms within the astrocyte membrane. Therefore, we speculate that the increased contribution of processes to the persistent astrocyte swelling in the washout is due to the locally lower expression of channels/transporters responsible for volume regulation. This phenomenon is likely to change during aging, when the expression of the channels/transporters is equally distributed on both somas and processes.

The Number of Cells That Respond to Pathological Conditions With a Low Rate of Swelling Is Increased in Alzheimer's Disease

The astrocyte volume changes in all tested groups were analyzed using SOM (self-organizing map) analysis to determine whether distinct astrocyte subpopulations with a different ability to regulate their volume also appear during aging, as described in our previous study (Benesova et al., 2009). Cells from all ages were pooled and divided by SOM analysis into two groups of astrocytes based on the size of their swelling and the course of volume changes over time (**Figure 8**). These two groups were profiled based on volume changes induced by both hypo-osmotic stress (**Figure 8A**) and hyperkalemia (**Figure 8C**). Two groups of astrocytes were labeled following our previous study as HR (high-responding) and LR (low-responding). In hypo-osmotic stress, the volume of HR cells reached ~156% in the 20th min of $aCSF_{H-100}$ exposure, while the maximal volume of LR cells was only ~108%. The percentage of HR and LR cells did not

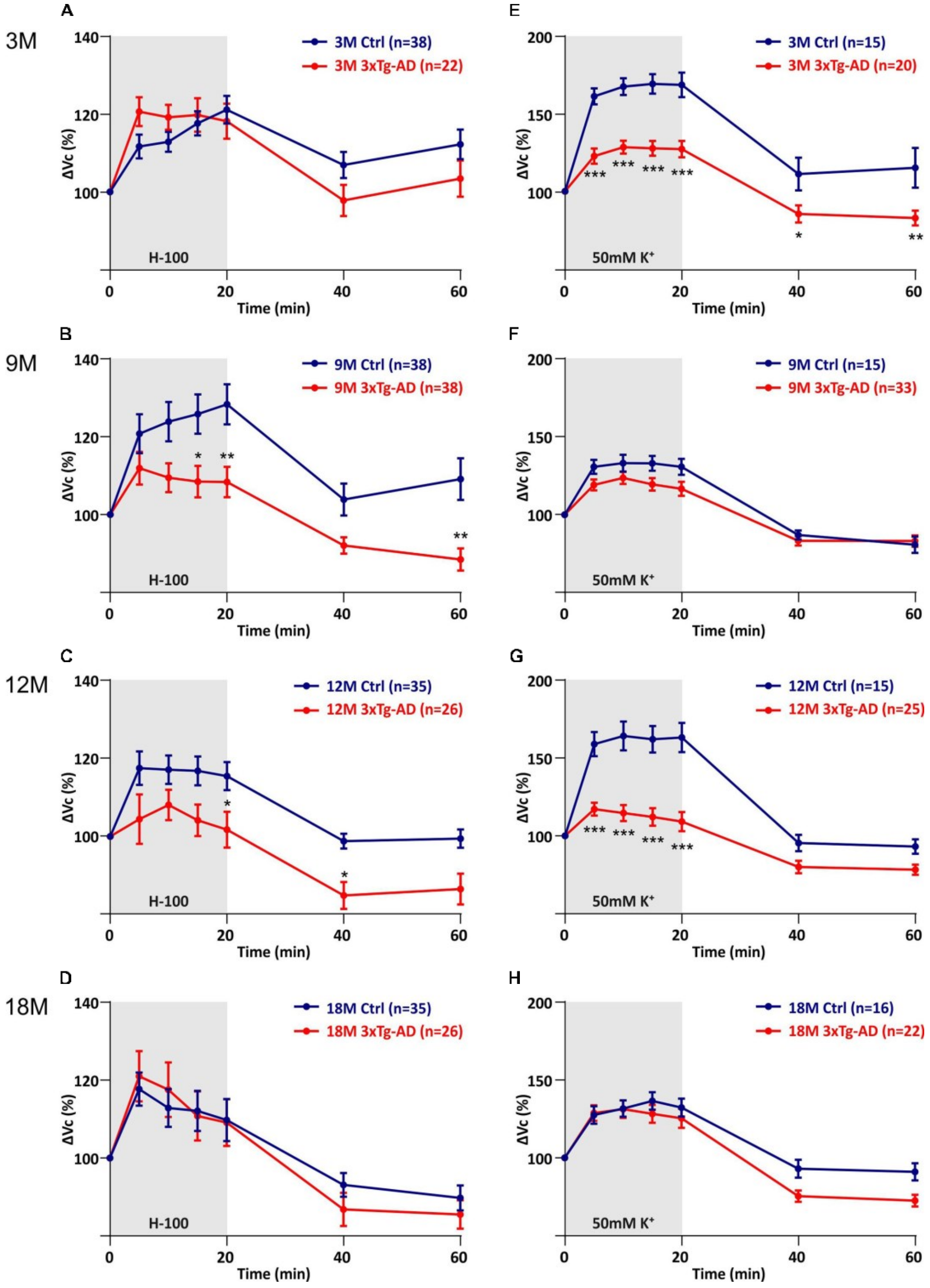

FIGURE 6 | Comparison of astrocyte swelling in controls and 3xTg-AD during exposure to hypo-osmotic stress or severe hyperkalemia (50 mM K$^+$). (A–D) Time course of the total volume changes (*Δ*Vc) in EGFP-positive cells during a 20-min application of aCSF$_{H-100}$ and a 40-min washout. Note that the astrocyte swelling is comparable in 3M- and 18M-old animals, while the astrocytic swelling in 9M- and 12M-old controls significantly exceeds the swelling in 3xTg-AD. (E–H) Time course of the total volume changes (*Δ*Vc) in EGFP-positive cells during a 20-min application of aCSF$_{K+}$ and a 40-min washout. Note that the astrocyte swelling is comparable in 9M- and 18M-old animals, while the astrocytic swelling in 3M- and 12M-old controls significantly exceeds the swelling in 3xTg-AD. Data are presented as mean ± SEM. Statistical significance was determined by two-way ANOVA with Tukey's multiple comparison test. Asterisks indicate significant differences (*$p < 0.05$, **$p < 0.01$, ***$p < 0.001$). Ctrl, control; 3xTg-AD, triple transgenic model of AD crossbred with GFAP/EGFP mice; GFAP, glial fibrillary acidic protein, EGFP, enhanced green fluorescent protein; aCSF, artificial cerebrospinal fluid; H-100, hypotonic artificial cerebrospinal fluid; 50 mM K$^+$, artificial cerebrospinal fluid with elevated K$^+$ concentration; 3M, 9M, 12M, 18M, 3-, 9-, 12-, 18-month-old animals; n, number of cells.

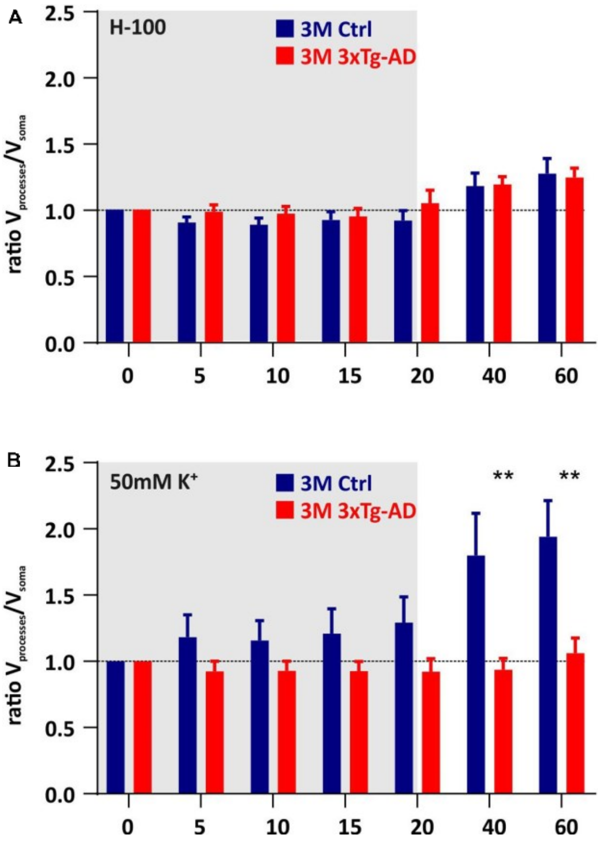

FIGURE 7 | Contribution of cell somas/processes to the total volume changes induced by hypoosmotic stress (A) or hyperkalemia (B). The bar graph shows the ratio of the change of processes volume to the change in soma. Note that under hyperkalemia, swelling of the processes predominates over the swelling of the somas, in the 3M-old controls, while in the respective age group in 3xTg-AD mice the somas and processes swell comparatively. Data are presented as mean ± SEM. Statistical significance was determined by two-way ANOVA test with Tukey's *post hoc* test. Asterisks indicate significant differences (**$p < 0.01$). Ctrl, control; 3xTgAD, triple transgenic model of AD crossbred with GFAP/EGFP mice; GFAP, glial fibrillary acidic protein; EGFP, enhanced green fluorescent protein; H-100, hypotonic artificial cerebrospinal fluid; 50 mM K+, artificial cerebrospinal fluid with elevated K+ concentration; 3M, 3-month-old animals.

differ between the controls and 3xTg-AD mice in either age group (**Figure 8B**). In hyperkalemia, the volume of HR cells reached the maximal value of ∼162% in the 20th min of $aCSF_{K+}$ exposure, while the maximal volume of LR cells did not exceed ∼117%. The percentage of HR and LR cells differed significantly between the control and 3xTg-AD in 3M and 12M mice (**Figure 8D**). In 3M controls, the HR group comprised 73% astrocytes, while in the 3M 3xTg-AD mice it was only 26%. In the 12M animals, the HR group was as high as 85% of control astrocytes, while only 18% of 3xTg-AD astrocytes.

Collectively, two subpopulations of astrocytes were present in all age groups in both the controls and 3xTg-AD animals. The only difference in the incidence of HR/LR cells was found in 3M and 12M 3xTg-AD mice during their exposure to $aCSF_{K+}$.

The Expression of Astrocytic Genes Responsible for the Ion and Water Movement Changes With the Progression of Alzheimer's Disease Symptoms

As the volume changes of astrocytes exposed to hypo-osmotic stress or hyperkalaemia differed significantly between the controls and 3xTg-AD mice, we hypothesized that the different volume changes reflect the altered expression of channels/transporters involved in the transport of osmotically active substances and water across the astrocytic membranes. Therefore, we performed a scRT-qPCR to determine the expression profiles of astrocytic channels, transporters and receptors that participate in maintaining ion and neurotransmitter homeostasis. The analysis of expression of 96 genes (for their complete list see **Supplementary Table 1**) was carried out in EGFP-positive cells collected from the CA1 region of the hippocampus from the 3M, 9M, 12M, and 18M controls or 3xTg-AD mice.

In accordance with the above-described data, we also found distinct astrocyte subpopulations based on their gene expression profiles. Employing the principal component analysis (PCA) two groups of EGFP-positive astrocytes, PCA1 and PCA2 were identified, differing in the expression levels of 35 genes as well as in the percentage level of cells expressing these genes (**Figure 9**). Differentially expressed genes comprise, primarily, those encoding aquaporins and connexins (*Aqp4, Gja1, Gjb6*), chloride and anion channels (*Clcn3, Clcn4, Vdac2*), potassium channels (*Kcnk1, Kcnj10*) and metabotropic and ionotropic glutamate receptors (*Grm3, Grin2c, Gria2*).

Comparing the 3xTg-AD mice and their age-matched controls significant differences in the expression levels of 24 genes were found (**Figure 10**). In the 3M 3xTg-AD mice, most of the differentially expressed genes were downregulated, compared to the controls. The most noteworthy decreases in the gene expression were observed for *Glul* encoding glutamine synthetase (GS), *Grin2c* encoding 2C subunit of NMDA receptors, *Gjb6* encoding connexins 30, *Kcnj10* encoding Kir4.1 potassium channel, *Slc1a2 and Slc1a3* encoding excitatory amino acid transporters (EAATs) and *Atp1a2* encoding ɑ-2 subunit of Na^+/K^+ ATPase. In the 3M 3xTg-AD mice the only upregulated astrocytic gene was *Vdac3* encoding voltage -dependent anion channel 3. Notably, the expression of genes, which were downregulated in the 3M 3xTg-AD mice, increased with aging. The maximal difference was observed in the 12M 3xTg-AD mice and their age-matched controls. At 18 months, the expression of most genes was comparable between the controls and 3xTg-AD mice. The age-related expression changes of selected genes are shown in **Figure 10E**. For other genes involved in astrocyte volume changes, such as *Slc12a2, Slc12a4*, and *Clcn2* (encoding (Na^+)-K^+-Cl^- cotransporters and ClC2 channels), we observed rather low expression levels in astrocytes from both the controls and 3xTg-AD mice. Nevertheless, in the 12M 3xTg-AD mice, *Slc12a2* was downregulated, while *Slc12a4* and *Clcn2* were upregulated.

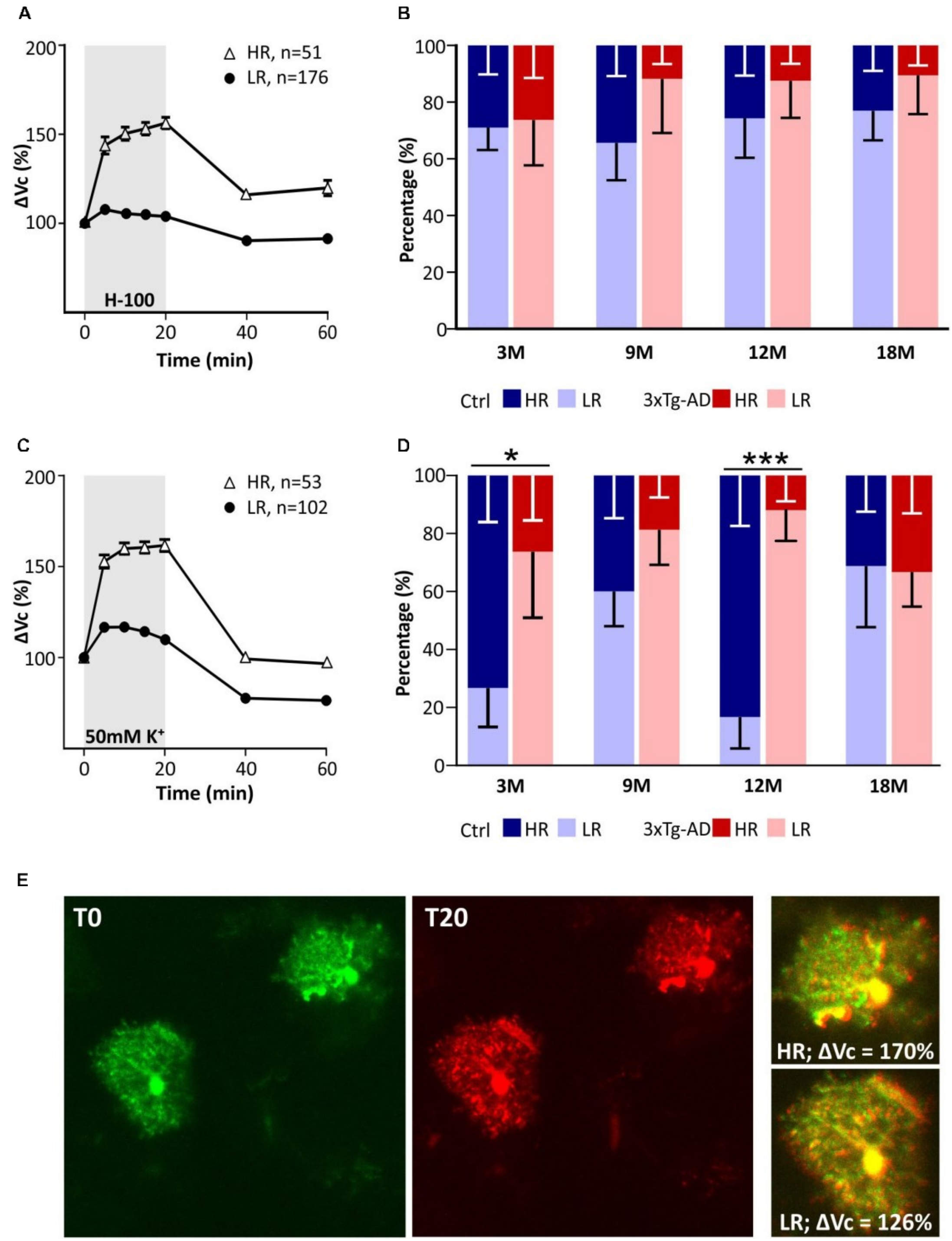

FIGURE 8 | Characterization of two groups of EGFP-positive astrocytes responding to pathological conditions with high or low rate of swelling identified in hippocampus of controls and 3xTg-AD mice. Subpopulations differ in the size of the swelling and the course of volume changes during the exposure to hypo-osmotic stress (A) or hyperkalemia (C). Comparison of the incidence of HR- and LR-astrocytes between controls and 3xTg-AD in individual age groups in hypo-osmotic stress (B) or hyperkalemia (D). Note that the number of astrocytes responding with a low rate of swelling is significantly increased in 3- and 12M-old 3xTg-AD mice. (E) Representative images of HR- and LR- EGFP-expressing astrocytes before (T0, red) and after the 20-min exposure to 50 mM K^+ (T20, green). Overlays show merged images of cells with their initial volume (red) and swollen cells (green). Green area represents swelling induced by 50 mM K^+. Data are presented as mean ± SEM. Statistical significance was determined by two-way ANOVA test with Tukey's *post hoc* test. Asterisks indicate significant differences (*$p < 0.05$, ***$p < 0.001$). Ctrl, control; 3xTg-AD, triple transgenic model of AD crossbred with GFAP/EGFP mice; HR, high-responding astrocytes; LR, low-responding astrocytes; H-100, hypotonic artificial cerebrospinal; 50 mM K+, artificial cerebrospinal fluid with elevated K^+ concentration; 3M, 9M, 12M, 18M, 3-, 9-, 12-, 18-month-old animals; n, number of cells.

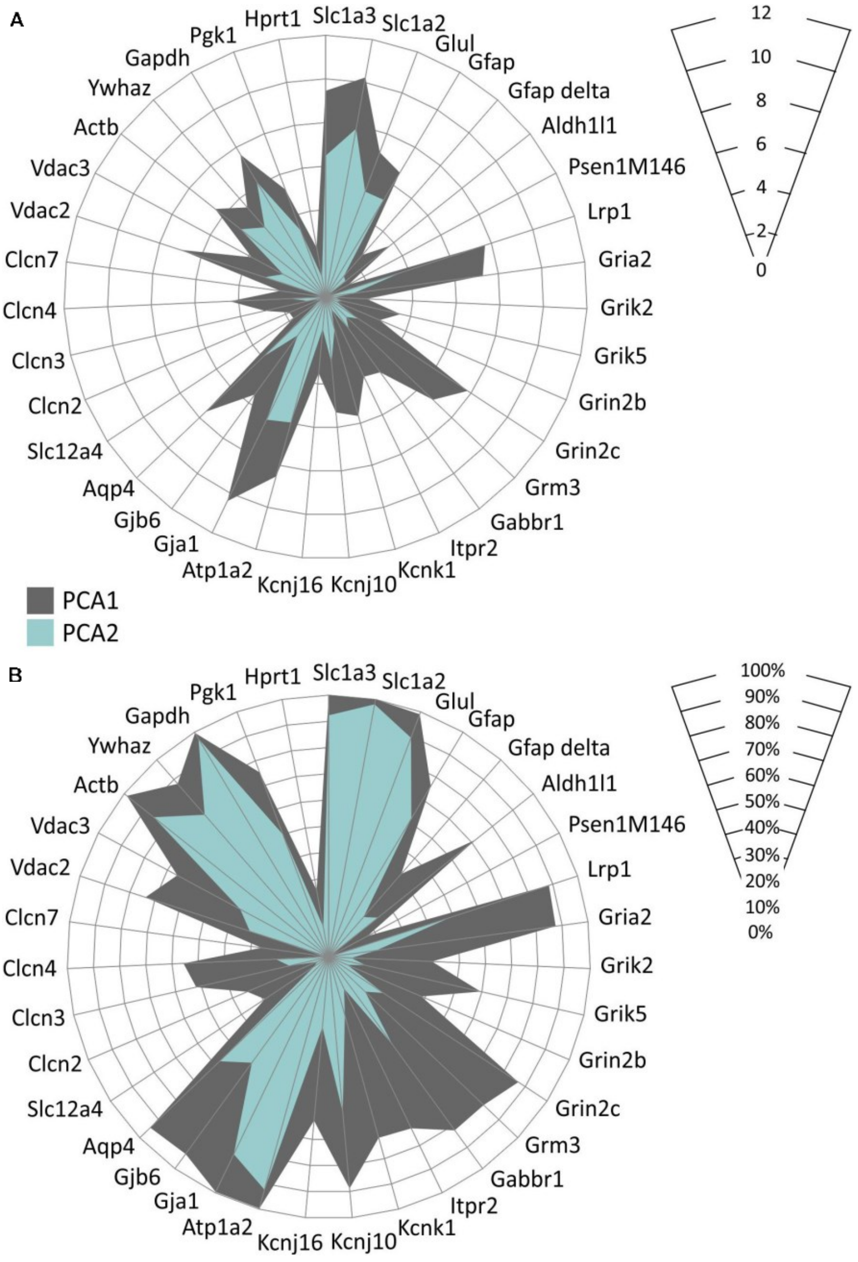

FIGURE 9 | Characterization of two EGFP-positive astrocyte subpopulations differing in the expression of the homeostatic genes identified in hippocampus of controls and 3xTg-AD mice. Subpopulations differ in levels of expression of selected genes (A) and in the percentage of cells expressing these genes (B). Only genes, the expression of which was changed significantly ($p < 0.05$) are depicted. Statistical significance was determined by two-way ANOVA test with Tukey's *post hoc* test.

Overall, we already observed changes at the gene level in 3M animals, which can affect the uptake of ions and neurotransmitters from the ECS, as well as the ability of astrocytes to regulate their volume. The decreased expression of some genes changes with age, possibly due to compensatory mechanisms. In addition, we found that even within one age group, there are significant differences in the gene expression between astrocytes. Based on this, we identified two groups of astrocytes, differing in the expression levels of 35 genes, as well as in the percentage of cells expressing these genes.

DISCUSSION

In this study, we described a new mouse strain, created by crossing the 3xTg-AD model of AD (Oddo et al., 2003) with GFAP/EGFP mice (Nolte et al., 2001), in which we detected

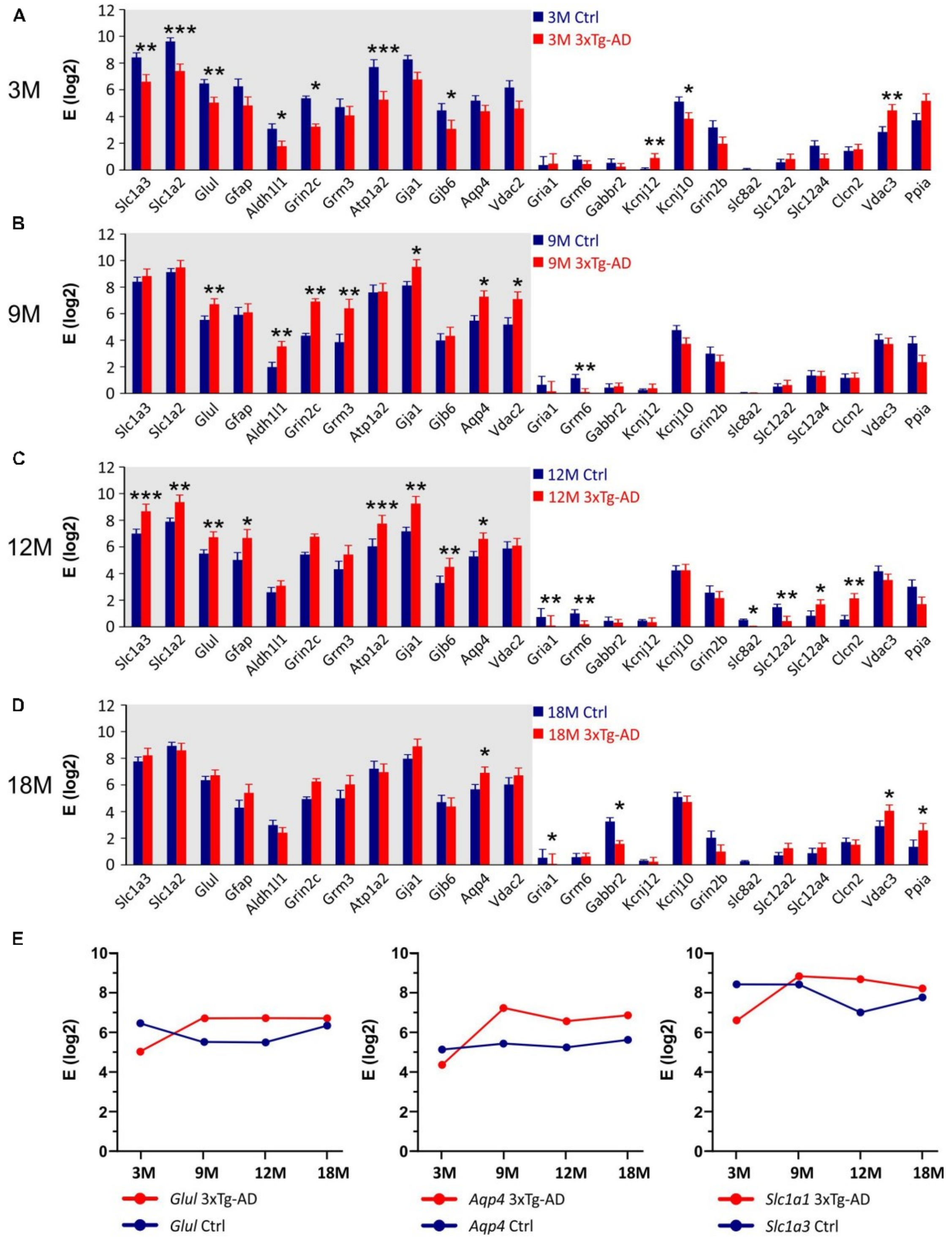

FIGURE 10 | Gene expression analysis in hippocampal EGFP-positive astrocytes of 3xTg-AD mice. (A–D) Relative mRNA levels (log scale) of genes significantly changed in 3M- (A), 9M- (B), 12M- (C) and 18M- (D) -old 3xTg-AD mice compared to age-matched controls. Normalized data are expressed as fold changes compared to the sample with the lowest expression of the gene. Data are presented as mean ± SEM. Statistical significance was determined by two-way ANOVA test with Tukey's *post hoc* test. Genes undergoing significant changes during aging are indicated by a gray background. Asterisks indicate significant differences (*$p < 0.05$, **$p < 0.01$, ***$p < 0.001$). (E) Age dependent changes of relative mRNA levels of genes encoding glutamin synthetase (*Glul*), aquaporine 4 (*Aqp4*) and glutamate transporters GLAST (*Slc1a3*). Ctrl, control; 3xTg-AD, triple transgenic model of AD crossbred with GFAP/EGFP mice; GFAP, glial fibrillary acidic protein; EGFP, enhanced green fluorescent protein; 3M, 9M, 12M, 18M, 3-, 9-, 12-, 18-month-old animals; Aliases of all genes are summarized in Supplementary Table 1.

an intracellular expression of Aβ in pyramidal neurons in 3M animals which is earlier than in the original 3xTg-AD model. In this AD model, we did not observe any changes in the ECS volume fraction during aging, but the increase in the number of obstacles that we observed in physiological aging occurred faster. The changes in α and λ evoked by hypo-osmotic stress were comparable between the AD model and the age-matched controls, the only difference was observed in the rate of α recovery in 9M and 12M animals. Similarly, changes in α and λ evoked by hyperkalemia were comparable between the 3xTg-AD mice and controls within 3 - 12M, however in 18M mice, a marked decrease in α and compromised recovery was detected in controls compared to the 3xTg-AD mice. We can subsequently summarize that single astrocyte swelling evoked by both hypo-osmotic stress and hyperkalemia was lower in the 3xTg-AD mice than in controls and it did not change with increasing age. We further found that these changes only occur in a certain subpopulation of astrocytes, which becomes more numerous during the progression of AD symptoms. Finally, we already observed a decrease in the expression of genes in the 3M animals, which can affect the uptake of ions and neurotransmitters from the ECS, as well as the ability of astrocytes to regulate their volume. These are mainly genes of astrocytic glutamate transporters, α2β2 subunit of Na^+/K^+-ATPase, connexin 30 or Kir4.1 channels.

Animal Model

For studying the morphological changes of astrocytes, we generated a new mouse strain by crossbreeding 3xTg-AD mice with GFAP/EGFP mice (Nolte et al., 2001). The original triple transgenic model was generated by Oddo et al. (2003) to study the interactions between Aβ and tau and their joint effect on the synaptic function. The triple transgenic mice develop both the main features of AD, the amyloid plaques and the neurofibrillary tangles. The authors reported the intraneuronal Aβ immunoreactivity as one of the earliest manifestations of the neuropathology. It was observed in the hippocampus from the age of six months. In contrast, our results already revealed the intracellular Aβ expression in the hippocampal pyramidal neurons in 3M animals. On the other hand, in the original work, the hippocampal expression of extracellular Aβ deposits was observed from 12 months, while we failed to detect them until 18-months of age. A possible explanation for this discrepancy is the different genetic background of the experimental animals. The original 3xTg-AD model has a different genetic background (C57Bl/6) to the GFAP/EGFP model (FVB/NJ), therefore our double transgenic model has a mixed background. A distinct phenotype of AD models created on different genetic backgrounds has been suggested by Frohlich and co-authors (Frohlich et al., 2013). They found a significantly higher number of plaques as well as an increased intracerebral concentration of Aβ42 in APP/PS1 mice on a C57Bl/6J background than in FVB/N background mice (APPtg-FVB). Furthermore, these data correlated with the microglial activity which was enhanced in the APPtg-FVB mice. Qosa and Kaddoumi (2016) described the different clearance of Aβ in four mouse strains widely used for the development of AD mouse models. The authors observed a decreased expression of LRP1 protein, which is responsible for Aβ clearance in SJL/J mice compared to C57Bl/6, FVB/N, and BALB/c. They further reported that the brain degradation of Aβ decreases in BALB/c, FVB/N, and SJL/J mice after administration rifampicin, which is a commonly used antibiotic that has previously been found to increase Aβ clearance across the blood-brain barrier (Qosa et al., 2012). Comparable reduced degradation was not observed in C57Bl/6 mice.

Changes in the Morphology of Astrocytes and Their Effect on Extracellular Space Diffusion Parameters

A gradual age-related decrease in α and increase in λ in mouse hippocampus with the most profound changes in 18M animals was reported in our recent study (Kolenicova et al., 2020), and confirmed in this study. Apart from the specific brain structures (thalamus, brainstem acoustic nuclei), rich on protective perineuronal and perisynaptic nets of condensed ECM, smaller or larger alterations in brain diffusion detected by the RTI method or diffusion-weighted magnetic resonance seems to be a common feature of aged nervous tissue (Sykova and Nicholson, 2008). Some controversy on the extent of age-evoked α, λ or apparent diffusion coefficient of water (ADC_W) changes observed among the studies, resulted from complex structural alterations of the aging tissue including changes in glial atrophy and/or astrogliosis (Rodriguez-Arellano et al., 2016), deposits of Aβ (Xekardaki et al., 2015), microglia activation (Harry, 2013), or changes in the ECM composition (Morawski et al., 2012; Morawski et al., 2014; Vegh et al., 2014b), which can affect the ECS diffusion parameters and can vary in distinct brain regions or different species. Interestingly, more substantial α and ADC_W decreases in females than in males were revealed during "late" aging (17-28- months of age) (Sykova et al., 2005) while no gender-related differences were detected in "early" aging (16-18 months of age) (Cicanic et al., 2018).

In contrast to physiological aging, we detected no age-related decline in α in 3xTg-AD mice. This finding corresponds with the observation in another AD model, APP23 mice (Sykova et al., 2005) and may be associated with amyloid deposits in the ECS, preventing the shrinkage of the ECS volume in aged tissue. However, the immunohistochemical analysis showed an extracellular amyloid load no earlier than in the 18M 3xTg-AD animals (**Figure 1**). Therefore, the contribution of other factors such as atrophy of astrocytes (Rodriguez-Arellano et al., 2016) or shifts in the composition of ECM (Morawski et al., 2012; Sethi and Zaia, 2017) should be taken into account, especially in the earlier phase of aging.

Sykova et al. (2005) also reported a decrease in ADC_W and ADC_{TMA} indicating more hindered brain diffusion than in the controls, but only in APP23 females and not in APP23 males. Moreover, some studies showed a gender-dependent impairment of water-maze performance in aged APP23 mice, as well as a higher plaque load in females than in males (Kelly et al., 2003; Sykova et al., 2005). On the contrary, in 3xTg-AD mouse model containing mutations not only in APP but also in tau protein and presenilin, we did not detect any gender-related difference in amyloid load, the ECS diffusion parameters, or in astrocyte swelling. In this study, we observed more hindered extracellular diffusion (larger λ values) in the 12M 3xTg-AD mice than in the age-matched controls. In fact, an increase in λ during physiological aging was accelerated in the 3xTg-AD mice with a substantial "jump" already between the 9 and 12 months of age, while a similar substantial λ increase occurred between 12 and 18 months of age in the controls. Again, as amyloid is not expressed extracellularly in 12M animals, other key elements creating diffusion barriers, such as morphological changes of glia cells and/or increase of ECM expression, have to play a role in the observed λ increase.

Our previous studies of various pathological conditions revealed that increased ECS volume and/or tortuosity are in accordance with the ECM overexpression (Roitbak and Sykova, 1999; Zamecnik et al., 2004), while smaller values of α and/or λ associate with overall decrease of ECM content or lack of a core ECM molecules (Sykova et al., 2005; Bekku et al., 2010). Thus, to explain increased values of both α and λ in the aged 3xTg-AD mice, we would expect ECM overexpression in AD-affected tissue. In contrast, a loss of ECM forming perineuronal nets in AD tissue was reported in older studies based on detection of N-acetylgalactosamine by lectins Wisteria foribunda and vicia villosa (Baig et al., 2005). However, more recent study of Morawski et al. (2012) showed that this loss of ECM was an artifact caused by decomposition of post mortem tissue. In fact, perineuronal nets remained intact in well-preserved AD tissue and hyaluronan is even enriched in amyloid plaque territories (Morawski et al., 2012). Similarly, significant increases in the levels of several protein components of the ECM, with increases in Aβ levels was found in the hippocampus; these increases occurred before the onset of plaque formation in association with impairment of long-term potentiation and contextual memory (Vegh et al., 2014a).

Progressive increase in tortuosity with aging in 3xTg-AD mice without changes in the ECS volume might seem counterintuitive but only in comparison with acute states, such as acute ischemia (Vorisek and Sykova, 1997). In this case, cell swelling is accompanied by a compensatory shrinkage of the ECS leading to a decrease in α and increase in λ due to a higher concentration of already existing diffusion barriers in a smaller space. However, we have shown in several of our previous studies that α and λ behave independently in chronic or long-lasting states where the amount of diffusion barriers is increased (Roitbak and Sykova, 1999; Zamecnik et al., 2004; Anderova et al., 2011) or decreased (Bekku et al., 2010; De Santis et al., 2020). Generally, there are three main sources of diffusion barriers: 1. fine cell processes, especially astrocytic, 2. macromolecules of ECM and 3. dead space microdomains, i.e., concave geometrical formation of the ECS, where diffusing molecules can be "trapped" (for review see Hrabetova and Nicholson, 2004; Sykova and Nicholson, 2008; Wolak and Thorne, 2013). Increased tortuosity in aged 3xTg-AD presumably results from a combination of all these factors. Both AD-related reactive astrogliosis with morphological rebuilding of astrocytic processes and increased expression levels of several ECM molecules were described in the very late stages of AD development (Morawski et al., 2012; Vegh et al., 2014a; Rodriguez-Arellano et al., 2016). Contribution of dead spaces is also possible especially in late stages of AD, when geometry of the ECS can be altered by the presence of amyloid plaques.

In contrast to the reduced hyperkalemia-induced swelling of astrocytes in the 9M and 18M 3xTg-AD mice in comparison with the controls, we did not detect similar differences in the ECS diffusion parameters. When comparing the extent of volume changes, we had to evaluate the relative changes due to different basal values α and λ between the control and 3xTg-AD mice, especially in the ages of 12 and 18 months. Relative values of volume fraction and tortuosity, calculated when the control values were set to 100%, did not show any significant differences between the control and 3xTg-AD mice, neither after hypotonic stress nor severe hyperkalemia. In animals with physiological aging, the exposure to 50 mM K^+ evoked more profound changes of absolute α in the 3M and 12M mice than in the 9M and 18M groups, similarly to changes in astrocyte swelling. In contrast, the pattern of α changes in 3xTg-AD animals was similar in all the tested age groups. In fact, there was a trend to a larger and especially faster α decrease during 50 mM K^+ exposure in the 3xTg-AD mice in comparison with the controls (**Supplementary Figure 3**). However, the differences became statistically insignificant after post-test. The discrepancy between the ECS volume changes and astrocyte swelling was already observed in our previous studies (Dmytrenko et al., 2013; Anderova et al., 2014; Kolenicova et al., 2020). It is quite predictable, as the changes of α measured by the RTI method reflect volume changes in all cell types, not just in astrocytes, and average thus the values from about 0.01-0.001 mm^3 of tissue. Apart from astrocytes, other cells with a large capability of swelling are neurons. A recent study by Genocchi et al. (2020) used a computational model of cortical spreading depression to explore how different parameters, including changes in AQP4 channel expression in astrocytes, neuron/astrocyte ratio and activity of Na^+/K^+-ATPase or chloride channels affect the swelling of neurons and astrocytes. Their results show that changes in each of these parameters may shift the proportion between neuronal and astrocytic swelling (Genocchi et al., 2020). Our results of astrocytic gene profiling undoubtably showed significant differences in the expression of some of the above-mentioned genes. We can therefore assume that a proportion of swelling of neurons and astrocytes (and possible other cell types) in the 3xTg-AD mice, differs from that in the control animals and may contribute to the larger discrepancy in the findings obtained by RTI and 3D confocal morphometry.

Following the evoked cell swelling, the values of α only recovered fully to the basal conditions in 3M, 9M, and 12M control animals and 3M and 9M 3xTg-AD mice, after $aCSF_{H-100}$. The recovery in the older groups was only partial. The partial recovery was also detected in all the tested groups after the application of $aCSF_{K+}$, with the exception of the 18M control animals, where no recovery was detected. This is in contrast to the astrocytic volume measurements, where a full recovery or even undershoot was observed in all the tested groups after hypo-osmotic stress or hyperkalemia. This discrepancy is due to the contribution of other cell types to the changes of α measured by the RTI method. Most other studies only attribute the ability to recover cell volume to astrocytes. Studies in neuronal cultures showed some extent of volume regulation in neurons by the releasing of taurine (Olson and Li, 2000; Li and Olson, 2008). However, a more recent study showed that neurons in tissue slices during oxygen/glucose deprivation swell rapidly, but are not capable of returning their volume to the original value (Risher et al., 2009). Astonishingly, in the 18M 3xTg-AD mice, the recovery was partial, while no recovery was observed in the age-matched control mice. No recovery in the control aged animals suggest possible irreversible tissue damage by severe depolarization evoked by 50 mM K^+, which could be even more pronounced in the older animals with an already small basal ECS volume. In fact, in 18M control mice, 50 mM K^+ evoked an α decrease to 0.07-0.08 which is close to values reached in terminal ischemia-anoxia (Vorisek and Sykova, 1997). In such a small space, concentration of glutamate or other toxic substances diluted in the interstitial fluid can be extremely high and may evoke irreversible cytotoxic damage of the tissue. Studies concerning spreading depression (SD), which main feature is a high potassium-evoked depolarization, reported prolonged SD duration and hampered recovery from SD in aged brain in comparison with young one and related these finding to functional alterations in membrane transporters and channels (for review see Hertelendy et al., 2019). Age-related impairment of ionic and neurotransmitter uptake was demonstrated also here and in our previous study (Kolenicova et al., 2020). Assuming that ionic and neurotransmitter homeostasis is altered in both control and 3xTg-AD aged mice, the larger initial ECS volume in the aged 3xTg-AD can be a protective factor buffering the concentration changes of toxic substances and enabling at least a partial recovery to control values.

Single Astrocyte Volume Changes and Their Relationship to Expression Levels of Channels and Transporters

In our recent study (Kolenicova et al., 2020), we showed that single astrocyte volume changes under exposure to high K^+ concentration alter during aging, which is a natural neurodegeneration process. Here we compare the age-related changes with changes caused by the pathological processes typical of AD. We show that the changes observed during aging occur earlier in the 3xTg-AD model of AD. We found lower volume changes in these mice when compared to the controls and these changes did not alter among the age groups. On the other hand, volume changes induced by hypo-osmotic stress showed no differences related to aging (Kolenicova et al., 2020), but in the 3xTg-AD astrocytes we observed significantly lower swelling than in the controls, similarly, to hyperkalemia. These results suggest that the mechanisms responsible for the uptake or extrusion of osmotically active substances, i.e., ions and neurotransmitters, as well as water transport mechanisms are impaired in the 3xTg-AD mice. We hypothesized that these defects are due to the altered expression of channels and transporters previously associated with astrocyte swelling under hypo-osmotic stress or ischemic conditions. Therefore, we performed sc RT-qPCR analysis and compared the gene expression of 96 selected homeostatic genes (**Supplementary Table 1**). In general, even in the young, 3M 3xTg-AD mice, a significantly lower expression of some homeostatic genes was observed compared to the control. In the 9M 3xTg-AD mice, the expression of these genes increased and remained at the same level until the age of 18 months. We believe that an overexpression may be a compensatory mechanism in response to the deterioration of astrocyte homeostatic functions.

One of the transporters for which we predicted changes in the expression profile was the Na^+-K^+-Cl^- cotransporter (NKCC1). In the previous study (Kolenicova et al., 2020) we showed that astrocyte volume changes during exposure to hyperkalemia were inhibited by bumetanide, an NKCC1 blocker. This cotransporter was also described to be involved in K^+-induced astrocyte swelling *in vitro* (Su et al., 2002) or in the optic nerve (MacVicar et al., 2002). NKCC1 contributes to the cell swelling by transferring ions into the cells and also by co-transferring water along with its substrates (Macaulay and Zeuthen, 2012). Since NKCC1 is abundantly expressed on other cell types in addition to astrocytes, such as endothelial cells which may also contribute to the cerebral oedema formation, the inhibition of this transporter is one of the options considered for the treatment of cerebral oedema (Deng et al., 2016). On the other hand, some authors report that astrocytic swelling induced by neuronal activity or 10.5 mM concentration of extracellular K^+ is not due to NKCC1 activity (Larsen et al., 2014; Walch et al., 2020). However, the sc RT-PCR analysis of astrocytes isolated from the 3xTg-AD mice revealed no significant change in the *Slc12a2* (NKCC1 encoding gene) expression, which is consistent with the literature, as no reference was found to the fact that Na^+-K^+-Cl^- cotransporter expression was altered in AD models. Therefore, we believe that it is unlikely that NKCC1 expression impairment is the cause of reduced swelling under the exposure to hypo-osmotic stress or hyperkalemia.

We further focused on the changes in the expression of AQP4 as this water channel plays multiple roles in the pathophysiology of AD. AQP4 affects ion and glutamate homeostasis, synaptic plasticity, astrocytic Ca^{2+} signaling, neuroinflammation, as well as Aβ and tau protein clearance (Lan et al., 2016; Assefa et al., 2018). Changes in AQP4 expression have even been considered a cause of the accumulation of Aβ plaques (Peng et al., 2016) and tau protein (Harrison et al., 2020) in the brain parenchyma (Tarasoff-Conway et al., 2015; Valenza et al., 2019). The accumulation is caused by the disruption of the so-called glymphatic system, which is responsible for the clearance of excess or defective proteins from the ECS (Plog and Nedergaard, 2018; Reeves et al., 2020). Since most studies describe an increase in AQP4 expression, the decreased clearance is possibly due to the loss of polarization, redistribution of AQP4, and mislocalization on non-endfoot membrane, rather than an overall change in expression. Changes in the localization of AQP4 on the astrocyte membrane have been described in the tg-ArcSwe mouse model of AD (Yang et al., 2011). The authors reported a loss of AQP4 from endfoot membranes at sites of perivascular amyloid deposits, emerging just after the appearance of the first plaques. Moreover, they found an upregulation of AQP4 in the neuropil surrounding the plaques. The increased expression was also observed in patients with AD or cerebral amyloid angiopathy by Moftakhar and co-authors (Moftakhar et al., 2010). Similarly, Hoshi and co-authors (Hoshi et al., 2012) showed an increased AQP4 expression in the temporal lobe of patients with sporadic or familiar form of AD; however, the expression differed between the inferior, middle and superior temporal cortices. Moreover, the authors report that the increased expression of AQP4 in senile plaques occurred during early Aβ deposition, whereas AQP4 downregulation occurred in the later stage of Aβ plaque formation. The role of AQP4 in astrocyte swelling and brain oedema formation has been suggested in several studies in which a less swelling in mice with deleted AQP4 was observed (Manley et al., 2000; Papadopoulos and Verkman, 2005). Another experimental approach used modifications in the subcellular distribution of AQP4 molecules, induced by the deletion of dystrophin or α-syntrophin in Syn-/- mice, leading to the reduced expression of AQP4 localized in the perivascular membranes of astrocytic endfeet. A delayed brain oedema formation after water intoxication was observed in these transgenic mice (Vajda et al., 2002; Amiry-Moghaddam et al., 2004). On the other hand, the participation of AQP4 in the swelling of individual astrocytes has been confirmed to be neither in elevated K^+ nor in hypo-osmotic stress (Murphy et al., 2017; Walch et al., 2020). In the first study the authors observed an increased swelling of astrocytes in hippocampal slices of AQP4–/– mice compared to the controls in a hypoosmolar cell swelling model (Murphy et al., 2017). In the second study, the authors observed no differences between the swelling of AQP4–/– mice and controls and slower recovery to baseline volume during the washout period after the 10.5 mM K^+ application (Walch et al., 2020). Therefore, they hypothesized that AQP4 is dispensable for astrocyte swelling, and in the absence of AQP4, astrocytes have impaired volume recovery. Their results are in line with findings that the deletion of AQP4 increased ECS shrinkage, indicating a possible role for AQP4–/– in astrocyte volume regulation (Haj-Yasein et al., 2012). Finally, a study with the new isoform-selective AQP4 inhibitor TGN-020 showed that K^+ uptake and associated astrocytic swelling are not dependent on AQP4 function (Toft-Bertelsen et al., 2021). All of the above-mentioned facts are consistent with the results presented in this work. In the 3xTg-AD model of AD, we observed a significant increase in AQP4 mRNA expression, along with an increasing incidence of Aβ plaques. These results are in slight contrast to Bronzuoli and co-workers (Bronzuoli et al., 2019), who reported an increase in AQP4 protein expression in the hippocampus of the 3xTg-AD mice during aging, but regardless of genotype. This discrepancy may stem from the different approaches used in the two studies, since we determined the mRNA expression at the single-cell level and in a subpopulation of EGFP-labeled astrocytes, while Bronzuoli et al. determined the total protein expression by Western blotting or immunohistochemistry. As AQP4 does not appear to play a role in astrocyte swelling, but rather contributes to cell volume regulation, increases in its expression correspond to lower swelling in the 3xTg-AD mice compared to the controls.

Other mechanisms that attracted our attention were those related to glutamate homeostasis. One of the basic properties of astrocytes, which are impaired in AD, is the uptake of glutamate from ECS. Several studies have revealed significant changes in the expression of glutamate transporters in both AD patients and mouse models (Jacob et al., 2007). On the contrary, other studies have not confirmed the reduced expression of EAATs (Beckstrom et al., 1999; Kulijewicz-Nawrot et al., 2013). The altered expression of glutamate-aspartate transporter (GLAST) has been observed by Ikegaya et al. (2002), Abe and Misawa (2003), Jacob et al. (2007), Matos et al. (2008). While Abe and Ikegaya observed GLAST reduction the others published opposite results. The conflicting data can be explained by different methodological approaches including amyloid preparation or culture conditions, but also by internalization or mislocalization as shown by Scimemi and co-authors (Scimemi et al., 2013) for glutamate transporter 1 (GLT-1). The authors reported an impaired glutamate clearance due to mislocalization of GLT-1 expression in slices treated with monomeric or oligomeric Aβ 1-42. In addition, regional differences such as those mentioned by Jacob and co-authors, must also be considered (Jacob et al., 2007). The reduced expression of glutamate transporters results in an impaired glutamate uptake and increased extracellular glutamate levels. This in turn leads to the overactivation of neuronal glutamate receptors resulting in synaptic dysfunction, which significantly contributes to the AD pathophysiology. Here we observed the reduced expression of *Slc1a2* (encoding GLT-1), but only in the 3M animals. In the older transgenic animals, GLT-1 expression values exceeded those observed in the controls, but the differences were rather due to the expression changes occurring in the controls during aging. The same pattern was observed for *Slc1a3* (encoding GLAST) expression.

In addition to the above-mentioned functions of AQP4, this water channel also regulates the function and expression of other channels/transporters, namely glutamate transporters, potassium channels and connexins. An association between AQP4 and GLT-1 has been proposed based on the findings that AQP4 deficiency downregulated GLT-1 in primary cultured astrocytes (Zeng et al., 2007) or mouse amygdala (Li et al., 2012). The changes in amygdala adequately influenced the synaptic plasticity as well as the fear memory (Li et al., 2012). Yang and co-authors (Yang et al., 2013) showed that GLT-1 stimulator (ceftriaxone, a β-lactam antibiotic known to upregulate GLT-1 in astrocytes) improved memory function in AQP4 deficient mice. Moreover, Hinson and co-authors suggested that AQP4 and GLT-1 co-exist in astrocytic membranes as a macromolecular complex, allowing their functional coupling (Hinson et al., 2008). Co-expression of the GLAST with AQP4 was discovered in the study of Nielsen (Nielsen et al., 1997). In line with these findings, we observed a very similar expression pattern for *Slc1a2*, *Slc1a3* and *Aqp4*.

Further, we assumed that the changes in glutamate transporter expression may also affect astrocyte swelling during exposure to pathological conditions. Pathological glutamate levels may contribute to the swelling by influx of Na^+, H^+ and glutamate in exchange for K^+. Nevertheless, the increased levels of intracellular Na^+ most likely inhibit this type of transport and GLAST and GLT-1 may rather contribute to the volume decrease by the supposed "uptake reversal" (Jabaudon et al., 2000). Moreover, the astrocytic water transport at the pial and vascular interfaces is predominantly mediated by AQP4, whereas the water passage at the neuropil facing membranes is determined by GLTs (MacAulay et al., 2002). Based on the expression changes observed in our study, glutamate transport in younger animals contributes to the astrocytic swelling, as it was upregulated in the control mice that swell more. On the other hand, in the 12M mice, where the GLAST and GLT-1 are upregulated in 3xTg-AD, the reverse transport appears to occur, as the astrocytes swell less. However, these proposals are only speculative, and a deeper examination of these mechanisms is necessary.

In addition to glutamate transporters, the glutamate homeostatic system is also affected by GS, and changes in its function may contribute to cognitive deficits in the diseased brain. Changes in GS expression have been described by Olabarria in 3xTg-AD mice (Olabarria et al., 2011) and by Hoshi in AD patients (Hoshi et al., 2018). In contrast, another human study showed increased levels of GS in the prefrontal cortex in AD (Burbaeva et al., 2005). Our observation is also not in line with Olabarria and co-authors. While these authors observed a GS expression decrease in the dentate gyrus in the 12M and 18M animals and in CA1 in 18M animals, we only detected a decrease in the 3M animals, but the GS expression was slightly increased compared to controls in older animals.

Similar to glutamate transporters, connexins (Cxs) also work in association with AQP4. Connexins form supposed "gap junctions," through which astrocytes are connected into a network called an astrocytic syncytium. This interconnection of astrocytes enables the effective buffering of K^+ and glutamate. An example of Cx-AQP4 collaboration is astrocytic K^+ siphoning, in which increased K^+ at the site of neuronal activity is taken up by K^+ channels along with water and shifted towards perivascular cells through astrocytic syncytium. At the end of this process, ions and water are extruded into the bloodstream via ion channels and AQP4 (Nicchia et al., 2005). Connexins play roles in the formation of glioma-induced brain oedema (Li et al., 2015) as well as cerebral oedema following ischemic brain injury (Chu et al., 2017). Bronzuoli and co-authors reported that Cx43 decreased with age in 3xTg-AD mice as well as in controls. Both the Western blotting and immunohistochemical analysis led to the conclusion that the Cx43 expression in the 3xTg-AD mice does not change due to genetic mutation, hence the presence of Aβ and tau in the ECS, but due to aging (Bronzuoli et al., 2019). On the contrary, we show here that the expression of both major astrocyte Cxs, Cx30 and Cx43 (encoded by *Gjb6* and *Gja1*) increased along with the development of the AD symptoms in the 3xTg-AD mice. However, Cxs have been proven to be involved in the cell volume regulation (Li et al., 2004; Ye et al., 2009). Thus, we can speculate that, similarly to AQP4, Cxs contribute to the volume regulation of astrocytes in 3xTg-AD mice.

Remarkable differences in gene expression were also observed for *Atp1a2* (encoding α2β2 isoform of Na^+/K^+-ATPase). While in the controls its expression decreased slightly with age, in the 3xTg-AD mice it increased and in the 18M mice the expression in both strains reached a similar level. As the α2β2 isoform is most sensitive to extracellular K^+ concentration, it provides a route for K^+ influx into astrocytes that could couple to water movement (Larsen et al., 2014). Therefore, the downregulation of *Atp1a2*, as observed by the gene expression analysis of this study, may contribute to the lesser swelling in the 3xTg-AD mice. Moreover, it possibly leads to breakdown of the electrochemical gradient, which is a prerequisite for neuronal excitability and the activity of glutamate transporters, such as GLAST and GLT-1. Thus, the decreased expression of *Atp1a2* leads secondarily to increased extracellular concentration of glutamate and likewise contributes to glutamate excitotoxicity (Klemens et al., 2019; Belov Kirdajova et al., 2020).

Since we performed the sc RT-qPCR analysis in astrocytes which has been sorted based on the EGFP expression, which was under the control of the GFAP promoter, we suggest that these cells may represent a minor subpopulation of astrocytes that exhibit different expression changes than those found in the other above-mentioned studies. This hypothesis may be supported by the fact that Aβ-induced expression changes are often observed in astrocytes showing reactive features, such as morphological changes as well as an increased GFAP expression. None of these properties were observed in EGFP-positive astrocytes in the hippocampus of the 3xTg-AD mice. Using single-nucleus RNA sequencing Habib and co-authors identified six astrocytic populations in the hippocampus of 5xFAD mice (Habib et al., 2020). The populations were described as low-GFAP, high-GFAP, disease-associated astrocytes (DAA) with transitional-like intermediate states between them. While low-GFAP and high-GFAP astrocytes were identified in both the controls and 5xFAD mice, DAAs were only found in the AD model. DAAs were characterized by the expression of reactive markers such as Serpina3n and Vimentin, and they also showed an increased expression of pan-reactive and inflammation astrocyte signatures. They were mainly found in the vicinity of Aβ plaques and their percentage increased sharply during the aging of the 5xFAD mice. The percentage of low-GFAP astrocytes increased with age in the controls and decreased in the 5xFAD mice, while the percentage of high-GFAP astrocytes decreased in the controls and remained constant in the 5xFAD. Regarding the homeostatic genes analyzed in our study, the largest differences were observed between the low-GFAP and high-GFAP populations of astrocytes. In the low-GFAPs, the genes *Gja1, Aqp4, Slc1a2, Kcnj10, and Kcnk1* were significantly downregulated, while *Grin2c, Gria2, and Slc1a3* upregulated compared to the high-GFAPs. Although our sc RT-qPCR analysis showed two populations of astrocytes with lower/higher GFAP expression, these groups do not correspond to the groups found by Habib et al. First, in our population with low GFAP expression, all other differentially expressed genes are also downregulated; second, the incidence of cells belonging to PCA1 and PCA2 did not change over time as in the study by Habib et al. In order to better classify our group of astrocytes in accordance with this classification, a more detailed analysis of marker gene expression is necessary.

In our previous publications we described the existence of two populations (HR- and LR- astrocytes) of EGFP-positive astrocytes based on the different levels of swelling under exposure to hypo-osmotic stress (Chvatal et al., 2007b) or oxygen-glucose deprivation (Benesova et al., 2012). We proposed that the different swelling mirrored differences in the expression of Cl^-

and K^+ channels and Na^+-K^+-Cl^- cotransporter. Here we show that there are two groups of EGFP-positive astrocytes differing in the expression levels of 35 genes divided by the principle component analysis. These genes include Clcn2 (a gene for the ClC2 channel), which has been reported to be activated by cell swelling (Nielsen et al., 1997) and involved in the RVD by removing Cl^- from the cells. In the study of Benesova at al., *Clcn2* was highly expressed in astrocytic subpopulation 1 (comprising LR-astrocytes), thus possibly contributing to their increased ability of volume regulation. Regarding K^+ channels, we previously suggested that the expression of Kir4.1, TWIK1 and TREK1 may be another reason for the existence of HR- and LR astrocytes. We show here that the genes underlying the PC1 and PC2 subpopulations include *Kcnj10 and Kcnk1* (encoding Kir4.1 and TREK-1 channels). As Kir4.1 has been demonstrated to participate in RVD rather than the swelling (Dibaj et al., 2007; Hirrlinger et al., 2008; Obara-Michlewska et al., 2011), its higher level in the PCA1 population indicates a correlation of PCA1 with cells that better regulate cell volume. Other genes that are also increased in the PCA1 group, namely Cxs and AQP4, correspond to the hypothesis that it is a population of cells with better volume regulation, i.e., LR-astrocytes, as previously proposed (Benesova et al., 2012). The division of the cells into two populations in the present study was performed based on the differential expression of 35 genes. Surprisingly, the population divide was based on the higher/lower expression of all the genes. This may indicate a reduced transcriptional activity in one group of cells. Further investigation of the heterogeneity of EGFP-positive astrocytes in the 3xTg-AD model of AD is therefore necessary. However, it should be also emphasized that transcript levels are not sufficient to predict levels of functional proteins. The level of protein expression can be modulated at the level of translation, protein's half-life, protein synthesis delay as well as protein transport (reviewed for example by Liu et al., 2016, or Sonneveld et al., 2020). Therefore, we are aware that a more detailed analysis of the expression of the proteins of interest and their localization may better elucidate the changes we observe at the level of changes in astrocyte volume and diffusion parameters of the ECS.

Taken together, in younger age groups of AD mice (3-9M), intracellular Aβ accumulation in hippocampal neurons alone has no effect on neural tissue diffusivity, as α and λ are comparable to age-matched controls. Simultaneously, changes in ECS volume fraction and its recovery are almost comparable at these ages regardless of employed pathological stimulus. Nevertheless, the astrocyte swelling induced by hyperkalemia is markedly reduced in 3xTg-AD mice already at 3M, which might be partly caused by increased incidence of LR-astrocytes or already decreased expression of glutamate transporters, connexin 30 and Kir4.1 at this age. In 9M-old astrocytes from 3xTg-AD mice the expression levels of above mention genes are comparable to controls, which may also fit well with their similar swelling. Hypotonicity-evoked swelling in astrocytes from 3xTg-AD mice was significantly smaller compared to age-matched control possibly due to slightly increased number of LR-astrocytes and increased expression of connexin 43 and AQP4.The discrepancy in recovery of astrocyte volume and the ECS volume fraction after hyposmolality or hyperkalemia evoked cell swelling is obvious in older age groups (12M and 18M). This discrepancy is highly probable due to the shift in the proportion of swelling of cells that can regulate their volume (astrocytes) and cells which are not capable of regulation (neurons and possibly other types) (Risher et al., 2009). Genocchi et al. (2020) calculated that this shift can be induced by alterations in expression of specific channels involved in volume and ionic homeostasis. In 12M 3xTg-AD mice, the recovery of α following hypo-osmotic stress was significantly smaller compared to age-matched controls. We hypothesize that such less efficient recovery of ECS volume fraction after hypo-osmotic stress may originate from a more severe impairment of homeostatic functions in 3xTg-AD than in control mice indicating a faster decline of astrocyte homeostatic functions in AD-affected tissue and larger proportion of neuronal swelling. In 18M mice, homeostatic functions are comparably impaired in both control and 3xTg-AD mice and α recovery is only partial in both groups. In contrast, more effective recovery of α occurred in 18M 3xTg-AD hippocampus following hyperkalemia compared to age-matched control. This opposite trend can be explained by distinct mechanisms underlying cell swelling during both insults together with the larger initial ECS volume in 3xTg-AD mice, in which toxic substances/ions are more diluted and do not cause an irreversible cell damage. Irreversible changes may occur especially in non-astrocytic cell types as we observed no difference in astrocyte swelling between control and 3xTg-AD in 18M animals. For comparison see **Supplementary Figure 4**.

CONCLUSION

Overall, in the present study we have shown that APP Swedish, MAPT P301L, and PSEN1 M146V mutations in the murine model of AD lead to the structural changes in the ECS differing from those observed in physiological aging. We suggest that these changes are caused by cell atrophy on the one hand, and shifts and alterations in the ECS content, including an increase in the diffusion obstacles (barriers), on the other. However, these changes do not influence ECS shrinkage under exposure to hypo-osmotic stress or hyperkalemia, but they do affect the ECS recovery during the washout.

Larger ECS and increased tortuosity further affect the function of astrocytes, especially the uptake of ions and neurotransmitters. We have also shown that astrocytes in 3xTg-AD mice swell less during the exposure to hypo-osmotic stress or hyperkalemia, when compared to controls. However, this difference is also partially caused by the higher incidence of cells that swell very little or not at all. We therefore propose that this group of astrocytes expresses a higher number of channels involved in RVD or fewer ion channels/transporters participating in ion/neurotransmitter uptake. Considering age-related changes in tortuosity and astrocyte volume swelling/regulation, we conclude that AD can be understood as an accelerated form of physiological aging even at the level of basic homeostatic functions of astrocytes, such as ion/neurotransmitter uptake and water management.

DATA AVAILABILITY STATEMENT

The original contributions presented in the study are included in the article/**Supplementary Material**, further inquiries can be directed to the corresponding author/s.

ETHICS STATEMENT

The animal study was reviewed and approved by Institute of Experimental Medicine ASCR Animal Care Committee, Prague, Czechia.

AUTHOR CONTRIBUTIONS

JT and MK analyzed and interpreted the data, wrote the manuscript, and prepared all figures. DK, TF, ZH, BP, LM, and JK performed 3D morphometry, IHC, prepared cell suspensions and performed FACS. MK and MC performed real-time iontophoretic method. LuV, PA, and DZ performed RT-qPCR measurement, processed and analyzed data. MA and LyV conceived and supervised the study. All authors contributed to the article and approved the submitted version.

FUNDING

This study was supported by grant 19-02046S from the Czech Science Foundation, by the Institutional support RVO 86652036 and by Operational Programme Research, Development and Education in the framework of the project “Center of Reconstructive Neuroscience,” registration number CZ.02.1.01/0.0./0.0/15_003/0000419.

ACKNOWLEDGMENTS

The authors would like to thank Helena Pavlikova and Marketa Hemerova for their excellent technical assistance and Frances Zatrepalkova for proofreading the manuscript.

SUPPLEMENTARY MATERIAL

The Supplementary Material for this article can be found online at: https://www.frontiersin.org/articles/10.3389/fnagi.2021.783120/full#supplementary-material

REFERENCES

Abe, K., and Misawa, M. (2003). Amyloid beta protein enhances the clearance of extracellular L-glutamate by cultured rat cortical astrocytes. *Neurosci. Res.* 45, 25–31. doi: 10.1016/s0168-0102(02)00190-6

Acosta, C., Anderson, H. D., and Anderson, C. M. (2017). Astrocyte dysfunction in Alzheimer disease. *J. Neurosci. Res.* 95, 2430–2447. doi: 10.1002/jnr.24075

Amiry-Moghaddam, M., Xue, R., Haug, F. M., Neely, J. D., Bhardwaj, A., Agre, P., et al. (2004). Alpha-syntrophin deletion removes the perivascular but not endothelial pool of aquaporin-4 at the blood-brain barrier and delays the development of brain edema in an experimental model of acute hyponatremia. *FASEB J.* 18, 542–544. doi: 10.1096/fj.03-0869fje

Anderova, M., Benesova, J., Mikesova, M., Dzamba, D., Honsa, P., Kriska, J., et al. (2014). Altered astrocytic swelling in the cortex of alpha-syntrophin-negative GFAP/EGFP mice. *PLoS One* 9:e113444. doi: 10.1371/journal.pone.0113444

Anderova, M., Vorisek, I., Pivonkova, H., Benesova, J., Vargova, L., Cicanic, M., et al. (2011). Cell death/proliferation and alterations in glial morphology contribute to changes in diffusivity in the rat hippocampus after hypoxia-ischemia. *J. Cereb. Blood Flow Metab*. 31, 894–907. doi: 10.1038/jcbfm.2010.168

Assefa, B. T., Gebre, A. K., and Altaye, B. M. (2018). Reactive astrocytes as drug target in Alzheimer’s disease. *Biomed. Res. Int.* 2018:4160247. doi: 10.1155/2018/4160247

Baig, S., Wilcock, G. K., and Love, S. (2005). Loss of perineuronal net N-acetylgalactosamine in Alzheimer’s disease. *Acta Neuropathol.* 110, 393–401. doi: 10.1007/s00401-005-1060-2

Beckstrom, H., Julsrud, L., Haugeto, O., Dewar, D., Graham, D. I., Lehre, K. P., et al. (1999). Interindividual differences in the levels of the glutamate transporters Glast and Glt, but no clear correlation with Alzheimer’s disease. *J. Neurosci. Res.* 55, 218–229. doi: 10.1002/(SICI)1097-4547(19990115)55:2<218::AID-JNR9>3.0.CO;2-L

Bekku, Y., Vargova, L., Goto, Y., Vorisek, I., Dmytrenko, L., Narasaki, M., et al. (2010). Bral1: its role in diffusion barrier formation and conduction velocity in the Cns. *J. Neurosci.* 30, 3113–3123. doi: 10.1523/JNEUROSCI.5598-09.2010

Belov Kirdajova, D., Kriska, J., Tureckova, J., and Anderova, M. (2020). Ischemia-Triggered glutamate excitotoxicity from the perspective of glial cells. *Front. Cell Neurosci.* 14:51. doi: 10.3389/fncel.2020.00051

Ben Haim, L., Carrillo-De Sauvage, M. A., Ceyzeriat, K., and Escartin, C. (2015). Elusive roles for reactive astrocytes in neurodegenerative diseases. *Front. Cell Neurosci.* 9:278. doi: 10.3389/fncel.2015.00278

Benesova, J., Hock, M., Butenko, O., Prajerova, I., Anderova, M., and Chvatal, A. (2009). Quantification of astrocyte volume changes during ischemia in situ reveals two populations of astrocytes in the cortex of GFAP/EGFP mice. *J. Neurosci. Res.* 87, 96–111. doi: 10.1002/jnr.21828

Benesova, J., Rusnakova, V., Honsa, P., Pivonkova, H., Dzamba, D., Kubista, M., et al. (2012). Distinct expression/function of potassium and chloride channels contributes to the diverse volume regulation in cortical astrocytes of GFAP/EGFP mice. *PLoS One* 7:e29725. doi: 10.1371/journal.pone.0029725

Bronzuoli, M. R., Facchinetti, R., Valenza, M., Cassano, T., Steardo, L., and Scuderi, C. (2019). Astrocyte function is affected by aging and not alzheimer’s disease: a preliminary investigation in hippocampi of 3xTg-Ad Mice. *Front. Pharmacol.* 10:644. doi: 10.3389/fphar.2019.00644

Burbaeva, G., Boksha, I. S., Tereshkina, E. B., Savushkina, O. K., Starodubtseva, L. I., and Turishcheva, M. S. (2005). Glutamate metabolizing enzymes in prefrontal cortex of Alzheimer’s disease patients. *Neurochem. Res.* 30, 1443–1451. doi: 10.1007/s11064-005-8654-x

Chu, H., Huang, C., Gao, Z., Dong, J., Tang, Y., and Dong, Q. (2017). Reduction of ischemic brain edema by combined use of paeoniflorin and astragaloside iv via down-regulating connexin 43. *Phytother. Res.* 31, 1410–1418. doi: 10.1002/ptr.5868

Chvatal, A., Anderova, M., Hock, M., Prajerova, I., Neprasova, H., Chvatal, V., et al. (2007a). Three-dimensional confocal morphometry reveals structural changes in astrocyte morphology in situ. *J. Neurosci. Res.* 85, 260–271. doi: 10.1002/jnr.21113

Chvatal, A., Anderova, M., and Kirchhoff, F. (2007b). Three-dimensional confocal morphometry - a new approach for studying dynamic changes in cell morphology in brain slices. *J. Anat.* 210, 671–683. doi: 10.1111/j.1469-7580.2007.00724.x

Cicanic, M., Edamatsu, M., Bekku, Y., Vorisek, I., Oohashi, T., and Vargova, L. (2018). A deficiency of the link protein Bral2 affects the size of the extracellular space in the thalamus of aged mice. *J. Neurosci. Res.* 96, 313–327. doi: 10.1002/jnr.24136

De Santis, S., Cosa-Linan, A., Garcia-Hernandez, R., Dmytrenko, L., Vargova, L., Vorisek, I., et al. (2020). Chronic alcohol consumption alters extracellular space geometry and transmitter diffusion in the brain. *Sci. Adv.* 6:eaba0154. doi: 10.1126/sciadv.aba0154

De Strooper, B., and Karran, E. (2016). The cellular phase of Alzheimer's disease. *Cell* 164, 603–615.

Deng, Y. Y., Shen, F. C., Xie, D., Han, Q. P., Fang, M., Chen, C. B., et al. (2016). Progress in drug treatment of cerebral edema. *Mini Rev. Med. Chem.* 16, 917–925. doi: 10.2174/1389557516666160304151233

Dibaj, P., Kaiser, M., Hirrlinger, J., Kirchhoff, F., and Neusch, C. (2007). Kir4.1 channels regulate swelling of astroglial processes in experimental spinal cord edema. *J. Neurochem.* 103, 2620–2628. doi: 10.1111/j.1471-4159.2007.04979.x

Dmytrenko, L., Cicanic, M., Anderova, M., Vorisek, I., Ottersen, O. P., Sykova, E., et al. (2013). The impact of alpha-syntrophin deletion on the changes in tissue structure and extracellular diffusion associated with cell swelling under physiological and pathological conditions. *PLoS One* 8:e68044. doi: 10.1371/journal.pone.0068044

Frohlich, C., Paarmann, K., Steffen, J., Stenzel, J., Krohn, M., Heinze, H. J., et al. (2013). Genomic background-related activation of microglia and reduced beta-amyloidosis in a mouse model of Alzheimer's disease. *Eur. J. Microbiol. Immunol.* 3, 21–27. doi: 10.1556/EuJMI.3.2013.1.3

Genocchi, B., Cunha, A., Jain, S., Hyttinen, J., Lenk, K., and Ellingsrud, A. J. (2020). Parametric exploration of cellular swelling in a computational model of cortical spreading depression. *Annu. Int. Conf. IEEE Eng. Med. Biol. Soc.* 2020, 2491–2495. doi: 10.1109/EMBC44109.2020.9175306

Goetzl, E. J., and Miller, B. L. (2017). Multicellular hypothesis for the pathogenesis of Alzheimer's disease. *FASEB J.* 31, 1792–1795. doi: 10.1096/fj.201601221R

Habib, N., Mccabe, C., Medina, S., Varshavsky, M., Kitsberg, D., Dvir-Szternfeld, R., et al. (2020). Disease-associated astrocytes in Alzheimer's disease and aging. *Nat. Neurosci.* 23, 701–706. doi: 10.1038/s41593-020-0624-8

Haj-Yasein, N. N., Jensen, V., Ostby, I., Omholt, S. W., Voipio, J., Kaila, K., et al. (2012). Aquaporin-4 regulates extracellular space volume dynamics during high-frequency synaptic stimulation: a gene deletion study in mouse hippocampus. *Glia* 60, 867–874. doi: 10.1002/glia.22319

Hardy, J., and Selkoe, D. J. (2002). The amyloid hypothesis of Alzheimer's disease: progress and problems on the road to therapeutics. *Science* 297, 353–356. doi: 10.1126/science.1072994

Harrison, I. F., Ismail, O., Machhada, A., Colgan, N., Ohene, Y., Nahavandi, P., et al. (2020). Impaired glymphatic function and clearance of tau in an Alzheimer's disease model. *Brain* 143, 2576–2593. doi: 10.1093/brain/awaa179

Harry, G. J. (2013). Microglia during development and aging. *Pharmacol. Ther.* 139, 313–326. doi: 10.1016/j.pharmthera.2013.04.013

Hertelendy, P., Varga, D. P., Menyhart, A., Bari, F., and Farkas, E. (2019). Susceptibility of the cerebral cortex to spreading depolarization in neurological disease states: the impact of aging. *Neurochem. Int.* 127, 125–136. doi: 10.1016/j.neuint.2018.10.010

Hinson, S. R., Roemer, S. F., Lucchinetti, C. F., Fryer, J. P., Kryzer, T. J., Chamberlain, J. L., et al. (2008). Aquaporin-4-binding autoantibodies in patients with neuromyelitis optica impair glutamate transport by down-regulating Eaat2. *J. Exp. Med.* 205, 2473–2481. doi: 10.1084/jem.20081241

Hirrlinger, P. G., Wurm, A., Hirrlinger, J., Bringmann, A., and Reichenbach, A. (2008). Osmotic swelling characteristics of glial cells in the murine hippocampus, cerebellum, and retina in situ. *J. Neurochem.* 105, 1405–1417. doi: 10.1111/j.1471-4159.2008.05243.x

Holmes, B. B., Devos, S. L., Kfoury, N., Li, M., Jacks, R., Yanamandra, K., et al. (2013). Heparan sulfate proteoglycans mediate internalization and propagation of specific proteopathic seeds. *Proc. Natl. Acad. Sci. U.S.A.* 110, E3138–E3147. doi: 10.1073/pnas.1301440110

Hoshi, A., Tsunoda, A., Yamamoto, T., Tada, M., Kakita, A., and Ugawa, Y. (2018). Altered expression of glutamate transporter-1 and water channel protein aquaporin-4 in human temporal cortex with Alzheimer's disease. *Neuropathol. Appl. Neurobiol.* 44, 628–638. doi: 10.1111/nan.12475

Hoshi, A., Yamamoto, T., Shimizu, K., Ugawa, Y., Nishizawa, M., Takahashi, H., et al. (2012). Characteristics of aquaporin expression surrounding senile plaques and cerebral amyloid angiopathy in Alzheimer disease. *J. Neuropathol. Exp. Neurol.* 71, 750–759. doi: 10.1097/NEN.0b013e3182632566

Hrabetova, S., and Nicholson, C. (2004). Contribution of dead-space microdomains to tortuosity of brain extracellular space. *Neurochem. Int.* 45, 467–477. doi: 10.1016/j.neuint.2003.11.011

Hrabetova, S., Hrabe, J., and Nicholson, C. (2003). Dead-space microdomains hinder extracellular diffusion in rat neocortex during ischemia. *J. Neurosci.* 23, 8351–8359. doi: 10.1523/JNEUROSCI.23-23-08351.2003

Hynd, M. R., Scott, H. L., and Dodd, P. R. (2004). Glutamate-mediated excitotoxicity and neurodegeneration in Alzheimer's disease. *Neurochem. Int.* 45, 583–595. doi: 10.1016/j.neuint.2004.03.007

Ikegaya, Y., Matsuura, S., Ueno, S., Baba, A., Yamada, M. K., Nishiyama, N., et al. (2002). Beta-amyloid enhances glial glutamate uptake activity and attenuates synaptic efficacy. *J. Biol. Chem.* 277, 32180–32186. doi: 10.1074/jbc.M203764200

Ingelsson, M., Fukumoto, H., Newell, K. L., Growdon, J. H., Hedley-Whyte, E. T., Frosch, M. P., et al. (2004). Early Abeta accumulation and progressive synaptic loss, gliosis, and tangle formation in Ad brain. *Neurology* 62, 925–931. doi: 10.1212/01.wnl.0000115115.98960.37

Itagaki, S., Mcgeer, P. L., Akiyama, H., Zhu, S., and Selkoe, D. (1989). Relationship of microglia and astrocytes to amyloid deposits of Alzheimer disease. *J. Neuroimmunol.* 24, 173–182. doi: 10.1016/0165-5728(89)90115-x

Jabaudon, D., Scanziani, M., Gahwiler, B. H., and Gerber, U. (2000). Acute decrease in net glutamate uptake during energy deprivation. *Proc. Natl. Acad. Sci. U.S.A.* 97, 5610–5615. doi: 10.1073/pnas.97.10.5610

Jacob, C. P., Koutsilieri, E., Bartl, J., Neuen-Jacob, E., Arzberger, T., Zander, N., et al. (2007). Alterations in expression of glutamatergic transporters and receptors in sporadic Alzheimer's disease. *J. Alzheimers Dis.* 11, 97–116. doi: 10.3233/jad-2007-11113

Kelly, P. H., Bondolfi, L., Hunziker, D., Schlecht, H. P., Carver, K., Maguire, E., et al. (2003). Progressive age-related impairment of cognitive behavior in App23 transgenic mice. *Neurobiol. Aging* 24, 365–378. doi: 10.1016/s0197-4580(02)00098-2

Klemens, J., Ciurkiewicz, M., Chludzinski, E., Iseringhausen, M., Klotz, D., Pfankuche, V. M., et al. (2019). Neurotoxic potential of reactive astrocytes in canine distemper demyelinating leukoencephalitis. *Sci. Rep.* 9:11689. doi: 10.1038/s41598-019-48146-9

Kolenicova, D., Tureckova, J., Pukajova, B., Harantova, L., Kriska, J., Kirdajova, D., et al. (2020). High potassium exposure reveals the altered ability of astrocytes to regulate their volume in the aged hippocampus of Gfap/Egfp mice. *Neurobiol. Aging* 86, 162–181. doi: 10.1016/j.neurobiolaging.2019.10.009

Kriska, J., Hermanova, Z., Knotek, T., Tureckova, J., and Anderova, M. (2021). On the common journey of neural cells through ischemic brain injury and Alzheimer's disease. *Int. J. Mol. Sci.* 22:9689. doi: 10.3390/ijms22189689

Kulijewicz-Nawrot, M., Sykova, E., Chvatal, A., Verkhratsky, A., and Rodriguez, J. J. (2013). Astrocytes and glutamate homoeostasis in Alzheimer's disease: a decrease in glutamine synthetase, but not in glutamate transporter-1, in the prefrontal cortex. *ASN Neuro* 5, 273–282. doi: 10.1042/AN20130017

Kulijewicz-Nawrot, M., Verkhratsky, A., Chvatal, A., Sykova, E., and Rodriguez, J. J. (2012). Astrocytic cytoskeletal atrophy in the medial prefrontal cortex of a triple transgenic mouse model of Alzheimer's disease. *J. Anat.* 221, 252–262. doi: 10.1111/j.1469-7580.2012.01536.x

Lan, Y. L., Zhao, J., Ma, T., and Li, S. (2016). The potential roles of aquaporin 4 in Alzheimer's disease. *Mol. Neurobiol.* 53, 5300–5309. doi: 10.1007/s12035-015-9446-1

Larsen, B. R., Assentoft, M., Cotrina, M. L., Hua, S. Z., Nedergaard, M., Kaila, K., et al. (2014). Contributions of the Na(+)/K(+)-Atpase, Nkcc1, and Kir4.1 to hippocampal K(+) clearance and volume responses. *Glia* 62, 608–622. doi: 10.1002/glia.22629

Li, G., and Olson, J. E. (2008). Purinergic activation of anion conductance and osmolyte efflux in cultured rat hippocampal neurons. *Am. J. Physiol. Cell Physiol.* 295, C1550–C1560. doi: 10.1152/ajpcell.90605.2007

Li, G., Liu, X., Liu, Z., and Su, Z. (2015). Interactions of connexin 43 and aquaporin-4 in the formation of glioma-induced brain edema. *Mol. Med. Rep.* 11, 1188–1194. doi: 10.3892/mmr.2014.2867

Li, X., Heinzel, F. R., Boengler, K., Schulz, R., and Heusch, G. (2004). Role of connexin 43 in ischemic preconditioning does not involve intercellular communication through gap junctions. *J. Mol. Cell Cardiol.* 36, 161–163. doi: 10.1016/j.yjmcc.2003.10.019

Li, Y. K., Wang, F., Wang, W., Luo, Y., Wu, P. F., Xiao, J. L., et al. (2012). Aquaporin-4 deficiency impairs synaptic plasticity and associative fear memory in the lateral amygdala: involvement of downregulation of glutamate transporter-1 expression. *Neuropsychopharmacology* 37, 1867–1878. doi: 10.1038/npp.2012.34

Liu, Y., Beyer, A., and Aebersold, R. (2016). On the dependency of cellular protein levels on MRNA abundance. *Cell* 165, 535–550. doi: 10.1016/j.cell.2016.03.014

Macaulay, N., and Zeuthen, T. (2012). Glial K(+) clearance and cell swelling: key roles for cotransporters and pumps. *Neurochem. Res.* 37, 2299–2309. doi: 10.1007/s11064-012-0731-3

MacAulay, N., Gether, U., Klaeke, D. A., and Zeuthen, T. (2002). Passive water and urea permeability of a human Na(+)-glutamate cotransporter expressed in Xenopus oocytes. *J. Physiol.* 542, 817–828. doi: 10.1113/jphysiol.2002.020586

MacVicar, B. A., Feighan, D., Brown, A., and Ransom, B. (2002). Intrinsic optical signals in the rat optic nerve: role for K(+) uptake via Nkcc1 and swelling of astrocytes. *Glia* 37, 114–123. doi: 10.1002/glia.10023

Manley, G. T., Fujimura, M., Ma, T., Noshita, N., Filiz, F., Bollen, A. W., et al. (2000). Aquaporin-4 deletion in mice reduces brain edema after acute water intoxication and ischemic stroke. *Nat. Med.* 6, 159–163. doi: 10.1038/72256

Matos, M., Augusto, E., Oliveira, C. R., and Agostinho, P. (2008). Amyloid-beta peptide decreases glutamate uptake in cultured astrocytes: involvement of oxidative stress and mitogen-activated protein kinase cascades. *Neuroscience* 156, 898–910. doi: 10.1016/j.neuroscience.2008.08.022

Minati, L., Edginton, T., Bruzzone, M. G., and Giaccone, G. (2009). Current concepts in Alzheimer's disease: a multidisciplinary review. *Am. J. Alzheimers Dis. Dement.* 24, 95–121. doi: 10.1177/1533317508328602

Moftakhar, P., Lynch, M. D., Pomakian, J. L., and Vinters, H. V. (2010). Aquaporin expression in the brains of patients with or without cerebral amyloid angiopathy. *J. Neuropathol. Exp. Neurol.* 69, 1201–1209. doi: 10.1097/NEN.0b013e3181fd252c

Morawski, M., Bruckner, G., Jager, C., Seeger, G., Matthews, R. T., and Arendt, T. (2012). Involvement of perineuronal and perisynaptic extracellular matrix in Alzheimer's disease neuropathology. *Brain Pathol.* 22, 547–561. doi: 10.1111/j.1750-3639.2011.00557.x

Morawski, M., Filippov, M., Tzinia, A., Tsilibary, E., and Vargova, L. (2014). ECM in brain aging and dementia. *Prog. Brain Res.* 214, 207–227. doi: 10.1016/B978-0-444-63486-3.00010-4

Murphy, T. R., Davila, D., Cuvelier, N., Young, L. R., Lauderdale, K., Binder, D. K., et al. (2017). Hippocampal and cortical pyramidal neurons swell in parallel with astrocytes during acute hypoosmolar stress. *Front. Cell Neurosci.* 11:275. doi: 10.3389/fncel.2017.00275

Nedergaard, M., and Goldman, S. A. (2020). Glymphatic failure as a final common pathway to dementia. *Science* 370, 50–56. doi: 10.1126/science.abb8739

Nicchia, G. P., Srinivas, M., Li, W., Brosnan, C. F., Frigeri, A., and Spray, D. C. (2005). New possible roles for aquaporin-4 in astrocytes: cell cytoskeleton and functional relationship with connexin43. *FASEB J.* 19, 1674–1676. doi: 10.1096/fj.04-3281fje

Nicholson, C. (1993). Ion-selective microelectrodes and diffusion measurements as tools to explore the brain cell microenvironment. *J. Neurosci. Methods* 48, 199–213. doi: 10.1016/0165-0270(93)90092-6

Nicholson, C., and Phillips, J. M. (1981). Ion diffusion modified by tortuosity and volume fraction in the extracellular microenvironment of the rat cerebellum. *J. Physiol.* 321, 225–257. doi: 10.1113/jphysiol.1981.sp013981

Nielsen, S., Nagelhus, E. A., Amiry-Moghaddam, M., Bourque, C., Agre, P., and Ottersen, O. P. (1997). Specialized membrane domains for water transport in glial cells: high-resolution immunogold cytochemistry of aquaporin-4 in rat brain. *J. Neurosci.* 17, 171–180. doi: 10.1523/JNEUROSCI.17-01-00171.1997

Nolte, C., Matyash, M., Pivneva, T., Schipke, C. G., Ohlemeyer, C., Hanisch, U. K., et al. (2001). GFAP promoter-controlled Egfp-expressing transgenic mice: a tool to visualize astrocytes and astrogliosis in living brain tissue. *Glia* 33, 72–86.

Obara-Michlewska, M., Pannicke, T., Karl, A., Bringmann, A., Reichenbach, A., Szeliga, M., et al. (2011). Down-regulation of Kir4.1 in the cerebral cortex of rats with liver failure and in cultured astrocytes treated with glutamine: implications for astrocytic dysfunction in hepatic encephalopathy. *J. Neurosci. Res.* 89, 2018–2027. doi: 10.1002/jnr.22656

Oddo, S., Caccamo, A., Shepherd, J. D., Murphy, M. P., Golde, T. E., Kayed, R., et al. (2003). Triple-transgenic model of Alzheimer's disease with plaques and tangles: intracellular Abeta and synaptic dysfunction. *Neuron* 39, 409–421. doi: 10.1016/s0896-6273(03)00434-3

Okada, Y., Sato, K., and Numata, T. (2009). Pathophysiology and puzzles of the volume-sensitive outwardly rectifying anion channel. *J. Physiol.* 587, 2141–2149. doi: 10.1113/jphysiol.2008.165076

Olabarria, M., Noristani, H. N., Verkhratsky, A., and Rodriguez, J. J. (2011). Age-dependent decrease in glutamine synthetase expression in the hippocampal astroglia of the triple transgenic Alzheimer's disease mouse model: mechanism for deficient glutamatergic transmission? *Mol. Neurodegener.* 6:55. doi: 10.1186/1750-1326-6-55

Olson, J. E., and Li, G. Z. (2000). Osmotic sensitivity of taurine release from hippocampal neuronal and glial cells. *Adv. Exp. Med. Biol.* 483, 213–218. doi: 10.1007/0-306-46838-7_23

Papadopoulos, M. C., and Verkman, A. S. (2005). Aquaporin-4 gene disruption in mice reduces brain swelling and mortality in pneumococcal meningitis. *J. Biol. Chem.* 280, 13906–13912. doi: 10.1074/jbc.M413627200

Pasantes-Morales, H., and Vazquez-Juarez, E. (2012). Transporters and channels in cytotoxic astrocyte swelling. *Neurochem. Res.* 37, 2379–2387. doi: 10.1007/s11064-012-0777-2

Peng, W., Achariyar, T. M., Li, B., Liao, Y., Mestre, H., Hitomi, E., et al. (2016). Suppression of glymphatic fluid transport in a mouse model of Alzheimer's disease. *Neurobiol. Dis.* 93, 215–225. doi: 10.1016/j.nbd.2016.05.015

Plog, B. A., and Nedergaard, M. (2018). The glymphatic system in central nervous system health and disease: past, present, and future. *Annu. Rev. Pathol.* 13, 379–394. doi: 10.1146/annurev-pathol-051217-111018

Prince, M., Bryce, R., Albanese, E., Wimo, A., Ribeiro, W., and Ferri, C. P. (2013). The global prevalence of dementia: a systematic review and metaanalysis. *Alzheimers Dement.* 9:e2.

Qosa, H., Abuznait, A. H., Hill, R. A., and Kaddoumi, A. (2012). Enhanced brain amyloid-beta clearance by rifampicin and caffeine as a possible protective mechanism against Alzheimer's disease. *J. Alzheimers Dis.* 31, 151–165. doi: 10.3233/JAD-2012-120319

Qosa, H., and Kaddoumi, A. (2016). Effect of mouse strain as a background for Alzheimer's disease models on the clearance of amyloid-beta. *J. Syst. Integr. Neurosci.* 2, 135–140. doi: 10.15761/JSIN.1000123

Reeves, B. C., Karimy, J. K., Kundishora, A. J., Mestre, H., Cerci, H. M., Matouk, C., et al. (2020). Glymphatic system impairment in alzheimer's disease and idiopathic normal pressure hydrocephalus. *Trends Mol. Med.* 26, 285–295. doi: 10.1016/j.molmed.2019.11.008

Risher, W. C., Andrew, R. D., and Kirov, S. A. (2009). Real-time passive volume responses of astrocytes to acute osmotic and ischemic stress in cortical slices and in vivo revealed by two-photon microscopy. *Glia* 57, 207–221. doi: 10.1002/glia.20747

Rodriguez-Arellano, J. J., Parpura, V., Zorec, R., and Verkhratsky, A. (2016). Astrocytes in physiological aging and Alzheimer's disease. *Neuroscience* 323, 170–182. doi: 10.1016/j.neuroscience.2015.01.007

Roitbak, T., and Sykova, E. (1999). Diffusion barriers evoked in the rat cortex by reactive astrogliosis. *Glia* 28, 40–48. doi: 10.1002/(sici)1098-1136(199910)28:1<40::aid-glia5>3.0.co;2-6

Rusnakova, V., Honsa, P., Dzamba, D., Stahlberg, A., Kubista, M., and Anderova, M. (2013). Heterogeneity of astrocytes: from development to injury - single cell gene expression. *PLoS One* 8:e69734. doi: 10.1371/journal.pone.0069734

Scimemi, A., Meabon, J. S., Woltjer, R. L., Sullivan, J. M., Diamond, J. S., and Cook, D. G. (2013). Amyloid-beta1-42 slows clearance of synaptically released glutamate by mislocalizing astrocytic Glt-1. *J. Neurosci.* 33, 5312–5318. doi: 10.1523/JNEUROSCI.5274-12.2013

Serrano-Pozo, A., Muzikansky, A., Gomez-Isla, T., Growdon, J. H., Betensky, R. A., Frosch, M. P., et al. (2013). Differential relationships of reactive astrocytes and microglia to fibrillar amyloid deposits in Alzheimer disease. *J. Neuropathol. Exp. Neurol.* 72, 462–471. doi: 10.1097/NEN.0b013e3182933788

Sethi, M. K., and Zaia, J. (2017). Extracellular matrix proteomics in schizophrenia and Alzheimer's disease. *Anal. Bioanal. Chem.* 409, 379–394. doi: 10.1007/s00216-016-9900-6

Smith, M. A., Rottkamp, C. A., Nunomura, A., Raina, A. K., and Perry, G. (2000). Oxidative stress in Alzheimer's disease. *Biochim. Biophys. Acta* 1502, 139–144.

Sonneveld, S., Verhagen, B. M. P., and Tanenbaum, M. E. (2020). Heterogeneity in MRNA Translation. *Trends Cell Biol.* 30, 606–618. doi: 10.1016/j.tcb.2020.04.008

Su, G., Kintner, D. B., and Sun, D. (2002). Contribution of Na(+)-K(+)-Cl(-) cotransporter to high-[K(+)](o)- induced swelling and EAA release in astrocytes. *Am. J. Physiol. Cell Physiol.* 282, C1136–C1146. doi: 10.1152/ajpcell.00478.2001

Sykova, E., and Nicholson, C. (2008). Diffusion in brain extracellular space. *Physiol. Rev.* 88, 1277–1340. doi: 10.1152/physrev.00027.2007

Sykova, E., Vorisek, I., Antonova, T., Mazel, T., Meyer-Luehmann, M., Jucker, M., et al. (2005). Changes in extracellular space size and geometry in App23 transgenic mice: a model of Alzheimer's disease. *Proc. Natl. Acad. Sci. U.S.A.* 102, 479–484. doi: 10.1073/pnas.0408235102

Tarasoff-Conway, J. M., Carare, R. O., Osorio, R. S., Glodzik, L., Butler, T., Fieremans, E., et al. (2015). Clearance systems in the brain-implications for Alzheimer disease. *Nat. Rev. Neurol.* 11, 457–470. doi: 10.1038/nrneurol.2015.119

Thorne, R. G., and Nicholson, C. (2006). In vivo diffusion analysis with quantum dots and dextrans predicts the width of brain extracellular space. *Proc. Natl. Acad .Sci. U.S.A.* 103, 5567–5572. doi: 10.1073/pnas.0509425103

Ting, J. T., Daigle, T. L., Chen, Q., and Feng, G. (2014). Acute brain slice methods for adult and aging animals: application of targeted patch clamp analysis and optogenetics. *Methods Mol. Biol.* 1183, 221–242. doi: 10.1007/978-1-4939-1096-0_14

Toft-Bertelsen, T. L., Larsen, B. R., Christensen, S. K., Khandelia, H., Waagepetersen, H. S., and Macaulay, N. (2021). Clearance of activity-evoked K(+) transients and associated glia cell swelling occur independently of Aqp4: a study with an isoform-selective Aqp4 inhibitor. *Glia* 69, 28–41. doi: 10.1002/glia.23851

Vajda, Z., Pedersen, M., Fuchtbauer, E. M., Wertz, K., Stodkilde-Jorgensen, H., Sulyok, E., et al. (2002). Delayed onset of brain edema and mislocalization of aquaporin-4 in dystrophin-null transgenic mice. *Proc. Natl. Acad. Sci. U.S.A.* 99, 13131–13136. doi: 10.1073/pnas.192457099

Valenza, M., Facchinetti, R., Steardo, L., and Scuderi, C. (2019). Altered waste disposal system in aging and alzheimer's disease: focus on astrocytic aquaporin-4. *Front. Pharmacol.* 10:1656. doi: 10.3389/fphar.2019.01656

Valny, M., Honsa, P., Waloschkova, E., Matuskova, H., Kriska, J., Kirdajova, D., et al. (2018). A single-cell analysis reveals multiple roles of oligodendroglial lineage cells during post-ischemic regeneration. *Glia* 66, 1068–1081. doi: 10.1002/glia.23301

Vegh, M. J., Rausell, A., Loos, M., Heldring, C. M., Jurkowski, W., Van Nierop, P., et al. (2014b). Hippocampal extracellular matrix levels and stochasticity in synaptic protein expression increase with age and are associated with age-dependent cognitive decline. *Mol. Cell Proteomics* 13, 2975–2985. doi: 10.1074/mcp.M113.032086

Vegh, M. J., Heldring, C. M., Kamphuis, W., Hijazi, S., Timmerman, A. J., Li, K. W., et al. (2014a). Reducing hippocampal extracellular matrix reverses early memory deficits in a mouse model of Alzheimer's disease. *Acta Neuropathol. Commun.* 2:76. doi: 10.1186/s40478-014-0076-z

Voipio, J., Pasternack, M., and Macleod, K. (1994). *Ion-sensitive microelectrodes. Microelectrode Techniques: The Plymouth Workshop Handbook*, 2 Edn. Cambridge: The Company of Biologists Limited, 275–316.

Vorisek, I., and Sykova, E. (1997). Ischemia-induced changes in the extracellular space diffusion parameters. K+, and pH in the developing rat cortex and corpus callosum. *J. Cereb. Blood Flow Metab.* 17, 191–203. doi: 10.1097/00004647-199702000-00009

Walch, E., Murphy, T. R., Cuvelier, N., Aldoghmi, M., Morozova, C., Donohue, J., et al. (2020). Astrocyte-selective volume increase in elevated extracellular potassium conditions is mediated by The Na(+)/K(+) atpase and occurs independently of aquaporin 4. *ASN Neuro* 12:1759091420967152.

Walton, H. S., and Dodd, P. R. (2007). Glutamate-glutamine cycling in Alzheimer's disease. *Neurochem. Int.* 50, 1052–1066. doi: 10.1016/j.neuint.2006.10.007

Wilson, C. S., and Mongin, A. A. (2018). Cell volume control in healthy brain and neuropathologies. *Curr. Top. Membr.* 81, 385–455. doi: 10.1016/bs.ctm.2018.07.006

Wolak, D. J., and Thorne, R. G. (2013). Diffusion of macromolecules in the brain: implications for drug delivery. *Mol. Pharm.* 10, 1492–1504. doi: 10.1021/mp300495e

Xekardaki, A., Kovari, E., Gold, G., Papadimitropoulou, A., Giacobini, E., Herrmann, F., et al. (2015). Neuropathological changes in aging brain. *Adv. Exp. Med. Biol.* 821, 11–17. doi: 10.1007/978-3-319-08939-3_6

Yang, J., Li, M. X., Luo, Y., Chen, T., Liu, J., Fang, P., et al. (2013). Chronic ceftriaxone treatment rescues hippocampal memory deficit in Aqp4 knockout mice via activation of Glt-1. *Neuropharmacology* 75, 213–222. doi: 10.1016/j.neuropharm.2013.08.009

Yang, J., Lunde, L. K., Nuntagij, P., Oguchi, T., Camassa, L. M., Nilsson, L. N., et al. (2011). Loss of astrocyte polarization in the tg-ArcSwe mouse model of Alzheimer's disease. *J. Alzheimers Dis.* 27, 711–722. doi: 10.3233/JAD-2011-110725

Ye, Z. C., Oberheim, N., Kettenmann, H., and Ransom, B. R. (2009). Pharmacological "cross-inhibition" of connexin hemichannels and swelling activated anion channels. *Glia* 57, 258–269. doi: 10.1002/glia.20754

Zamecnik, J., Vargova, L., Homola, A., Kodet, R., and Sykova, E. (2004). Extracellular matrix glycoproteins and diffusion barriers in human astrocytic tumours. *Neuropathol. Appl. Neurobiol.* 30, 338–350. doi: 10.1046/j.0305-1846.2003.00541.x

Zeng, X. N., Sun, X. L., Gao, L., Fan, Y., Ding, J. H., and Hu, G. (2007). Aquaporin-4 deficiency down-regulates glutamate uptake and Glt-1 expression in astrocytes. *Mol. Cell Neurosci.* 34, 34–39. doi: 10.1016/j.mcn.2006.09.008

Conflict of Interest: The authors declare that the research was conducted in the absence of any commercial or financial relationships that could be construed as a potential conflict of interest.